eman ta zabal zazu

Universidad del País Vasco
Euskal Herriko Unibertsitatea

UNIVERSITY OF THE BASQUE COUNTRY UPV/EHU
FACULTY OF SCIENCE AND TECHNOLOGY

---

Doctoral Programme in Physics Engineering
Department of Electricity and Electronics

# MICROPHONICS CONTROL FOR SUPERCONDUCTING RADIO FREQUENCY CAVITIES USING A DELAY-RESISTANT MODIFICATION OF THE ACTIVE DISTURBANCE REJECTION CONTROL

Doctoral Thesis

**Ander Elejaga Estiballes**

Advisors

**Josu Jugo Garcia**
**Pablo Echevarria Fernandez**

Leioa, 2024

# ACKNOWLEDGMENT

Para comenzar, Me gustaría mostrar mi más sincero agradecimiento a mis tutores, el Dr. Josu Jugo y el Dr. Pablo Echevarria, por dedicarme su preciado tiempo y atención, siempre que lo he necesitado. Este trabajo nunca habría llegado a buen puerto sin su gran conocimiento y dedicación. Trás tantas horas de congresos, conversaciones y largas jornadas de trabajo codo con codo, los considero más unos amigos que simples tutores. Y a colación de las extensas jornadas de mediciones y experimentos, que bien podían alargarse hasta altas horas de la noche, me gustaría dejar una especial nota de agradecimiento a Marta, por hacerse cargo, ella sola, del cuidado de sus hijas pequeñas aquellos días en los que Pablo trabajaba más horas de las debidas con el único motivo de ayudarme.

También es más que justo agradecer al departamento de Electricidad y Electrónica de la Facultad de Ciencia y Tecnología de la UPV/EHU por proporcionarme los medios necesarios, ya fueran materiales o de conocimiento, para llevar a cabo este trabajo. Se trata de un grupo de personas de una calidad humana y profesional excepcional que nunca ha dudado en integrarme como a uno más. En especial, me gustaría agradecer al Dr. Asier Lopez por facilitarme esta genial plantilla de Latex que he utilizado.

I would like to continue thanking, this time in English, the Helmholtz Zentrum Berlin, for allowing me to carry out my doctoral internship at their facilities and also for funding part of it. Rarely does an aspiring scientist have the good fortune to rub shoulders with such renowned scientists and have access to the infrastructure that a world-class research facility has to offer. I would especially like to thank Dr. Axel Neumann, Dr. Jens Knobloch, Dr. Andriy Ushakov and of course Dr. Pablo Echevarria for helping me without reservation and making me feel at home.

I would also like to thank Dr. Andrea Bellandi and, again, Dr. Axel Neumann for volunteering to read and proofread my paper. It has been truly fortunate to have the opinion and advice of such experts in the field. I believe that after implementing their suggestions, the written presentation of the thesis has taken a significant leap in quality.

Esta tesis ha supuesto para mi una experiencia un tanto agridulce. Ha sido un camino largo y lleno de baches, tanto en lo personal como en lo profesional, que no me ha dejado otra opción que evolucionar como persona. Ha habido momentos difíciles, en los que he pensado en abandonar, y la única razón que me ha hecho seguir adelante es el apoyo inconmensurable de mi familia y amigos. Es por esto que quiero agradecerles de todo corazón su ayuda y compañía. En especial, me gustaría resaltar la suerte que he tenido al coincidir con unos compañeros de doctorado tan excepcionales. Hemos vivido momentos difíciles pero también muy felices de los que atesoraré recuerdos de por vida.

Por último, cómo no agradecer a la persona que más me ha apoyando y ha sacrificado por mi. Mi pareja Ruth ha sido como el hogar al que vuelves tras un día duro de trabajo, como el árbol bajo el que te resguardas de la tormenta, y es por ello que quiero expresar mi más profundo agradecimiento y devoción. Sin ella, este largo trayecto habría sido completamente intransitable. Te quiero con todo mi corazón.

*A José Antonio Elejaga Aguado (*1955-†2020). Siento que no pudieras acompañarme hasta el final del camino.*

# ABSTRACT

The main objective of this thesis is to develop a feedback controller capable of reducing the peak detuning of SRF cavities being operated with high $Q_L$. Detuning occurs when factors like mechanical vibrations and radiation pressure cause the cavity's resonance frequency to deviate from the desired operating frequency, leading to a significant degradation of the efficiency of the accelerator and, in extreme cases, may even cause operational failures. This dissertation will deal in particular with microphonic detuning, which refers to any external mechanical perturbations affecting the accelerating structure. The resulting controller will be tested on a 9-cell TESLA cavity in the Horizontal-Bi-Cavity-Teststand (HoBiCaT) of Helmholtz-Zentrum Berlin (HZB).

Chapter 2 begins by setting out the basic theoretical foundations for an in-depth understanding of the causes and effects of microphonic detuning. To do so, it is necessary to review the electromagnetic behavior of resonant cavities, and the effect that coupled mechanical disturbances have on it. Likewise, the main sources of microphonics are also discussed and an extensive study of the state of the art regarding the control of such disturbances is carried out. From these researches it is determined that the Active Disturbance Rejection Algorithm (ADRC) is a suitable alternative as a feedback controller for low frequency disturbances.

In chapter 3, the ADRC controller is studied in detail, analyzing its mathematical description and testing it in simulation on several systems using Matlab/Simulink. Based on the results obtained, the shortcomings of the ADRC for controlling delayed systems are evident, since it tends to destabilize with relatively low delays. Thus, a study of the different techniques used to date to improve the performance of the ADRC against systems with delay was done and it was concluded that none of them are valid for the case in question, since they sacrifice performance, and specially disturbance rejection capabilities, in favor of stability.

Chapter 4 lays the foundations of a novel proposal for the improvement of ADRC in systems with time delay, the Modified Linear Active Disturbance Rejection Algorithm (MLADRC). First, the mathematical development by which the MLADRC is defined is presented, emphasizing the differences and advantages with respect to the original ADRC. Then, a stability study of the algo-

rithm is performed and the effect that the different parameters have on the controller performance is tested. Lastly, the aforementioned approach is implemented in a real mechanical system with relevant resonant modes to analyse the feasibility of the design process and the performance of the resulting controller, obtaining promising results.

In chapter 5, the implementation and testing of the MLADRC algorithm in a 9-cell TESLA cavity is presented. To do so, the controller is first tested in a virtual SRF cavity using Matlab/Simulink. Then, work was done on the fixed-point design of the controller for its subsequent implementation on FPGA. For this purpose, it is programmed both in Labview FPGA and VHDL. The next step is to debug the hardware implementation of the controller using Hardware In the Loop (HIL) techniques and a simulator implemented in a PXI. Lastly, the controller is implemented and tested on the real system, a 9-cell TESLA cavity. The results are analyzed and discussed in the final part of the chapter.

Finally, Chapter 6 contains a brief summary of the most important results of the thesis and the pertinent conclusions.

Additionally general knowledge about accelerating cavities is added in the Appendices. This information is out of the scope of this thesis but an uninitiated reader might find it useful to understand better the overall context of this work. The technical details of the hardware used in the different experiments of this work have also been compiled in the Appendices to facilitate the reading of certain chapters.

# CONTENTS

# CHAPTER 1

# INTRODUCTION

Particle accelerators, remarkable achievements of modern science and engineering, hold immense relevance in modern society across a wide range of disciplines. While their primary function lies in exploring fundamental physics, their deep impact extends to technological advancements, medical and industrial applications, environmental research, and the cultivation of human capital.

In the realm of fundamental science, particle accelerators have revolutionized the understanding of the universe. By colliding extremely energetic particles, these machines recreate conditions similar to the universe's early moments, shedding light on fundamental particles, forces, and cosmic evolution. These experiments yield insights into the fundamental laws that govern the universe, helping scientist to understand and reveal questions about the laws of physics that have remained unanswered for centuries.

The technological implications of this machines are far-reaching. The precision engineering and cutting-edge technologies developed for these machines have found applications in diverse industries. The design and implementation of high-gradient superconducting magnets, sophisticated radio frequency cavities, and advanced control systems have led to innovations in materials science, energy production, and aerospace engineering, driving progress in those fields.

Medicine has greatly benefited from accelerators, particularly in cancer treatment and medical imaging. Particle beams, such as protons and ions, provide a targeted and highly precise form of radiation therapy, minimizing damage to healthy tissues surrounding tumors. Additionally, accelerators produce isotopes used in medical imaging techniques, allowing for early disease detection and personalized treatment plans.

In environmental and energy research, they contribute to the development of novel materials for renewable energy technologies. Their capabilities are of great importance in understanding nuclear waste management, nuclear reactor safety, and nuclear fusion, addressing environmental concerns and fostering sustainable energy solutions.

Beyond their concrete contributions, particle accelerators play a vital role in education and human capital development. Their complexity and interdisciplinary nature attract a diverse community of scientists and engineers, fostering collaboration and knowledge exchange. As a result, a highly skilled workforce emerges, driving innovation across multiple sectors and propelling society towards greater scientific and technological achievements.

In conclusion, particle accelerators represent a cornerstone of modern society's progress and innovation. With their far-reaching implications in fundamental science, technology, medicine, energy, and environment, these sophisticated machines contribute to the scientific progress of modern society.

Many particle accelerators are immense facilities not only in size and complexity, but also in terms of energy consumption. In the current context of climate change and soaring energy prices, current and future facilities need to tackle their efficiency to ensure their viability.

While radio frequency (RF) acceleration has seen significant development over several decades, the evolving demands of future facilities are presenting fresh challenges that are driving advancements in RF acceleration technology. The pursuit of efficient high-gradient RF structures and systems stands as one of the five critical domains identified by the European Strategy for forthcoming facilities [2], needing continued research and development efforts.

In low beam-loading superconducting radio frequency (SRF) accelerators, controlling the detuning of the resonators allows the reduction of the overcoupling, which is mainly given to manage for the expected detuning level of a cavity. Reducing the detuning reliably to an insignificant level will allow to operate cavities at low bandwidth, meaning high loaded quality factor ($Q_L$). When the quality factors are optimized, the power consumption required to attain a specific level of accelerating field diminishes, resulting in a reduction in RF cost and the possibility of using solid state amplifiers, which are cheaper and more versatile than klystrons. This translates into lower installation budget and lower operational costs and environmental impact.

Cavities that are being operated with such $Q_L$ are specially susceptible to a phenomenon called microphonic detuning [63], which refers to the detuning caused by mechanical oscillations that couple to the accelerating structures and impact their energetic efficiency and field stability. These mechanical disturbances micro-metrically alter the geometry of the cavities, shifting the resonance frequency of the accelerating mode with respect to the nominal frequency. This deformation generates a drift in the phase and amplitude of the electromagnetic field inside the resonator that has traditionally been corrected by the Low Level Radio Frequency (LLRF) control system at the cost of injecting more RF power. Such vibrations can arise from various sources, including ambient acoustic noise, Lorentz forces and mechanical resonances in the accelerator components.

Several prominent accelerator facilities worldwide employ high loaded Q factors in low-intensity beam experiments. The HIE-ISOLDE project aims to upgrade the ISOLDE radioactive beam facility at CERN by adding a superconducting linear accelerator (LINAC) among other things. The intended operating point for this accelerator falls in the range of $Q_L = 1 \cdot 10^7 - 3 \cdot 10^7$, with a corresponding cavity bandwidth of 3 to 10 Hz [53], which makes the subject of microphonics one of the main challenges to overcome. On the other hand, in the case of the Large Hadron-electron collider (LHeC) [39], the possibility of using Energy recovery linacs (ERL) such as the one developed in the BERlinPro project is being considered [1] in order to accelerate electrons. For this purpose, a high power energy recovery facility called PERLE has been proposed, in which negligible beam loading and high $Q_L$ are expected to be used [56]. Another clear example of the necessity of high $Q_L$ operation in low beam loading applications is the possible upgrade of the European XFEL to Continuous Wave (CW) [6]. For this purpose, the cavities are expected to operate with $Q_L$ values between $10^7$ and $10^8$ and field gradients higher than 16 MV/m.

## CHAPTER 2

# SRF RESONANT CAVITIES AND DETUNING

In this section, the principles governing the operation of SRF cavities will be reviewed and the origin and cause of detuning will be explained. Acquiring a comprehensive understanding of the problem will facilitate a smoother navigation through potential difficulties. Thus, the study will be initiated by examining the electromagnetic fields generated in the most commonly used cavities and resonance modes, verifying the strong dependence of these fields on the geometry of the cavity and defining important concepts for the study of these devices. Afterwards, the problem of detuning will be explained, as well as its main causes and effects. SRF cavities are particularly sensitive to this problem, so the most important characteristics of these machines will be studied. Finally, a study of the state of the art will be carried out in order to know in which particular cases the detuning control is especially relevant and which are the control techniques used to date.

## 2.1 | RESONANT CAVITIES

High-energy particle accelerators, whether circular or linear, use resonant cavities as a fundamental element of acceleration. Those devices are typically constructed using conductive materials and have specific dimensions that allow them to support standing or travelling waves at particular frequencies. In this chapter we will focus on the cavities that work with standing waves, as these are the ones that will be worked with throughout this thesis.

The standing waves occur when the wavelength of the injected RF signal fits precisely within the dimensions of the cavity, causing constructive interfer-

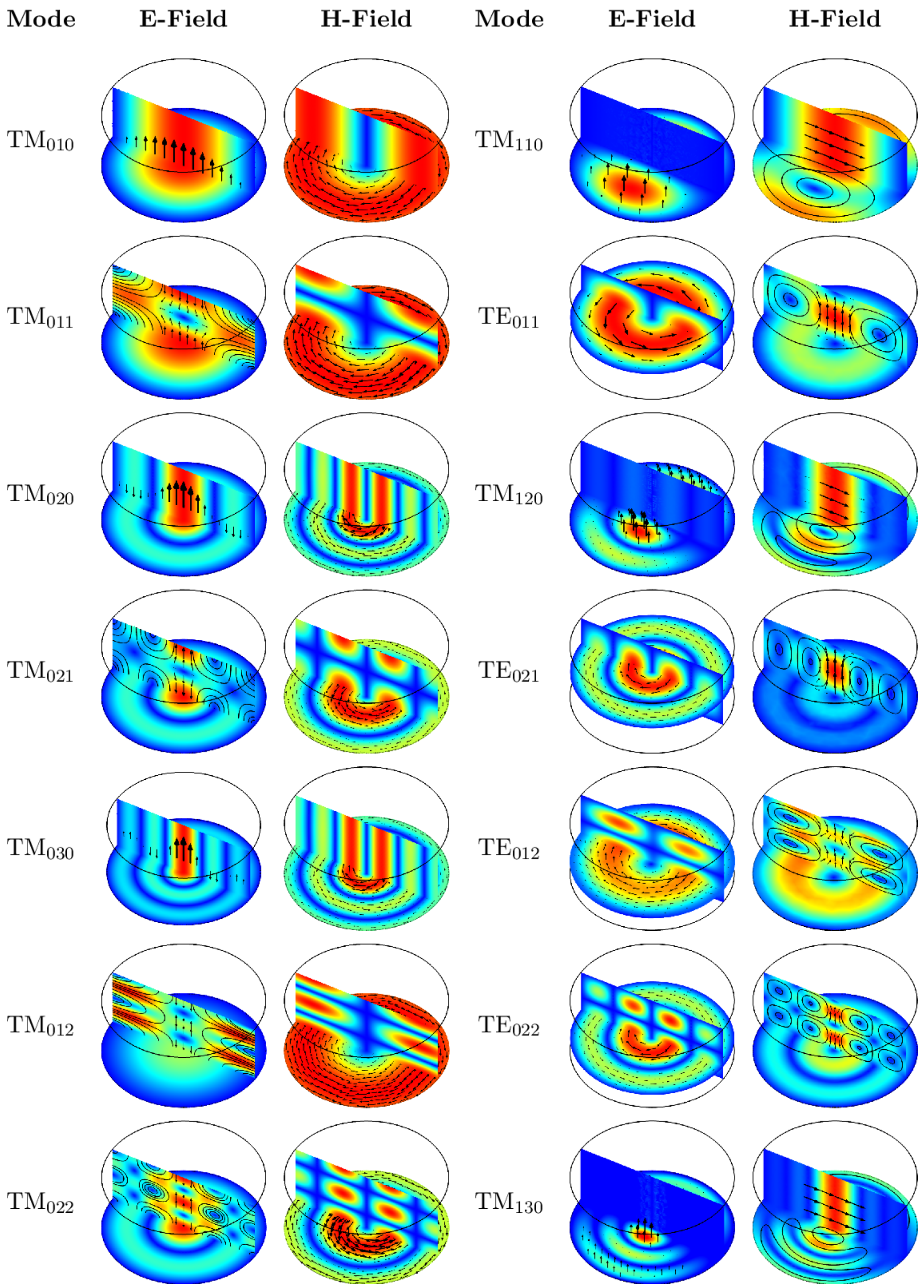

Figure 2.1.: Electromagnetic fields arrangement for several resonant modes of an ideal cylindrical cavity [20].

ence. When resonance is achieved, the energy of the incoming wave becomes concentrated within the cavity, leading to increased electric and magnetic field strengths. In this way it is possible to generate much larger electromagnetic field gradients using substantially less energy than with constant electromagnetic fields.

The geometry of the resonant cavity is crucial in determining its resonant frequencies and resonant modes. In this way, cavities support multiple modes of resonance, each corresponding to a specific pattern of standing waves. These modes are characterized by the arrangement of electromagnetic field lines within the cavity and each of them has a specific resonant frequency and energy distribution. Figure 2.1 shows the electromagnetic field distribution for the first resonant modes of an ideal cylindrical cavity.

A more detailed study of the resonance modes of a cylindrical cavity is given in appendix A, in particular the $TM_{0n0}$ modes are studied. The analysis of this type of cavity and modes is of particular importance for understanding the operation of more modern cavities such as elliptical SRF cavities and to fully understand the dependence of the resonant frequency on the geometry of the device.

## 2.2 | SRF RESONANT CAVITIES

One of the pressing problems of large acceleration facilities is their immense construction cost and energy consumption. This is why one of the main objectives of the scientific community is based on reducing the investment and operation costs of large accelerators.

In order to achieve higher energies for relatively light particles, like electrons, linear accelerators (Linacs) are often used. In this type of facilities, the investment costs are proportional to the length of the machine and since particles only traverse each accelerating section once, it is essential to have high accelerating gradients in order to minimize the length of the accelerator.

Another demanding need is to keep the mains power as low as possible for a given beam current and particle energy. In other words, the efficiency of transforming mains power to beam power should be at maximum.

In principle, RF super-conductivity provides a technical solution for both constraints, i.e. a high accelerating gradient and high mains-to-beam-power conversion efficiency [94].

Thereby, SRF cavities are nowadays used in a broad range of applications in which high accelerating gradients in CW are needed.

Although there are several types of SRF cavities, this section will focus on analysing the operation of cavities with elliptical geometry, and more specifically the TESLA cavity.

### 2.2.1 | QUALITY FACTOR AND CAVITY BANDWIDTH

The quality factor of a resonator refers to the efficiency with which it is able to store energy. In the case of SRF cavities this value may exceed $10^{10}$ due to almost non-existent resistive losses.

The electrical resistance $R_s$ of the a superconducting cavity for RF currents is defined by a temperature-dependent term $R_{BCS}$ and a temperature-independent residual resistance $R_{res}$ (See Appendix B.1).

$$R_s(T) = R_{BCS}(T) + R_{res} \tag{2.1}$$

When a resonance mode is excited, magnetic fields tangential to the cavity walls are generated, which in turn produce induced currents and, subsequently, resistive losses. The power dissipated ($P_{diss}$) on the walls of the cavity can be expressed by the following surface integral.

$$P_{diss} = \frac{1}{2}\int\int \bar{H}R_s ds \tag{2.2}$$

Thus, one may define an intrinsic quality factor $Q_0$ by

$$Q_0 = \frac{\omega_0 E_{st}}{P_{diss}} \tag{2.3}$$

where $E_{st}$ is the energy stored inside the cavity and $\omega_0$ the resonant frequency of the excited mode. Note that for each resonance mode, the intrinsic quality factor of the cavity is different, although, from now on, it will be taken as constant since the fundamental mode $TM_{010}$ oscillating at 1.3 GHz will be taken as a reference. This is the resonance mode and resonance frequency at which TESLA cavities operate.

In cavities such as the TESLA, the intrinsic quality factor can reach values of the order of $10^{10}$ and is mainly limited by the characteristics of the superconducting material itself. Even so, as the acceleration gradient approaches the maximum allowed by the superconductivity limit of the material (50-60 MV/m for TESLA cavities), the intrinsic quality factor tends to degrade to a large extent. (See Appendix B.2).

Resistive losses are not the only loss mechanism of a cavity. The coupling by the input power coupler determines the amount of power leaking back into the cavity transmission line. These losses may be described by the external quality factor $Q_{ext}$.

$$Q_{ext} = \frac{\omega_0 E_{st}}{P_{ext}} \tag{2.4}$$

where $P_{ext}$ encompasses all external power losses.

Finally, as a result of the interplay between the particle beam and the cavity field, a fraction of the stored energy is transferred to the beam, being the gained energy due to the acceleration. As a consequence, a quality factor referring to this phenomenon of beam loading can also be introduced through the equation:

$$Q_b = \frac{\omega_0 E_{st}}{P_b} \tag{2.5}$$

$P_b$ represents the power lost due to the beam loading effect, which is special relevance in high beam current accelerators.

All loss effects may be summarized by a general quantity describing the quality factor of a cavity resonance diminished by the external effects. This is the so-called loaded quality factor ($Q_L$) and determines the bandwidth of the RF resonance.

$$Q_L = \frac{\omega_0 E_{st}}{P_{diss} + P_{ext} + P_b} \tag{2.6}$$

Or in other terms:

$$\frac{1}{Q_L} = \frac{1}{Q_0} + \frac{1}{Q_{ext}} + \frac{1}{Q_b} \tag{2.7}$$

Similarly, the half bandwidth of a cavity resonance is defined as the point where the power, which is proportional to the square of the voltage, drops by 3 dB. The half-bandwidth can be expressed by the following expression.

$$\omega_{1/2} = \frac{\omega_0}{2Q_L} \tag{2.8}$$

As can be seen, the higher the loaded quality factor, the lower the cavity bandwidth.

The shunt impedance $R_{sh}$ is another figure of merit related to the power dissipation of the cavity and it measures the effectiveness of producing an axial accelerating voltage $V_{cav}$ for a given power dissipation.

$$P_{diss} = \frac{V_{cav}^2}{R_{sh}} \tag{2.9}$$

A related quantity is the geometric shunt impedance $R_{sh}/Q_0$, which depends only on the cavity's shape (1048 Ω for TESLA cavities) and can be obtained by combining equation (2.9) with the definition of $Q_0$:

$$\frac{R_{sh}}{Q_0} = \frac{V_{cav}^2}{\omega_0 E_{st}} \tag{2.10}$$

## 2.2.2 | EQUIVALENT RLC CIRCUIT

In order to study the electromagnetic dynamics of a SRF cavity, the whole accelerating system can be modeled using an equivalent electric circuit [81] where the cavity is modeled by a resonant $RLC$ circuit, being R, L and C the the equivalent resistance, impedance and capacitance of the cavity, respectively. The power amplifier and the beam are represented as current generators and the fundamental power coupler as an ideal transformer, with a winding ratio of 1:m. The power source is connected to the coupling antenna via a matched transmission line with impedance $Z_0$, which may vary between 50 and 75 Ω depending on the waveguide used.

Any mismatch between the cavity and source impedances leads to a reflection of a part of the forward power wave at the coupler. As this reflected wave may destroy the RF source, the backwards traveling wave is redirected by a circulator into a matched load. Figure 2.2 shows the equivalent circuit of the fundamental mode of a cavity connected to a RF power source, where $V_{cav}$ represents the transmitted voltage to the cavity and $V_{ref}$ the reflected voltage sent to the circulator.

According to this scheme, the input coupler relates the waveguide side and cavity side currents and voltages by the transformation equations:

$$V' = mV \tag{2.11}$$

$$I' = mI \tag{2.12}$$

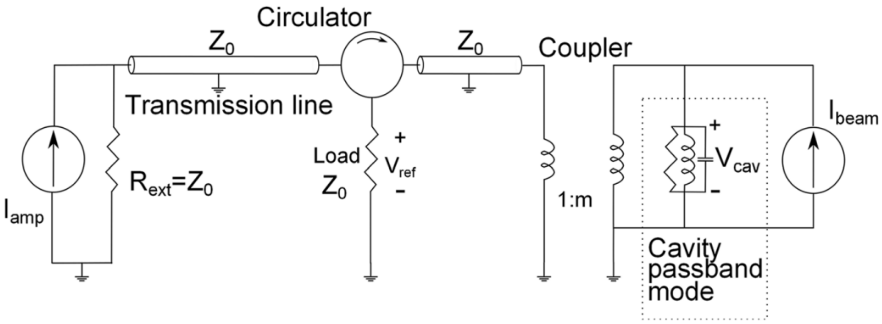

Figure 2.2.: Equivalent circuit model for a cavity accelerating a particle beam and connected via a coupler antenna to an RF power source [24].

Thus, the impedance of the waveguide side seen from the cavity can be defined as follows:

$$Z' = m^2 Z \tag{2.13}$$

All primed quantities refer to the cavity side. Thus, the power dissipated outside the cavity $P_{ext}$, i.e. at the load of the circulator, can be defined as the square of the cavity RMS voltage $V_{RMS}$ divided by the external impedance $Z_{ext} = m^2 Z_0$. Considering that the cavity voltage is sinusoidal, the RMS voltage can be expressed as $V_{RMS} = V_{cav}/\sqrt{2}$. In this way, the external dissipated power is defined as follows:

$$P_{ext} = \frac{V_{cav}^2}{2m^2 Z_0} \tag{2.14}$$

Similarly, the power dissipated in the cavity walls $P_{diss}$ can be defined as:

$$P_{diss} = \frac{V_{cav}^2}{2R} \tag{2.15}$$

Note that the power dissipated inside the cavity is exclusively dependent on the characteristics of the device, i.e. it solely depends on the intrinsic quality factor of the cavity $Q_0$. On the other hand, the power dissipated in the external load depends on the degree of coupling between the cavity and the RF power circuit. The coupling factor $\beta$ is used to quantify that degree of coupling, and is defined as the ratio of the power loss in the external circuit to that in the cavity.

$$\beta = \frac{P_{ext}}{P_{diss}} = \frac{R}{m^2 Z_0} \tag{2.16}$$

The equivalent circuit components are defined in terms of the cavity parameters as follows [81]

$$\sqrt{\frac{L}{C}} = \frac{R}{Q_0} \tag{2.17}$$

$$\omega_0 = \frac{1}{\sqrt{LC}} \tag{2.18}$$

$$R_{sh} = 2R \tag{2.19}$$

At the same time, The ratio of the transformer, $m$, can be given in terms of coupling factor of the fundamental power coupler $\beta$.

$$m = \sqrt{\frac{R}{\beta Z_0}} \tag{2.20}$$

Note that the transformed external load $Z_{ext}$ acts as a parallel resistor to the cavity resistor $R$. Therefore, those two elements can be replaced by a single resistor $R_L$, known as the loaded impedance.

$$\frac{1}{R_L} = \frac{1}{R} + \frac{1}{m^2 Z_0} \tag{2.21}$$

This $R_L$ can also be defined as:

$$R_L = \frac{R}{1+\beta} = \frac{R_{sh}}{2(1+\beta)} \tag{2.22}$$

In a similar way, $Q_L$ can be described as:

$$Q_L = \frac{Q_0}{1+\beta} \tag{2.23}$$

Now that all the parameters of the equivalent circuit are defined as a function of cavity quantities, it is possible to solve the time evolution equation of the system to analyse its dynamics. As it is shown in Figure 2.3, the starting circuit can be simplified to a externally driven RLC circuit.

Applying Kirchhoff's law for currents, it is obtained that the incident current in the RLC circuit, $I(t)$, is equal to the sum of the currents through the capacitor $I_C(t)$, the resistor $I_{R_L}(t)$ and the coil $I_L(t)$.

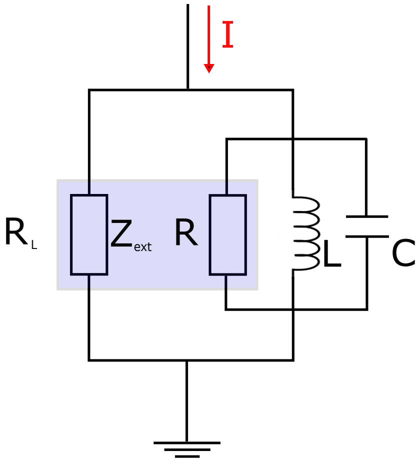

Figure 2.3.: Simplified RLC circuit representing a fundamental resonance mode of a cavity.

$$I(t) = I_{R_L}(t) + I_C(t) + I_L(t) \tag{2.24}$$

Given the definition of the current through those elements, the equation can be rewritten as follows:

$$I(t) = C\frac{dV_C(t)}{dt} + \frac{V_{R_L}(t)}{R_L} + \frac{1}{L}\int V_L(t)dt \tag{2.25}$$

Note that the voltage dropping on the resistor $V_{R_L}$, on the coil $V_L(t)$ and on the capacitor $V_C(t)$ are equal and the same as the cavity voltage $V_{cav}$. Thus, by deriving the function (2.25) with respect to time and substituting $V_{cav}$, we obtain the following differential equation that defines the time evolution of the cavity voltage as a function of the incident current.

$$\ddot{V}_{cav}(t) + \frac{1}{R_L C}\dot{V}_{cav}(t) + \frac{1}{LC}V_{cav}(t) = \frac{1}{C}\dot{I}(t) \tag{2.26}$$

Using the previously discussed relationships between circuit parameters and cavity quantities, the time evolution equation of the cavity voltage results in the following formula:

$$\ddot{V}_{cav}(t) + \frac{\omega_0}{Q_L}\dot{V}_{cav}(t) + \omega_0^2 V_{cav}(t) = \frac{\omega_0 R_L}{Q_L}\dot{I}(t) \tag{2.27}$$

This is the general form of an externally driven damped harmonic oscillator.

Therefore, if the applied current $I(t)$ is harmonic, i.e. $I(t) = I_0 sin(\omega t)$, the driving term of the right side of the equation is proportional to $cos(\omega t)$, and the particular solution, which describes the stationary response of the system, is given by

$$V_{cav}(t) = V_0 sin(\omega t + \psi) \tag{2.28}$$

where

$$V_0 = \frac{R_L I_0}{\sqrt{1 + tan^2(\psi)}} \tag{2.29}$$

and

$$tan(\psi) = Q_L(\frac{\omega_0}{\omega} - \frac{\omega}{\omega_0}) \tag{2.30}$$

The phase angle $\psi$ is known as the tuning angle of the cavity and is defined as the phase difference between the driving current $I$ and the cavity voltage $V_{cav}$.

If the driving frequency $\omega$ is very close to the cavity resonance frequency $\omega_0$, one may rewrite equation (2.30) to:

$$tan(\psi) \approx 2Q_L \frac{\Delta\omega}{\omega_0} = 2Q_L \frac{\Delta f}{f_0} \tag{2.31}$$

where $\Delta\omega = \omega_0 - \omega$. Note that this equation is of particular relevance to this work because when detuning is sufficiently low, it can be inferred by comparing the phase of the driving signal with that of the cavity voltage (see equation (5.1)).

Under the same assumption, equation (2.29) can be rewritten as follows:

$$V_0(\Delta\omega) \approx \frac{R_L I_0}{\sqrt{1 + (2Q_L \frac{\Delta\omega}{\omega})^2}} \tag{2.32}$$

Equations (2.31) and (2.32) define the dependence of the amplitude and phase of the cavity voltage with respect to detuning, forming what is known as the Lorenz curve (see Figure 2.4).

To this point, the steady-state of the cavity has been analyzed, assuming that the driving signals, i.e. both the RF generator and the beam current, have been

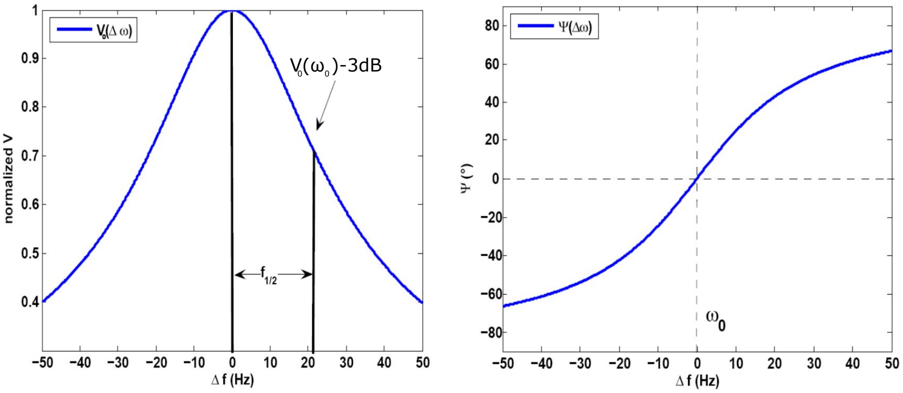

Figure 2.4.: Amplitude and phase of a cavity resonance plotted against frequency [67].

turned on for a long enough time, compared to the characteristic filling time of the cavity.

The next step is to study the transient dynamics of the cavity field. For this purpose, the differential equation (2.27), which defines the time evolution of the field $V_{cav}$, is used as a starting point.

Assuming that the driving current of the RF generator $I_g(t)$ and the Fourier component of the pulsed beam $I_b(t)$ are harmonics with a time dependence $e^{i\omega t}$, the driving current of the cavity $I(t)$ can be represented as a phasor multiplying a complex exponential.

$$I(t) = I_g(t) + I_b(t) = [I_{re}(t) + iI_{im}(t)]e^{i\omega t} \tag{2.33}$$

where $I_{re}$ and $I_{im}$ are the real and imaginary components of the driving current signal. Taking this current as the input signal to the system, the voltage output $V_{cav}$ can be represented following the same formulation.

$$V_{cav}(t) = [V_{re}(t) + iV_{im}(t)]e^{i\omega t} \tag{2.34}$$

where $V_{re}$ and $V_{im}$ are the real and imaginary components of the cavity voltage. Note that, through this notation, it is possible to separate the slowly changing amplitude and phase, encoded in the phasor, from the fast RF oscillation.

The transient dynamics of a CW-driven cavity is sufficiently described by the evolution of the cavity's voltage phase and amplitude, i. e. the time varying behavior of the phasor $V_{re} + iV_{im}$. In this way, by introducing the phasors of equation (2.33) and (2.34) in (2.27) and neglecting the second order time derivatives of $V_{cav}$, since they are small compared to the lower order terms, the first order cavity differential equation for the phase and amplitude is obtained. The whole derivation can be found in Annex A.6 of [81].

$$\dot{V}_{re} + \omega_{1/2} V_{re} + \Delta\omega V_{im} = R_L \omega_{1/2} I_{re} \tag{2.35}$$

$$\dot{V}_{im} + \omega_{1/2} V_{im} - \Delta\omega V_{re} = R_L \omega_{1/2} I_{im} \tag{2.36}$$

This equations can be rewritten in the matrix form of the state space formalism as

$$\begin{pmatrix} \dot{V}_{re} \\ \dot{V}_{im} \end{pmatrix} = \begin{pmatrix} -\omega_{1/2} & -\Delta\omega \\ \Delta\omega & -\omega_{1/2} \end{pmatrix} \begin{pmatrix} V_{re} \\ V_{im} \end{pmatrix} + \begin{pmatrix} R_L\omega_{1/2} & 0 \\ 0 & R_L\omega_{1/2} \end{pmatrix} \begin{pmatrix} I_{re} \\ I_{im} \end{pmatrix} \tag{2.37}$$

Note that the real $V_{re}(t)$ and imaginary $V_{im}(t)$ components of the cavity voltage can be related to its phase $\psi$ and amplitude $V_0$ by means of the following trigonometric relationship:

$$\psi(t) = arctan\left(\frac{V_{im}(t)}{V_{re}(t)}\right) \tag{2.38}$$

$$V_0(t) = \sqrt{V_{im}^2(t) + V_{re}^2(t)} \tag{2.39}$$

For a more in-depth analysis, incorporating the pulsed beam operation and other case studies, the reader is referred to [81].

## 2.3 | TESLA CAVITIES

The TESLA cavities [4] are SRF devices that were designed in the 1990s for use in a proposed linear electron-positron collider called the TESLA Linear Collider (TLC) [12], also known as the International Linear Collider (ILC). These cavities were specifically designed to provide efficient acceleration for electron and positron beams, which would allow researchers to explore electron-positron interactions in the center-of-mass energy range from 200 GeV to more than a TeV, which can no longer be realized in a circular machine due to synchrotron radiation. The proposed TESLA Linear Collider was intended to be a successor to the Large Electron-Positron Collider (LEP) [65] and would have had the potential to reveal new physics beyond what had been discovered at previous accelerators. Although the TESLA project didn't lead directly to the construction of the International Linear Collider as originally envisioned, many of the technological developments and concepts from TESLA have influenced subsequent particle accelerator projects, including the design of SRF cavities for other accelerators. The pursuit of high-energy linear colliders continues, with projects like the Compact Linear Collider (CLIC) [89] and the International Linear Collider (ILC) still being considered for future exploration of particle physics at the highest energy scales.

## 2.3.1 | CAVITY GEOMETRY AND ACCELERATION FIELDS

The TESLA cavity is a 9 elliptical cell standing wave structure of about 1 m length whose lowest TM mode, the $TM_{010}$, resonates at 1300 MHz. This resonant mode is the one used to accelerate particles due to the arrangement of electromagnetic fields that generates inside the cavity (see Figure 2.6 and 2.8). The device is made from solid niobium and is cooled by superfluid helium at 1.8-2 K. Figure 2.5 shows the side view of the cavity structure.

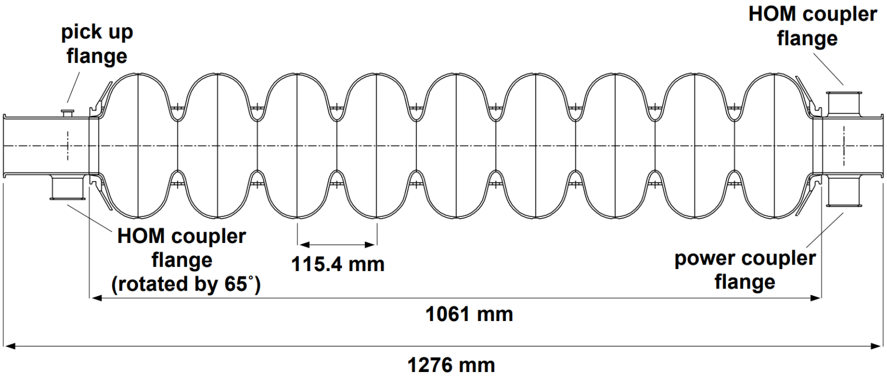

Figure 2.5.: Side view of the 9-cell TESLA cavity [4].

The reasoning behind the evolution towards elliptical geometry in the TESLA cavity is presented in the Appendix B.3, as well as the basic criteria for the design of this type of cavity.

Each 9-cell cavity is equipped with its own titanium helium tank, a tuning system that will be discussed in chapter 2.6, a coaxial RF power coupler capable of transmitting a peak power greater than 200 kW, a pickup probe and two Higher Order Modes (HOM) couplers. The main function of these couplers is to extract the energy that the particle beam can deposit in unwanted higher resonance modes, which can induce longitudinal beam instabilities and increase the beam's energy spread (See Appendix B.4).

The electromagnetic field generated in this type of resonant cells in the

$TM_{010}$ mode is similar to that of cylindrical cavities, with only azimuthal magnetic field and maximum electric field at the device axis (see figure 2.6).

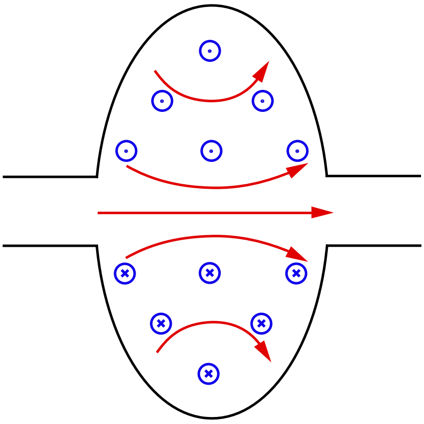

Figure 2.6.: Scheme of the electromagnetic disposition of the $TM_{010}$ mode in an elliptical cell. Electric field is represented in red and magnetic field in blue.

If feasible from both technical and performance standpoints, the utilization of multi-cell structures is advisable for minimizing the investment expenditure of an accelerator. These multi-cell structures have a lower cost per unit length and allow for higher effective gradients, which is especially relevant for linear accelerators. However, this type of structures introduce new problems to be faced, such as the increase of HOM modes, new pass-band modes, field flatness degradation and the higher sensitivity to mechanical vibrations. Those issues will be discussed in more depth further below. In the following, cell-to-cell coupling for the accelerating mode $TM_{010}$ will be examined, although many of the discussed features hold for other resonant modes.

Let's consider the scenario of coupling two identical resonators with cylindrical symmetry. This is illustrated schematically in Figure 2.7 (a), where two half-cells of an elliptical cavity are represented. The accelerating mode of each resonator has the same frequency $\omega_0$ and field pattern. When the resonators are coupled, as shown in Figures 2.7 (b) and (c), two different resonant modes emerge in the coupling region, slightly different in frequency and field pattern.

The field patterns vary in the iris region depending on whether the coupling plane aligns with the symmetry plane for the magnetic or electric field. These variations result in different stored magnetic and electric energies, leading to distinct frequencies. When there's symmetry for the magnetic field, the resonator oscillates in phase, forming the "0 mode". Conversely, when the symmetry plane corresponds to the electric field, the cavity oscillates in counter-phase, constituting the "$\pi$" mode.

As mentioned above, each of these pass-band modes has a different frequency, referred to as $\omega_0$ for mode 0 and $\omega_\pi$ for mode $\pi$. When the stored magnetic energy in the coupling region is bigger than the stored electric energy, $\omega_0$ is higher than $\omega_\pi$ and vice versa. Those cases are named as "magnetic coupling" and "electric coupling" respectively.

In an ideal case without losses, where the resonators are in a steady state and no energy dissipates via the beam, walls, or openings, no energy crosses the iris. This is because, for each mode in our example, one of the components of the Poynting vector becomes zero. The Poynting vector is defined as the cross product of the electric field and the magnetic field divided by the permeability of free space and indicates the direction and magnitude of the power per unit area carried by an electromagnetic wave. For the 0 mode, it is the radial electric field that becomes zero and for the $\pi$ mode it is the angular magnetic field. For a real structure, a linear combination of all modes is needed to enable cell-to-cell energy flow. In the considered example both 0 and $\pi$ mode must be excited, though the additional mode has much smaller amplitude.

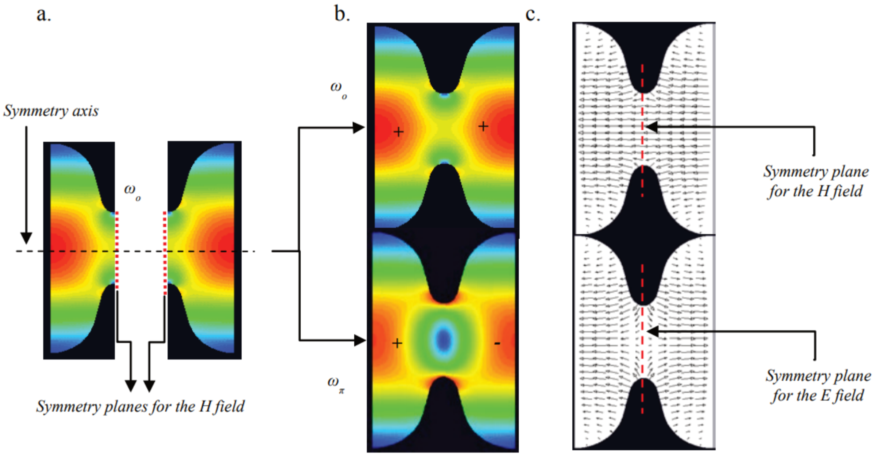

Figure 2.7.: Coupling of two resonators: (a) two identical resonators having the same frequency $\omega_0$ and field pattern before they are coupled, shown is the contour of the electric field for $TM_{010}$ mode; (b) contours of the electric field for the 0 and $\pi$ modes after two resonators have been coupled; (c) electric field lines for the 0 and $\pi$ modes [82].

An added difficulty of using multi-cell structures arises from the possible shift in the resonant frequency $\Delta\omega_i$ of the different cells. This can derive from various causes such as mechanical tolerances in the manufacturing process, or from the cooling-heating cycles. This issue is referred to as field flatness and leads to a degradation of the acceleration field.

The sensitivity of the cavity to this field flatness problem is strongly dependant on the coupling strength, which is measured by the coupling factor.

$$k_{cc} = \frac{\omega_\pi - \omega_0}{2(\omega_\pi + \omega_0)} \tag{2.40}$$

At the same time, the sensitivity of a N-cell cavity operating in $\pi$ mode is expressed by the following ratio.

$$\frac{\Delta E_{acc}}{E_{acc}} = a_{ff} \frac{\Delta \omega_i}{\omega_i} \tag{2.41}$$

Here, $E_{acc}$ and $\omega_i$ refer to the acceleration field and the resonance frequency of the cells respectively. $a_{ff}$, on the other hand, is the field flatness factor and is defined as follows:

$$a_{ff} = \frac{N^2}{k_{cc}} \tag{2.42}$$

This parameter should be small to keep the structure insensitive to random-cell frequency errors.

In weakly coupled structures, as a result of the nature of the coupling, for every resonant field pattern of an uncoupled cell, there are $n$ resonant modes of $n$ coupled cells. Those modes, differ in frequency, field amplitudes, and in cell-to-cell phase advance.

In order to accelerate particles, the $\pi$ mode of the $TM_{010}$ is normally used. As it has been previously discussed, when a cavity operates in this mode, the individual cells are resonating in counter-phase, forming the acceleration field shown in figure 2.8.

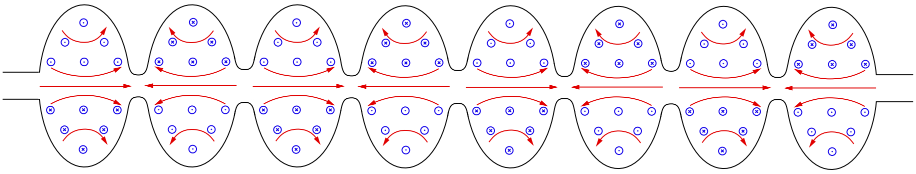

Figure 2.8.: Scheme of the electromagnetic disposition of the $TM_{010}$ $\pi$ mode in a 9-cell SRF cavity. Electric field is represented in red and magnetic field in blue.

For acceleration of particles with velocity close to $c$ ($\beta \sim 1$), the length of each cell is $l_{cell} = \beta \cdot \pi c/\omega_{acc}$. Thus, the time it takes for a particle to pass from one cell to another is equivalent to half a cycle of the acceleration field oscillation, so synchronic acceleration takes place. It is important to emphasize that for the correct acceleration of the particles, a Low Level Radio Frequency (LLRF) control system [86] is strictly necessary, which is a technology designed to ensure that the RF fields, responsible for accelerating and focusing particle beams, maintain specific characteristics like amplitude and phase.

## 2.4 | Mechanical detuning

Mechanical detuning in SRF cavities refers to a phenomenon where the resonant frequency of the cavity deviates from its desired or nominal value due to mechanical deformations or vibrations.

As in the case of cylindrical cavities (see Appendix A) and in the same way as for TESLA cavities, the electromagnetic resonance frequency is only dependent on the device's geometry. Thus, when the cavity undergoes mechanical vibration, its walls contract and expand, deforming its geometry in a few nanometers and thus deviating its nominal resonance frequency. As discussed above, this is especially detrimental in the case of SRF cavities operating at high $Q_L$, since as shown in equation (2.8), the cavity bandwidth is inversely proportional to its quality factor. TESLA cavities operate with bandwidths below 130 Hz when the $Q_L$ is greater than $10^7$, so that even the smallest deformation can generate changes in the nominal frequency of several bandwidths. In addition, the fact that TESLA cavities are multi-cell structures results in mechanical resonance modes at frequencies of even tens of hertz. In this way, these modes can be excited by external vibrations, generating a large detuning and degrading the acceleration field to a great extent. Figure 2.9 shows an example of the first mechanical resonance modes of a 5-cell elliptical cavity.

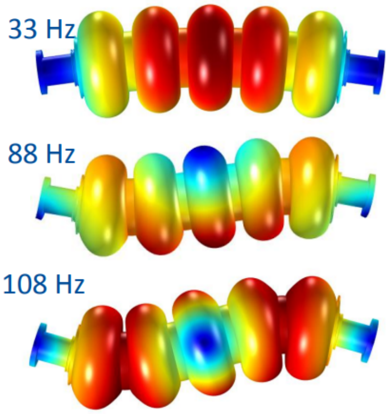

Figure 2.9.: First three mechanical modes of a five cell SRF cavity [55].

Mechanical detuning can be classified according to its origin. This classification is described in the next sections.

### 2.4.1 | LORENTZ FORCES DETUNING

One of the primary effect contributing to cavity detuning is due to the Lorentz forces acting on the cavity walls by the RF field itself. The pressure generated by the RF field is expressed in equation (2.43).

$$P_{rad} = \frac{1}{4}(\mu_0|\bar{H}|^2 - \epsilon_0|\bar{E}|^2) \tag{2.43}$$

As it can be seen, the magnetic field exerts a repulsive force proportional to the square of its modulus, while the electric field attracts the walls with a force also proportional to the square of its modulus. Considering the distribution of the electromagnetic fields in the fundamental resonance mode $TM_{010}$ the cells deform inward near the iris, while expanding outward at the equator, as shown in Figure 2.10. Overall frequency shift will always be negative since the repulsive magnetic field forces and the attractive electric field forces both work together to decrease the resonance frequency of the deformed cavity.

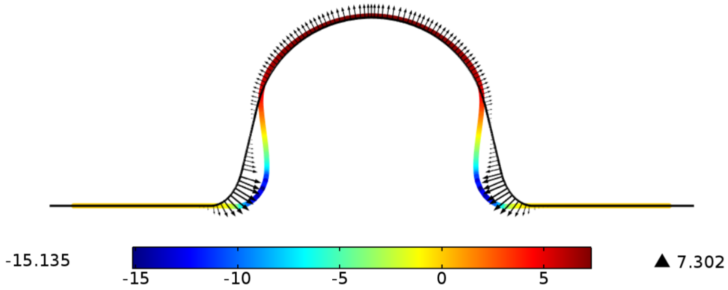

Figure 2.10.: Lorentz forces exerted on a 650 MHz $\beta$=0.9 single cell cavity ahead with the radiation pressure values in mbar at the 3.5 MV cavity voltage. Deformation is exaggerated by 20000 times [55].

The radiation pressure generates a change of the cavity's volume ($\Delta V$) causing a shift of the resonance frequency given by Slater's formula [88]. This phenomenon is called Lorentz force detuning.

$$\frac{\Delta\omega}{\omega} = -\frac{\int_{\Delta V}(\mu_0|\bar{H}|^2 - \epsilon_0|\bar{E}|^2)dV}{\int_V(\mu_0|\bar{H}|^2 + \epsilon_0|\bar{E}|^2)dV} \tag{2.44}$$

Here, $\bar{H}$ and $\bar{E}$ are the unperturbed field values and the denominator is the stored energy in the resonator.

Lorentz force detuning is of particular concern in cavities operating in pulsed mode, since periodic RF strokes can excite mechanical resonance modes of the device. It can also be problematic in accelerators operating with high beam loading, as the wakefield generated by the particle beam and the drastic absorption of energy can also excite unwanted mechanical resonance modes. In the case studied in this work, the cavity operates in CW, so that the Lorenz forces, by themselves, are not particularly harmful, since they generate a static detuning that is relatively easy to correct. Even so, they are partly responsible for the ponderomotive effect that will be presented later in this chapter.

## 2.4.2 | MICROPHONIC DETUNING

The term microphonics refers to any external mechanical disturbance that affects the geometry of the resonant cavity. External vibrations caused by heavy machinery like the pumps for the liquid helium system or vacuum pumps may be transmitted through the supply lines, the beam pipe or the ground, affecting directly to the accelerating structure. In the case of this type of disturbances generated by rotatory machinery, they usually have a constant oscillatory spectrum and is relatively easy to control by feed forward (FF) algorithms. The term "feed forward" refers to the fact that the control action is applied based on the known or anticipated input to the system, with the goal of directly compensating for the expected disturbances or changes. In a FF control system, the controller generates a control signal based on the anticipated disturbance before the system responds to it. A clear example of this technique is shown in [7], where a Narrow badwidth Active noice control (NANC) based in FF principles is applied to the SRF cavities of LCLS-II.

In addition to that, ground motion has the potential to propagate into the cavity system. The sources of this natural noise are given by seismic activities of the ground and ocean waves and have wavelengths up to several hundred meters with frequencies below 1 Hz [5]. These external sources of noise undergo partial filtration by the transfer medium. To address this, specifically designed passive supports are positioned beneath the pumps, and flexible bellows are integrated into any pipe that links vacuum pumps to the cryostat. These measures are implemented to facilitate damping.

Another source of noise arises from the helium cooling system used to maintain superconducting conditions within the cavities. Variations in pressure within the cryogenic system or alterations in the liquid helium level in the two-phase line lead to modifications in the forces exerted on the cavity walls. Also, Thermo-acoustic fluctuations arising from enclosed volumes in the cryo-plant

[95] trigger pressure waves. This will directly act as an isotropically distributed force onto the cavity via the helium transfer line. Additionally, during high-power operation, there is a potential for boiling to take place in the superfluid helium, which could transmit vibrations to the cavity structure. This kind of microphonics are much harder to control due to their stochastic nature. For this purpose, feedback control systems are used, but as will be shown throughout the study, this is difficult due to the low relative stability of the cavities from the mechanical standpoint.

### 2.4.3 | Ponderomotive effect

A phenomenon that is likely to impact the stability of the field in CW mode-driven cavities is the interaction between mechanical detuning and time-varying Lorentz forces. When combined with an RF feedback system in a setup where a generator maintains a fixed reference frequency, this interaction has the potential to induce undesired oscillations in both the amplitude and phase of the RF field, particularly if there is a significant amount of RF power available for compensation [22, 69].

In essence, two scenarios are conceivable, and these have been substantiated through measurements conducted at the ELBE radiation source linear accelerator [13]. In a scenario where the klystron (the power amplifier for the RF signal) operates near its saturation point, either positive or negative detuning from the resonance frequency can arise induced by microphonics.

In the case of a positive frequency shift, the RF field experiences a decay due to this detuning effect. Consequently, the low-level RF system endeavors to counterbalance the diminishing field amplitude by increasing the required forward power, and the klystron saturates. However, since there is no additional RF power available, the field amplitude diminishes further. This progression contributes to a subsequent positive detuning, owing to the fact that the reduced field level is accompanied by a diminished negative Lorentz force detuning offset. Even if the microphonics-induced detuning event that initiated this process were to decrease, the RF field might fail to recover. It has now strayed too far from resonance, causing the klystron to persist in a saturated state and the field strength to diminish to a minimal level.

When the resonance frequency experiences a negative shift, it leads to an observable oscillatory instability. The disruption caused by microphonics-induced perturbations is counteracted by the Lorentz force detuning as the field amplitude begins to decrease. The directional nature of the ponderomotive effect arises from the negative correlation inherent in the Lorentz force detuning.

At the ELBE linear accelerator, the measurement of this effect was only feasible during an RF pulse lasting approximately 50 ms. The ELBE cavity, shaped in accordance with the TESLA design, consists of nine cells and operates as a superconducting cavity. Figure 2.11 shows the measured ponderomotive effect for both positive and negative frequency shift cases [67].

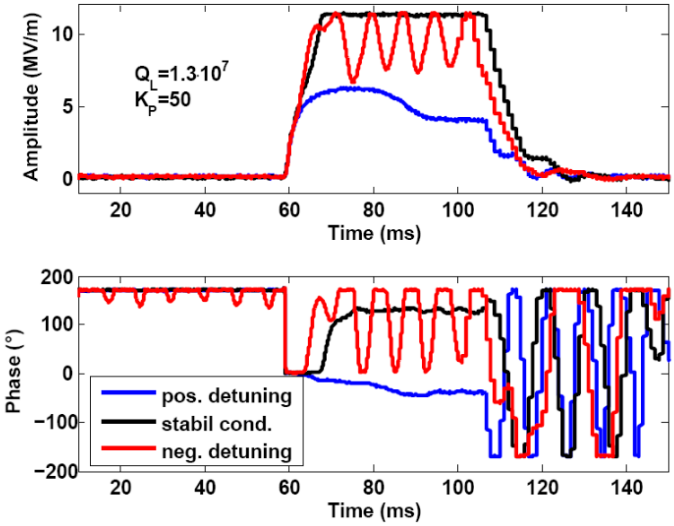

Figure 2.11.: Measurement of ponderomotive effect (red line) at the ELBE linac in [67]. A saturation of the klystron due to microphonics detuning leads to a decay (blue curve) or oscillation (red curve) of the field amplitude depending on the direction of the microphonics that triggers the effect. As a reference measurement the stable case is given (black curve). The data have been sampled at a set point field level of 11.5 MV/m and a loaded quality factor of $1.3 \cdot 10^7$.

In the graph, the stable condition is represented by the black curve, which involves driving the cavity at 11.5 MV/m while maintaining a loaded quality factor of $1.3 \cdot 10^7$. For this particular test, the maximum klystron power had been restricted to 10 kW. On the other hand, the blue curve showcases the outcome when there is positive detuning due to microphonics-induced klystron saturation. In this case, the desired field gradient is never achieved, and the field strength declines to around 5 MV/m. In contrast, when there is negative detuning, the anticipated oscillatory behavior has been verified through measurements, as illustrated by the red curve.

It is worth mentioning that, like the Lorentz forces, the ponderomotive effect is a nonlinear phenomenon that must be controlled using specific techniques.

## 2.5 | RF POWER REQUIREMENTS AND DETUNING

The input power $P_f$ requirement to maintain a constant electromagnetic field in an CW operating SRF cavity, is mainly determined by its operation characteristics and the peak detuning $\Delta f$ it is subject to. Equation (2.45) displays such dependence [67]:

$$P_f = \frac{V_{cav}^2}{4\frac{R}{Q}Q_L}[(1 + \frac{\frac{R}{Q}Q_L I_b}{V_{cav}} cos(\Phi_b))^2 + (\frac{\Delta f}{f_{1/2}} + \frac{\frac{R}{Q}Q_L I_b}{V_{cav}} sin(\Phi_b))^2] \tag{2.45}$$

where, as stated in section 2.2.1, $V_{cav}$ is the desired cavity voltage, $Q_L$ is the loaded quality factor, $f_{1/2}$ is the cavity half bandwidth and $R/Q$ is the geometric shunt impedance, which are parameters related with the cavity and its operation. On the other hand, $I_b$ and $\Phi_b$ are parameters related with the beam, representing the average beam current and the synchronous phase respectively. The latter is defined as the relative timing between the accelerating electric field and the beam and determines the acceleration field perceived by the particles as they cross the cavity.

Analyzing equation (2.45) it is obtained that when the beam loading is large, it is necessary to limit $V_{cav}$ and to some extent $Q_L$ to keep the energy consumption in feasible values. Figure 2.12 shows the forward power requirements to maintain different cavity voltages as a function of the loaded quality factor, when beam loading is high ($I_b = 50mA$). For that case, peak detuning was set at 10 Hz and the synchronous phase at 0°.

As it is shown in figure 2.12, the power requirements for a relatively low cavity voltage of 8 MV/m is around 40 KW, at an optimal $Q_L$ of approximately $10^6$. Thus, in applications with high beam loading, the acceleration gradient must be kept at conservative values to avoid unfeasible energy consumption. This also means that the $Q_L$ used for such applications is relatively low, and consequently, the machines operating under these characteristics are not as sensitive to detuning.

However, in applications where the beam loading is negligible, the power required to maintain a certain acceleration gradient is almost solely dependent on the detuning over the half-bandwidth squared. This means that for a small bandwidth, i.e. high $Q_L$, the system is extremely sensitive to detuning and significant power overhead is required by the RF control process to compensate. In turn, this also means that for this type of application, extremely high energy

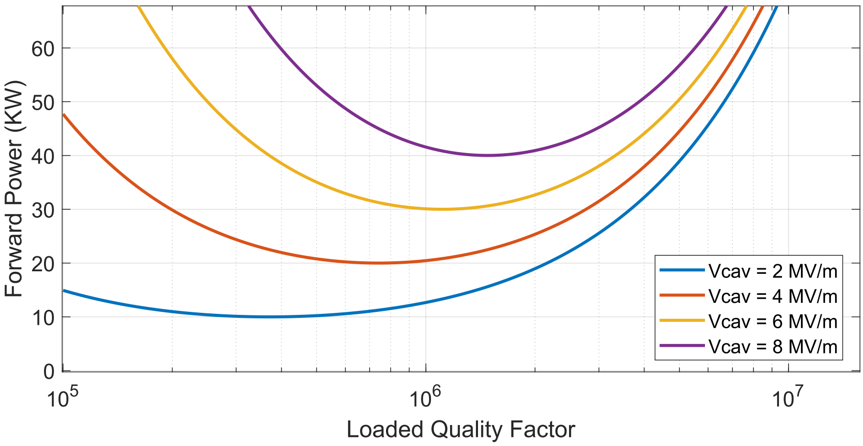

Figure 2.12.: Forward RF power $P_f$ as a function of loaded quality factor $Q_L$ for different $V_{cav}$ values and a beam intensity of $I_b = 50$ mA.

efficiencies can be achieved if the peak detuning is reduced to small enough values.

Figure 2.13 shows the forward power required to maintain a $V_{cav}$ of 16 MV/m as a function of the loaded quality factor $Q_L$ for different amounts of peak detuning $\Delta f$. Beam current $I_b$ and synchronous phase $\Phi_b$ are maintained constant with values of 75 µA and 0° respectively.

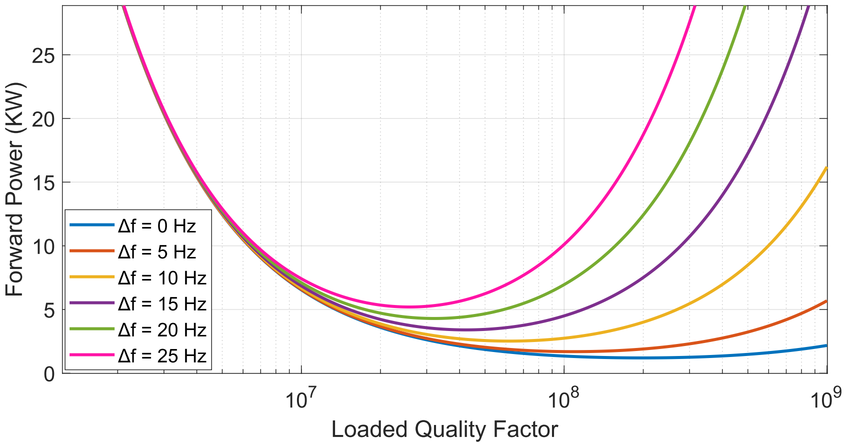

Figure 2.13.: Forward RF power $P_f$ as a function of loaded quality factor $Q_L$for different $\Delta f$ values and a beam intensity of $I_b = 75\ \mu A$.

This shows the significant improvement in energy efficiency that can be obtained by suppressing detuning in low beam loading applications.

## 2.6 | Tuning systems

As shown in Appendix A for a cylindrical cavity, the resonant frequency of an SRF cavity is determined by its physical dimensions, such as the length and shape. When the cavity undergoes mechanical perturbations the geometry of the device changes, generating a deviation in the resonant frequency called detuning. In this way, achieving and maintaining the desired resonant frequency is essential for optimal performance. A tuner is an actuator, that allows for real-time adjustment of the cavity's resonant frequency to ensure proper synchronization with the injected RF power signal. The tuner is also used to detune the cavities far off resonance in the event of failure to avoid damage to the device.

Typically, tuners have to deal with two different types of detuning. On the one hand, slow or static detuning, which is a constant or very slow frequency shift that is consequence of cavity manufacturing tolerances, the cooling process of the device or Lorentz forces in the case of continuous wave operation. On the other hand, there is fast detuning, which is caused by dynamic mechanical pertubations such as pressure changes in the liquid helium bath, seismic movements, vacuum pumps or Lorentz forces in the case of pulsed operation.

The most commonly used actuators in the case of static detuning are stepper motors and DC motors [85]. In order to compensate the detuning, tuners are designed to transfer the rotary motion of the motor to elongate or shorten the cavity by means of different mechanisms. These mechanisms depend on the design of the tuner itself as will be discussed later.

In the case of fast detuning compensation, piezo-actuators are the most commonly used devices [21]. Piezo-electric actuators are transducers that convert electrical energy into a mechanical displacement or stress based on a piezoelectric effect, which is a phenomenon in which certain materials undergo a mechanical deformation when an electric field is applied to them. They are used in fast detuning control since they are a high precision positioning mechanism that can control a small mechanical displacement at high speed, with the advantages of large generated force (3-4kN for a stack with a cross-section of 1cm$^2$) and stable displacement [74]. As in the case of stepper motors, these actuators elongate or shrink the cavity depending on the detuning to be compensated, although in this case, they can act in a bandwidth of hundreds of Hz. Figure 2.14 shows a P-844K075 custom piezo-electric actuator used in the tuner system on LCLS-II.

Magnetostrictive actuators are another less used option for fast detuning control. The basis for their operation is the magnetostrictive effect, which refers to the change in shape or dimensions of a material when it is subjected to a magnetic field. When an external magnetic field is applied to a magnetostrictive material, it causes the magnetic moments to align with the field, which at the

Figure 2.14.: P-844K075 custom piezo-electric actuator manufactured by PI for LCLS-II [74].

same time changes the magnetic energy of the material. In order to minimize this energy change, the material undergoes mechanical deformation, which results in a change in the material's dimensions. The goal is to induce controlled mechanical deformation in the tuning element to adjust the resonant frequency of the system, by applying a controlled magnetic field by means of a superconducting coil [51]. Those kind of actuators offer a larger tuning range when compared to piezo-electrics, but they have lower tuning speed. Generating an accurate magnetic field also involves additional challenges. Figure 2.15 shows an industrial magnetostrictive actuator.

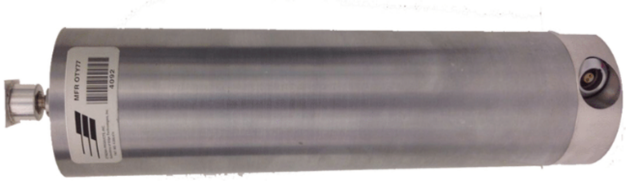

Figure 2.15.: Industrial magnetostrictive actuator [26].

However, correcting fast frequency variations with mechanical systems is inherently difficult, in fact, for the fastest variations such as transient beam loading, it is essentially impossible. As a result, the most common way to overcome fast frequency shifts is by a combination of overcoupling the fundamental power coupler in order to broaden the resonance and using extra RF power. This is why a major research effort is currently underway to develop non-mechanical fast tuners. A clear example of this is the Ferro-electric fast reactive tuner or FE-FRT [83]. Fundamentally FE-FRTs work by passing RF power through a transmission line containing ferroelectric material and reflecting it back to the cavity. The permittivity of the ferroelectric is controlled by applying a high voltage signal across the ferroelectric, altering the RF path length. This causes the phase of the RF fields and the reactance of the tuner as seen by the cavity to change, altering the frequency of the cavity without affecting its geometry [84]. Although this is an innovative technology that promises bandwidths several orders of magnitude greater than those achieved with mechanical actuators, it still requires further research and refinement. One of the biggest hurdles to overcome is the substantial RF power losses generated by the device. Figure 2.16 shows a proof of principle FE-FRT designed in [83] and successfully tested on an SRF cavity at CERN.

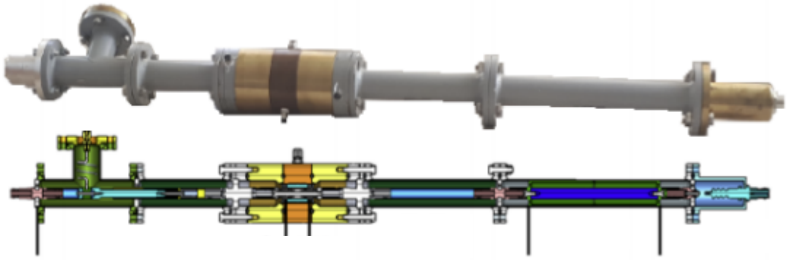

Figure 2.16.: Proof of principle FE-FRT [83].

As discussed above, SRF cavity tuners use a combination of the mentioned actuators to keep detuning levels as low as possible. The geometry and operating principles of two of the most commonly used tuners, the blade tuner and the double lever tuner developed at SACLAY, are described below.

The blade tuner is a device consisting of three concentric rings that are placed around the shell covering the cavity [11]. The outer rings are firmly attached to the cryostat, which in turn is connected to the cavity at its ends (see figure 2.17). It is worth mentioning that for the application of this type of tuner, a modified He tank, with a central bellow to allow for coaxial displacement is needed.

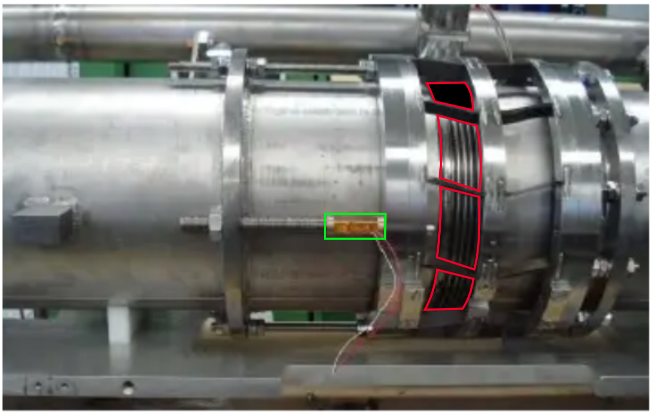

Figure 2.17.: Tuner installed on the helium tank at DESY HALLE III machine shop. Piezo-actuator is highlighted in green and flexible bellow in red [59].

The central ring is divided into two equal parts, and is connected to the outer rings by welded blades at an angle, which transforms the azimuthal rotation (in opposite directions) of the two halves of the central ring into a variation of the distance between the end rings. This axial displacement elongates or shrinks the cavity depending on the detuning to be compensated for. Figure 2.18 shows the kinetics of the mechanism governing the blade tuner.

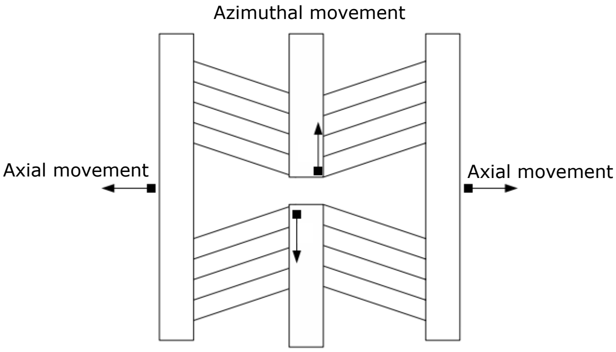

Figure 2.18.: Cinematic description of the blade tuning system [73].

As it is shown in figure 2.19, the azimuthal rotation is provided by a leverage system connected to a stepping motor. The fast actuator is implemented by inserting elements between one of the end rings and the corresponding flange on the He vessel. Figure 2.17 shows the piezo in place in the tuner installed on the helium tank at DESY HALLE III machine shop.

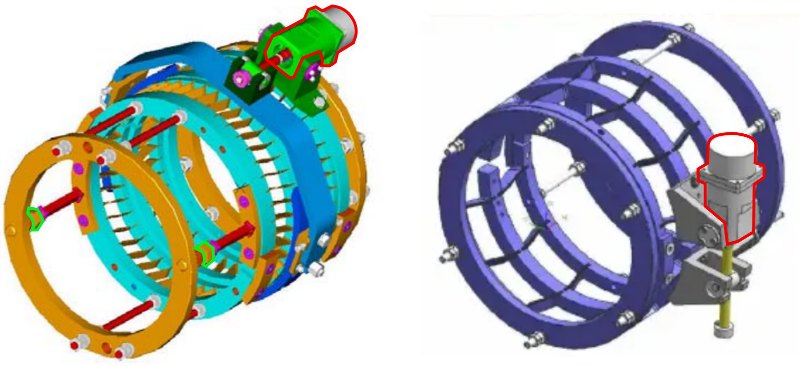

Figure 2.19.: Two different designs for the blade tuner, with their corresponding driving systems. The stepping motor is highlighted in red and the support for fast actuators in green. The tunner in the left was developed in the context of CARE subprograms for the ILC [73] and the design in the right is an enhancement of the TTF superstructures tuner [59].

On the other hand, the Saclay tuner is based on a compound lever mechanism acting at one end of the cavity. The static tuning is obtained with the combination of the lever arm and a screw which is driven by a stepper motor and a gear box. As it is shown in Figure 2.20, one of the links to the He tank is equipped with a piezoelectric holder in which the piezos responsible for the fast tuning are set.

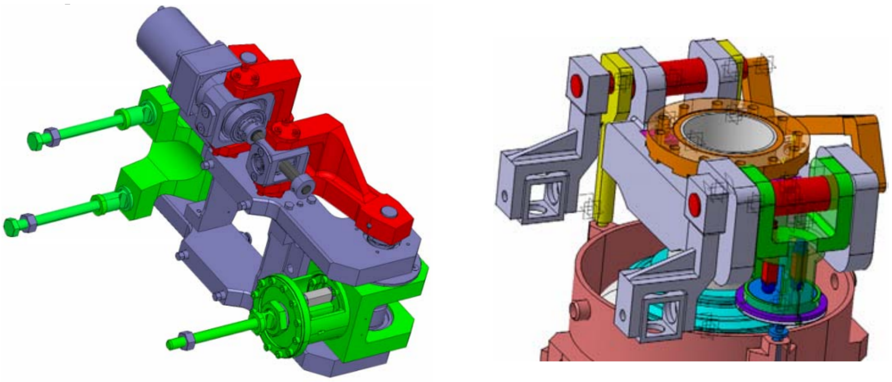

Figure 2.20.: Left picture: The structure of the tuning system itself. Highlighted in red is the system of levers driven by the stepper motor and in green is the system by which the tuner is connected to the helium vessel [23]. Right picture: A similar tuner mounted on a cryostat. The holder for the piezo actuators is shown in green.

Motion made by piezo actuators is transmitted to the cavity flange by the different parts of the tuner. It is important to note that due to the geometry of the system and the fact that part of the stroke is lost in different interfaces of the tuner, less than half of the piezo stroke is transmitted to the cavity flange in this kind of tuner.

The principle of the Saclay tuner system is based on the fact that the pre-load is directly applied on the piezo actuators by the cavity elasticity, which implies that the tuner is designed to lengthen the cavity only [23]. No additional force is applied by the support of the piezo actuators, excepting the weight of the components.

Figure 2.21 shows a tuning system, also based on a double lever mechanism, mounted on a real SRF cavity in HZB [60]. It is worth mentioning that there are many variations in the design of both blade tuners and lever-based tuners, as they are devices that are usually designed ad hoc for each type of cavity to be controlled. Even so, most of them share the same operating principle.

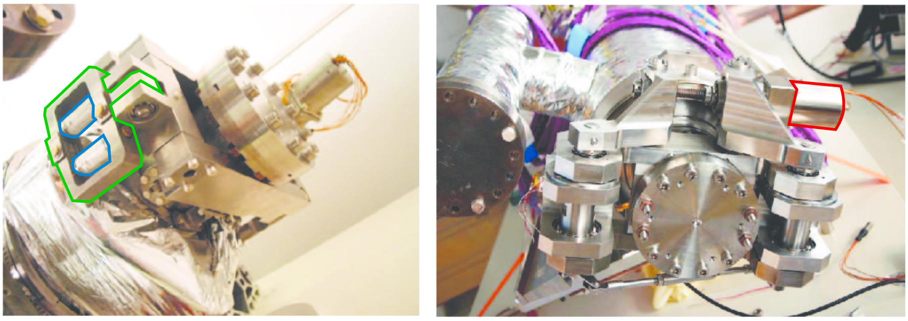

Figure 2.21.: A Lever-based tuning system mounted in the Helium vessel of a real SRF cavity in HZB [60]. In the left picture, the piezo holder is highlighted in green while the actual piezos are highlighted in blue. The stepping motor in shown in the right picture highlighted in red.

## 2.7 | CONTROL TECHNIQUES FOR MECHANICAL DETUNING

As has been demonstrated so far, controlling the level of detuning in SRF cavities is of vital importance for the correct formation of acceleration fields, and consequently for the correct acceleration of particles. This is especially the case for accelerators with high $Q_L$ operation. For that matter, active and passive control strategies are used to mitigate mechanical detuning, commonly in conjunction with each other.

### 2.7.1 | PASSIVE CONTROL

Strategies to mitigate vibration in SRF cavities start from the very stages of design and construction. Passive control techniques aim to attenuate microphonics through mechanical and structural design strategies without requiring active control systems. These methods rely on the inherent properties of the cavity and its support structure to passively mitigate vibrations.

Some common passive control techniques include the mechanical isolation of the cavity. In [38] a passive microphonic mitigation process is performed for the SRF cavities of the LCLS-II project, in which the cavity is isolated from external vibration sources. Due to the combination of low beam loading and a high cavity quality factor, the initially intended peak detuning allowance was set at 10 Hz. However, the peak detuning observed was as high as 150 Hz. This detuning exhibited a complex and variable time structure, characterized by both rapid and gradual fluctuations in both amplitude and spectrum.

Testing conducted under different temperature conditions revealed that thermoacoustic oscillations occurring within the cryogenic valves were the predominant source of the microphonics issue. To address this, measures were taken, including the implementation of valve wipers and adjustments to valve plumbing. These actions led to a significant enhancement in the environment regarding cavity detuning. Furthermore, the mechanical supports of the cavity were redesigned in order to to reduce, as far as possible, the vibrations transferred to the cavity.

The addition of materials with high damping properties in critical areas is another broadly used technique to reduce mechanical detuning by isolating the cavity. The article by T. Powers [75] describes the detuning problem they had at CEBAF due to the traffic of vehicles on the roads adjacent to the center. The solution given to the problem, in this case, was to insulate the structure that connects the cavity with the outside world by means of mechanically attenuating materials such as Sorbothane. For this purpose, attenuator rings were interposed in the joints of the waveguides, cavity supports, etc.

Knowing the origin of the vibration is always a great help in suppressing it. In [78] for example, the problem of microphonics generated by the flow of liquid helium in the cryostat is addressed from a design point of view. for this purpose, three different configurations for the cooling system are proposed that greatly reduce the mechanical disturbances generated by the helium; a dual-bath-single-temperature system, a dual-bath-dual-temperature system and what they called a quiet helium source system.

Much work has also been done to improve the design of the cavities themselves to make them more resistant to vibration. The objective is to reinforce the structure in areas known to be subject to strong mechanical stresses, such the ones generated by Lorentz Forces. This is achieved by stiffening the structure using different techniques such us stiffening rings (see figure 2.22).

On the other hand, in [31], a different fabrication and stiffening method for SRF cavities is presented, based on the addition of a thermal spray copper layer onto a thin wall niobium cavity.

### 2.7.2 | Active control

Active control techniques involve real-time monitoring and correction of microphonics using feedback or feed-forward control systems. These methods aim to actively counteract the vibration-induced disturbances through electromagnetic or mechanical adjustments.

In a feed forward control system, the control action is determined based on the predicted disturbance rather than waiting for the disturbance to affect the

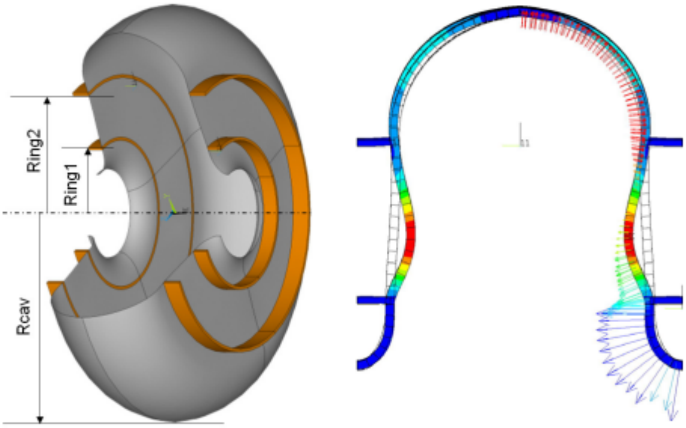

Figure 2.22.: The left side of the figure shows the positioning of the stiffening rings in the cell geometry. On the right, the effect of the stiffening rings on the attenuation of the Lorentz Forces suffered by the cavity is shown [98].

system's output and then adjusting the control accordingly. The idea is to "feed forward" information about the expected disturbance into the control system so that corrective measures can be taken in advance.

In this way, feed-forward systems are commonly used to correct vibrations whose frequency is fixed and localized, either because they are generated by a constant disturbance or because they are located in one of the resonance modes of the cavity. In [68] an Adaptive Feed-forward (AFF) controller is used to control microphonics derived from mechanical eigen modes. Another clear example of feed-forward control is the Narrowband Active Noise Control (NANC) techniques used in [7], where microphonic detuning produced by rotary machinery, such as vacuum pumps or HVAC equipment, is greatly reduced.

In the case of low-frequency stochastic disturbances, like those generated by fluctuations in the liquid helium flow or environmental noise, the use of feedback control systems is necessary. These kind of controllers continuously measure the output of the system, and this information is used to adjust the control inputs in order to minimize the difference between the actual output and the desired set-point. The traditional proportional-integral (PI) controller has been used in various machines [19] and is very effective when the phase response of the tuner is a monotonous function of frequency which is usual at lower frequencies (10 Hz). At higher frequencies, the tuner-cavity system typically has mechanical eigenmodes that introduce steps in the phase response which may possibly lead to positive feedback and instability at even modest gains. This is where the difficulty of controlling this type of system lies. In order to circumvent this problem, arbitrary digital control filters can be optimized specifically to compensate for a given microphonics spectrum while taking into account the exact phase response of the tuner [37]. The main disadvantage of this technique is that it is mandatory to study in detail the dynamics of the system in order to design the controller.

Integrator feedback can also be effectively used to cancel the steady-state error and slow drifts of the detuning, caused for example by the helium pressure variations [79]. This kind of algorithm can also compensates for the effect of the Lorenz Force detuning, when the accelerating field set point is changed, but it is insufficient to compensate perturbations in the frequency range of microphonics.

In [54], a feedback controller based on the input-output linearization method (RST feedback) is employed in a simulation environment to control a 9-cell TESLA cavity. The simulation results were positive, resulting in a very pronounced reduction of the detuning. However, such an algorithm is highly dependent on the accuracy of the mathematical model of the plant used to design it. This can mean a much higher performance in simulation than in real life, since the model used to design the controller is identical to the one that is controlled in the simulation itself.

In the work done by Z. Zheng and colleagues [103], a feedback control combo is used to overcome low frequency detuning in a SRF cavity, in which the Active Disturbance Rejection Control (ADRC) algorithm is tested to control the fast piezo-tuner and a PI for the stepper motor. Despite obtaining very good results in simulation [102], they soon discovered that in practical cases the ADRC provided no better performance than a conventional PI. In this case, they concluded that the delay generated by the hysteresis of the piezo-actuator was the cause of the malfunction of the ADRC.

Certainly, and based on the work done throughout this thesis, the delay in the control signal is especially detrimental to the ADRC algorithm. Thus, this work focuses on creating a modification of the ADRC (MLADRC), much more resistant to delay, with which to control low frequency stochastic detuning. In the following section, the theoretical basis of the ADRC is presented and the changes made to the algorithm to make it delay resistant are explained in depth.

CHAPTER 3

# ACTIVE DISTURBANCE REJECTION CONTROL

The ADRC [36, 33, 87] algorithm is an advanced control technique that addresses the challenges of disturbances and uncertainties in dynamic systems. It provides an effective solution by combining an extended state observer (ESO) with control action to counteract the effects of disturbances and enhance overall system performance.

At its core, ADRC operates on the principle of estimating the total system disturbance, including both internal and external factors, and then generating control signals to compensate for these disturbances [87]. Unlike traditional control methods that rely heavily on precise system models and parameter tuning, ADRC is designed to handle uncertainties without requiring accurate knowledge of the system dynamics.

The ESO in ADRC plays a crucial role. It estimates the so-called "total disturbance", which includes unknown inputs, model uncertainties, and external disturbances. By providing a continuous estimate of the total disturbance, the ESO enables the control system to make real-time adjustments and effectively reject any non desired dynamics. This estimation capability is particularly beneficial in situations where disturbances are unpredictable or difficult to measure accurately.

In this way, ADRC offers several key advantages that contribute to its widespread application in various fields:

I. **Robustness to Uncertainty:** ADRC is renowned for its robustness in the face of uncertainties. The ESO continually updates its estimation based on observed system behavior, allowing the control system to adapt to varying conditions without requiring precise knowledge of the underlying dynamics.

II. **Simplicity and Reduced Modeling:** Unlike some control techniques that demand detailed and accurate system models, ADRC relies on the ESO's disturbance estimation to handle uncertainties. This significantly reduces the complexity associated with model development and system identification.

III. **Fast Disturbance Rejection:** ADRC's ability to estimate and counteract disturbances in real time enables rapid response to changing conditions. This is particularly advantageous in systems where disturbances can occur suddenly or frequently.

IV. **Minimized Tuning Requirements:** Traditional control methods often require intricate tuning to achieve desired performance. ADRC reduces the need for meticulous tuning due to its inherent disturbance rejection capabilities, making it more user-friendly and less sensitive to parameter changes.

V. **Applicability in Complex Systems:** ADRC's effectiveness in dealing with uncertainties makes it suitable for complex systems, including those with nonlinearities, time-varying dynamics, and external disturbances.

VI. **Improved Setpoint Tracking:** ADRC's disturbance estimation and rejection abilities contribute to accurate tracking of setpoints, ensuring that the system's output closely follows the desired reference trajectory.

VII. **Practical Implementation:** The ADRC is a lightweight and very easy to implement algorithm that has found applications in various fields, from industrial processes to robotics, wind energy, and automotive systems, showcasing its versatility and adaptability [100].

In summary, the ADRC algorithm is a powerful approach to control dynamic systems in the presence of disturbances and uncertainties. Its foundation on the extended state observer, along with its robustness, simplicity, reduced tuning requirements, and applicability to complex systems, positions ADRC as a valuable tool for achieving high-performance control in SRF cavities.

The ADRC is a non-linear algorithm in nature, as the ESO originally uses non-linear functions to approximate the total disturbance [40]. This brings with it the design and implementation difficulties typical of non-linear systems. Still, for most practical cases, it is possible to apply a linear version of the ADRC known as linear ADRC or LADRC, which offers virtually the same performance. This LADRC will therefore serve as the starting point for the development of our own algorithm.

The following section presents the theoretical basis of the linear active disturbance rejection control (LADRC).

## 3.1 | THEORETICAL BASIS FOR THE LINEAR ADRC

Prof. Jingqing Han, the creator of the ADRC algorithm, took, in 1989, a different approach in control design, relying bastly on deductive reasoning, as evidenced in his paper "Control theory: is it a model analysis approach or a direct control approach?" [35]. This journey culminated in the development of the ADRC, which was a new way of tackling modern control theory. This paradigm shift in the study and development of a control algorithm resulted in the ADRC not having initially a strict mathematical demonstration from the control theory standpoint, but a more intuitive explanation.

Thus, in this section the operation of the controller will be presented intuitively, and each of its parts will be described both mathematically and functionally.

Before continuing, it is worth mentioning that in the original ADRC scheme, there is an element known as the tracking differenciator (TD). The primary objective of this control element is to follow the transient profile of the reference signal, addressing the issue of sudden changes in the set point and reducing possible noise generated by sensors. As in this particular case, the objective of the controller is to suppress the detuning of the cavities, i.e. to bring the detuning to zero, the setpoint signal will always be constant and null. This is why in this particular case, it does not make sense to implement a TD and that is why no special attention has been devoted to it.

One of the premises for the operation of the ADRC is that virtually any controllable and observable system, whether linear, nonlinear, time-varying, etc., can be simplified to a decoupled chain of integrators by means of the appropriate feedback law. This new system, which in advance will be called generalized canonical form, is always observable and controllable and easily controlled by proportional gains, through a state feedback controller. In equation (3.1) a single-input-single-output (SISO) system of decoupled chain of integrators of order n is shown.

$$\begin{cases} \dot{x}_1 = x_2 \\ \dot{x}_2 = x_3 \\ \vdots \\ \dot{x}_n = u \\ y = x_1 \end{cases} \tag{3.1}$$

Here, $x_1, x_2, \ldots, x_n$ are the states of the system and $y$ and $u$ the output and input respectively. This can also be depicted as its state space representation.

$$\begin{aligned} \dot{\bar{x}}(t) &= \mathbf{A}\bar{x}(t) + \mathbf{B}u(t) \\ y(t) &= \mathbf{C}\bar{x}(t) \end{aligned} \tag{3.2}$$

where **A**, **B** and **C** are described as follows.

$$\mathbf{A} = \begin{pmatrix} 0 & 1 & 0 & \cdots & 0 \\ 0 & 0 & 1 & \cdots & 0 \\ \vdots & \vdots & \vdots & \ddots & \vdots \\ 0 & 0 & 0 & \cdots & 1 \\ 0 & 0 & 0 & \cdots & 0 \end{pmatrix}_{n\times n} \tag{3.3}$$

$$\mathbf{B} = \begin{pmatrix} 0 & \cdots & 0 & 1 \end{pmatrix}^T_{n\times 1} \tag{3.4}$$

$$\mathbf{C} = \begin{pmatrix} 1 & 0 & \cdots & 0 \end{pmatrix}_{1\times n} \tag{3.5}$$

Thus, the main idea of the ADRC algorithm is to find the appropriate feedback law that converts the system to be controlled into its generalized canonical form, to later control it by means of a state feedback. This is achieved by dynamic linearization via the technique of the observer.

Although such concept is, in general, applicable to many nonlinear multi-input–multi-output (MIMO) time varying systems, a nth order SISO system is used as an example for the sake of simplicity and clarity. So lets assume an unknown nth order system described by the following equations.

$$\begin{cases} \dot{x}_1 = x_2 \\ \dot{x}_2 = x_3 \\ \vdots \\ \dot{x}_n = f(x_1, x_2, \ldots, \omega(t), t) + bu \\ y = x_1 \end{cases} \tag{3.6}$$

where $y$ is the output, measured and to be controlled, $u$ is the input, and $f(x_1, x_2, \ldots, \omega(t), t)$ is a multi-variable function of both the states and external disturbances $\omega(t)$, as well as time. This $f$ function encompasses all system dynamics different from the canonical form, as well as the effect of any external perturbation.

The objective here is to make $y$ behave as the desired canonical form using $u$ as the manipulative variable, and for this purpose, $f(x_1, x_2, \ldots, \omega(t), t)$ does not need to be expressively known. In fact, in the context of feedback control, $F(t) = f(x_1, x_2, \ldots, \omega(t), t)$ is something to be overcome by the control signal, and it is therefore denoted as the "total disturbance". Thus, the algorithm takes as disturbance, not only external perturbations, but also unwanted internal dynamics of the system. At this point, a challenge typically associated with system identification has been transitioned into the realm of disturbance rejection.

Treating $F(t)$ as an additional state of the system $x_{n+1}$, it is possible to redefine (3.6) with the following extended state system.

$$\begin{cases} \dot{x}_1 = x_2 \\ \dot{x}_2 = x_3 \\ \vdots \\ \dot{x}_n = x_{n+1} + bu \\ \dot{x}_{n+1} = \dot{F}(t) \\ y = x_1 \end{cases} \tag{3.7}$$

Which can also be expressed by its state space representation as follows.

$$\begin{aligned} \dot{\bar{x}}(t) &= \mathbf{A}_e \bar{x}(t) + \mathbf{B}_e u(t) + \mathbf{E}_e \dot{F}(t) \\ y(t) &= \mathbf{C}_e \bar{x}(t) \end{aligned} \tag{3.8}$$

Being $\mathbf{A}_e, \mathbf{B}_e, \mathbf{C}_e$ and $\mathbf{E}_e$ the matrices shown bellow.

$$\mathbf{A}_e = \begin{pmatrix} 0 & 1 & 0 & \cdots & 0 \\ 0 & 0 & 1 & \cdots & 0 \\ \vdots & \vdots & \vdots & \ddots & \vdots \\ 0 & 0 & 0 & \cdots & 1 \\ 0 & 0 & 0 & \cdots & 0 \end{pmatrix}_{(n+1)\times(n+1)} \tag{3.9}$$

$$\mathbf{B}_e = \begin{pmatrix} 0 & \cdots & 0 & b & 0 \end{pmatrix}^T_{(n+1)\times 1} \tag{3.10}$$

$$\mathbf{C}_e = \begin{pmatrix} 1 & 0 & \cdots & 0 \end{pmatrix}_{1\times(n+1)} \tag{3.11}$$

$$\mathbf{E}_e = \begin{pmatrix} 0 & 0 & \cdots & 1 \end{pmatrix}^T_{(n+1)\times 1} \tag{3.12}$$

Note that at this point, our system has been redefined as a decoupled chain of integrators in the first n states, plus the total disturbance which is isolated in the n+1 state.

So, the next step is to apply a Luenberger observer [15] to the system (see equation (3.13)), which will be called extended state observer (ESO) since it is applied to the extended system.

$$\begin{aligned} \dot{\hat{\bar{x}}}(t) &= \mathbf{A}_e \hat{\bar{x}}(t) + \mathbf{B}_e u(t) + \mathbf{L}_0 (y(t) - \hat{y}(t)) \\ \hat{y}(t) &= \mathbf{C}_e \hat{\bar{x}}(t) \end{aligned} \tag{3.13}$$

Where $\mathbf{L}_0 = [\beta_1 \ldots \beta_{n+1}]'$ is a parameter that defines the bandwidth of the observer ($\omega_e$), which have to be usually at least ten times faster than that of the system's dynamic and delimits the frequency range of the disturbances to be considered.

A State Observer, is a mathematical tool used in control theory to estimate the internal state variables of a dynamic system based on its measurable outputs, as long as the system is observable. In this way, by feeding into the observer the input signal $u$ of the system and the measured output signal $y$ it is capable of estimating the values of every state at every moment ($\hat{\bar{x}}$) as well as the output of the system $\hat{y}$. Taking into account that the system has been defined in such way that the total disturbance $f(x_1, x_2, \ldots, \omega(t), t)$ is isolated in the last state of the extended system, the ESO is able to estimate its value. This allows the control law $(u_0 - F(t))/b$ to reduce the plant to a cascade integral form, where $u_0$ refers to the control signal generated by the state feedback controller. Figure

3.1 shows the topology of the LADRC algorithm and figure 3.2 the structure of the ESO in more depth.

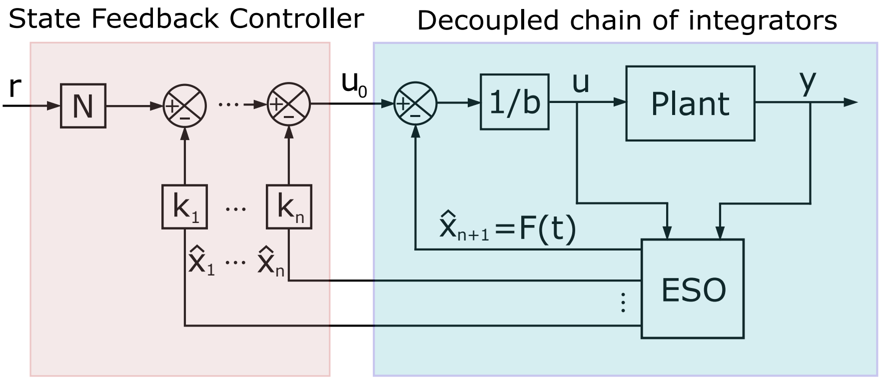

Figure 3.1.: Common topology of the LADRC algorithm.

It is important to note that, unlike a conventional state observer, in which an approximate mathematical model of the plant is needed, the ESO does not need any information about the system to be controlled, since its purpose is to force it to behave as a decoupled chain of integrators, by feeding back the total disturbance. In fact, in this explanation the order of the ESO has been defined as the order of the system to be controlled plus one, but this has been done only to understand the origin and concept of the ESO. In reality, the stability of the control system can be assured as long as the ESO is an order higher than the relative order of the system [91], which is the difference between the number of poles and zeros of the system.

In the schematic shown in figure 3.1, a state feedback control is applied to the linearized plant where N is a scaling parameter and $\bar{K} = [k_1, k_2 \ldots, k_n]$ is the vector resulting from solving the corresponding pole placement problem [66]. In this particular case, the control signal $u$ is defined by the following expression.

$$u(t) = \frac{Nr - \bar{K}[\hat{x}_1, \hat{x}_2, \ldots, \hat{x}_n]^T - \hat{x}_{n+1}}{b} \tag{3.14}$$

where $\hat{x}_{n+1}$ corresponds to the total disturbance $F(t)$.

Note that, once the plant has been reduced to its decoupled chain of integrators form, it is possible to apply a wide range of different controllers.

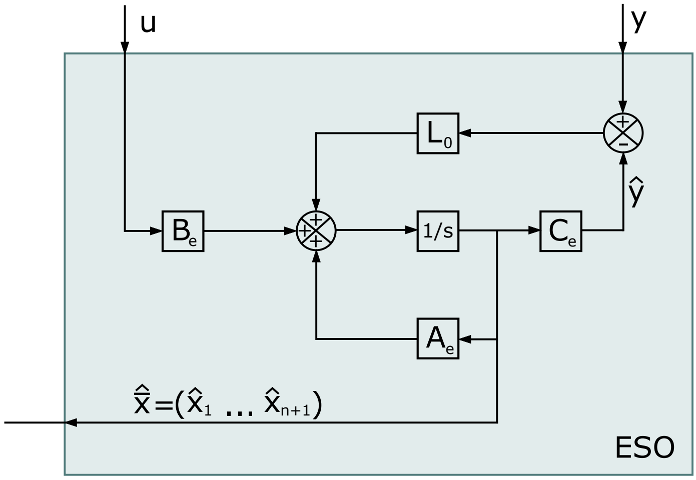

Figure 3.2.: Topology of the ESO.

## 3.1.1 | ALTERNATIVE SYSTEM DESCRIPTION

To facilitate the analysis of the system by means of its open-loop frequency response, and based on [99], the LADRC scheme has been redefined as shown in Figure 3.3.

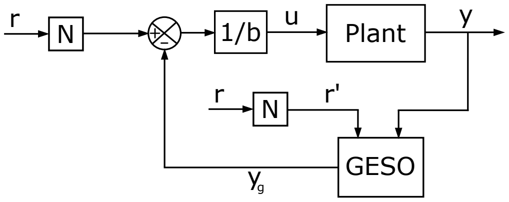

Figure 3.3.: Topology of the alternative scheme for the LADRC using a generalized extended state observer (GESO).

The main idea of this alternative form of LADRC is to internalize the controller directly into the ESO dynamics, thus generating the so-called generalized ESO (GESO). This GESO has the same function as the ESO, but instead of reducing the system to a decoupled chain of integrators, it reduces the system directly to the desired dynamics, which would have been determined by the controller ($\bar{K}$ vector) in the standard scheme.

The GESO can be expressed by its state-space representation as follows.

$$\begin{cases} \dot{\hat{\hat{z}}}(t) = \mathbf{A}_g \hat{\hat{z}}(t) + \mathbf{B}_g \begin{pmatrix} r'(t) \\ y(t) \end{pmatrix} \\ y_g(t) = \mathbf{K}_g \hat{\hat{z}}(t) \end{cases} \tag{3.15}$$

Being $\mathbf{A}_g$, $\mathbf{B}_g$ and $\mathbf{K}_g$ defined by the following equations.

$$\mathbf{K}_g = \begin{pmatrix} \bar{K} & 1 \end{pmatrix} \tag{3.16}$$

$$\mathbf{A}_g = \mathbf{A}_e - \mathbf{L}_0 \mathbf{C}_e - \frac{1}{b} \mathbf{B}_e \mathbf{K}_g \tag{3.17}$$

$$\mathbf{B}_g = \begin{pmatrix} \frac{1}{b}\mathbf{B}_e & \mathbf{L}_0 \end{pmatrix} \tag{3.18}$$

Note that, although conceptually there are differences between the two schemes, they are mathematically equivalent. Figure 3.4 depicts the topology of the GESO based on the original ESO scheme.

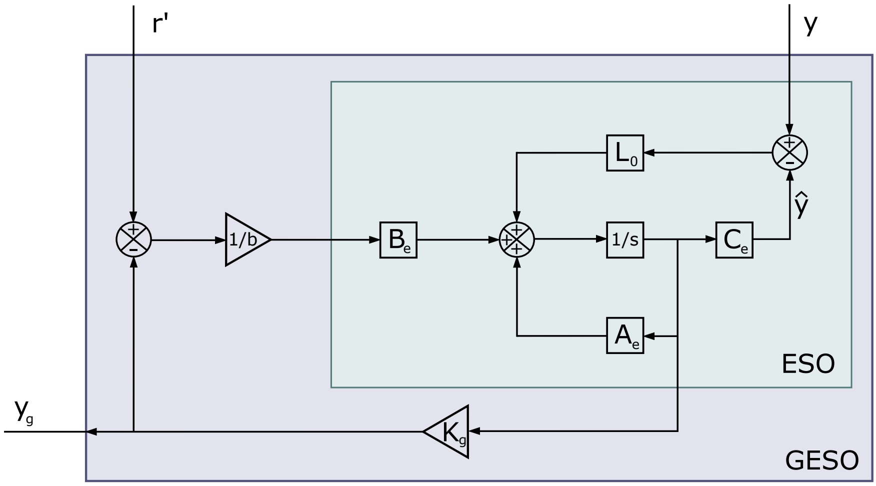

Figure 3.4.: Topology of the GESO based on the scheme of the standard ESO.

Using the Laplace transform presented in [30] over equation (3.15) the GESO can be rewritten as a function of the variable s as shown below.

$$\begin{cases} s\hat{\hat{Z}}(s) = \mathbf{A}_g \hat{\hat{Z}}(s) + \frac{\mathbf{B}_e}{b} R'(s) + \mathbf{L}_0 Y(s) \\ Y_g(s) = \mathbf{K}_g \hat{\hat{Z}}(s) \end{cases} \tag{3.19}$$

Solving the equation (3.19) to suppress $\hat{\hat{Z}}(s)$, the output of the GESO $Y_g(s)$ can be defined by the equation (3.20).

$$
\begin{aligned}
&Y_g(s) = \mathbf{K}_g(s\mathbf{I}_{(n+1)\times(n+1)} - \mathbf{A}_g)^{-1}\frac{\mathbf{B}_e}{b}R'(s) \\
&+ \mathbf{K}_g(s\mathbf{I}_{(n+1)\times(n+1)} - \mathbf{A}_g)^{-1}\mathbf{L}_0 Y(s)
\end{aligned}
\tag{3.20}
$$

which can be rewritten as a two-degree-of-freedom (2DOF) conventional feedback structure as shown in Figure 3.5. It must be said that this equivalent description is only valid for analysis and not as an alternative implementation scheme since numerical issues may arise.

$$
\begin{aligned}
&Y_g(s) = H_{geso}(s)Y(s) + H^r_{geso}(s)R'(s) \\
&H_{geso}(s) = \mathbf{K}_g(s\mathbf{I}_{(n+1)\times(n+1)} - \mathbf{A}_g)^{-1}\mathbf{L}_0 \\
&H^r_{geso}(s) = \mathbf{K}_g(s\mathbf{I}_{(n+1)\times(n+1)} - \mathbf{A}_g)^{-1}\frac{\mathbf{B}_e}{b}
\end{aligned}
\tag{3.21}
$$

where $H_{geso}(s)$ is a transfer function relating the $Y(s)$ input to the GESO output $Y_g(s)$, while $H^r_{geso}(s)$ relates the input to the GESO $R'(s)$ also to the output $Y_g(s)$. Also note that the denominator of both transfer functions are the same.

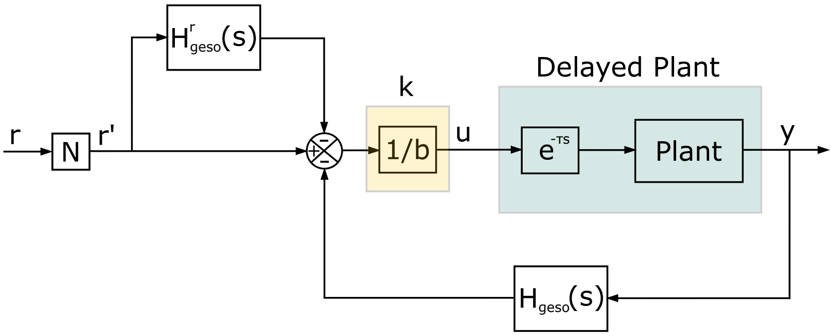

Figure 3.5.: Topology of the alternative scheme for the LADRC using a GESO, defined by a 2DOF feedback structure. A possible time delay $\tau$ is also added to the plant.

This description facilitates the stability analysis of the LADRC system. Using the transfer functions in (3.20) and adding a time delay $\tau$ to the plant, the closed loop characteristic equation derived from Figure 3.5 can be written as follows:

$$
1 + e^{-\tau s}kH_{geso}(s)P(s) = 0 \tag{3.22}
$$

where $P(s)$ is the transfer function of the plant. The roots of (3.22) are the poles of the closed loop transfer function and defines the stability of the system which can be studied as function of the direct-loop gain k, for a particular time delay $\tau$. Note that $k = 1/b$ is the nominal value that satisfies the matching condition, since this description is valid for any time delay, including $\tau = 0$. The matching condition is a term that refers to the minimal condition that assures the estimated disturbance and the actual disturbance to match, so the controller is able to effectively rejects disturbances by introducing an integral effect to the controller.

Note that the introduction of the time delay in the transfer function is of vital importance, since the main handicap of the application of the ADRC control in an SRF cavity is its special sensitivity to delay. Thus, one of the requirements for developing a more delay-resistant control algorithm is to be able to study the effect of the delay on the controlled system.

When $\tau$ is not 0, the analytical solution of equation (3.22) is not simple, since the number of roots are infinite. However, frequency domain methods, such as the Nyquist criterion, are valid in this case [104, 99]. By obtaining the Nyquist diagram (or Bode diagram for open loop stable systems) from the expression $e^{-\tau s} k H_{geso}(s) P(s)$, the stability of the system can be analysed by the Nyquist criterion and the delay stability margin can be easily obtained.

As a straightforward result, if the original system is open-loop stable, for any delay $\tau$ a sufficiently low $k$ makes the closed-loop system stable [19]. However, if this $k$ value is lower than $1/b$ the matching condition is not fulfilled, and the disturbance reduction is diminished.

Let us now consider the following expression:

$$H_{geso} = H^{c}_{geso} + H^{f}_{geso} \tag{3.23}$$

being

$$H^{c}_{geso} = [K, 0](sI_{(n+1)\times(n+1)} - A_g)^{-1} L_0 \tag{3.24}$$

$$H^{f}_{geso} = [0 \ldots 0, 1](sI_{(n+1)\times(n+1)} - A_g)^{-1} L_0 \tag{3.25}$$

By decomposing the $H_{geso}$ transfer function as shown in equation (3.23), the feedback loop in Figure 3.5 can be separated into two loops, which can be analysed independently. One of them refers to the equation (3.25) and represents the effect that the total disturbance feedback has on the overall control loop. The other loop referring to equation (3.24) represents the effect of the feedback of the rest of the state vector. Note that the denominator of the transfer function $H^c_{geso}$ and $H^f_{geso}$ are equal and have a pole in the origin, since the matching condition is satisfied by definition of matrix $A_g$.

To illustrate the effect of each loop, an example with two mechanical resonances is considered:

$$P(s) = \frac{1.4}{s+1} + g_0 + g_1 \tag{3.26}$$

$$g_0 = \frac{\omega_0^2}{s^2 + 2\delta_0\omega_0 s + \omega_0^2} \tag{3.27}$$

$$g_1 = \frac{\omega_1^2}{s^2 + 2\delta_1\omega_1 s + \omega_1^2} \tag{3.28}$$

with $\omega_0$=10 rad/s, $\delta_0$=0.1, $\omega_1$=40 rad/s, $\delta_1$=0.05 and a constant delay $\tau$ of 0.005 s. Those values were chosen in order to define a system with low relative stability, which is a fundamental characteristic of the real system to control.

The objective of the following study is to analyze the influence of each of the parts of the control loop described by 3.25 and 3.24, which, as already mentioned, refer to the feedback of the total disturbance and the feedback of the rest of the state control, respectively. For this purpose, the $\tau$ delay of 0.005 s is added and the open loop of the aforementioned parts of the control loop, i.e. functions $e^{-\tau s}H^c_{geso}(s)P(s)$ and $e^{-\tau s}H^f_{geso}(s)P(s)$, is studied.

In this way, several first order LADRC controllers have been defined based on equation (3.15), using different values of the observer bandwidth $\omega_e$ (two poles in -$\omega_e$) to obtain $\mathbf{L}_0$, and different values of the controller bandwidth $\omega_c$ (one pole in -$\omega_c$) to compute $\mathbf{K}$.

First, to observe the effect of the observer bandwidth $\omega_e$ on the controller performance, the controller bandwidth $\omega_c$ is set constant to 5 rad/s and several GESOs are generated with observer bandwidths ranging between 1000 and 10000 rad/s. Figure 3.6 shows the Bode diagram for both open-loop transfer functions $e^{-\tau s}H^c_{geso}(s)P(s)$ and $e^{-\tau s}H^f_{geso}(s)P(s)$ for the aforementioned values of $\omega_e$.

Similarly, several LADRC controllers (again first order) has been defined keeping constant $\omega_o$=1000 rad/s for different values of the LADRC control bandwidth $\omega_c$. Figure 3.7 shows the Bode diagrams for the open-loop transfer functions $e^{-\tau s}H^c_{geso}(s)P(s)$ and $e^{-\tau s}H^f_{geso}(s)P(s)$, for such systems.

Observing Figures 3.6 and 3.7, it is easy to discern that the observer band-

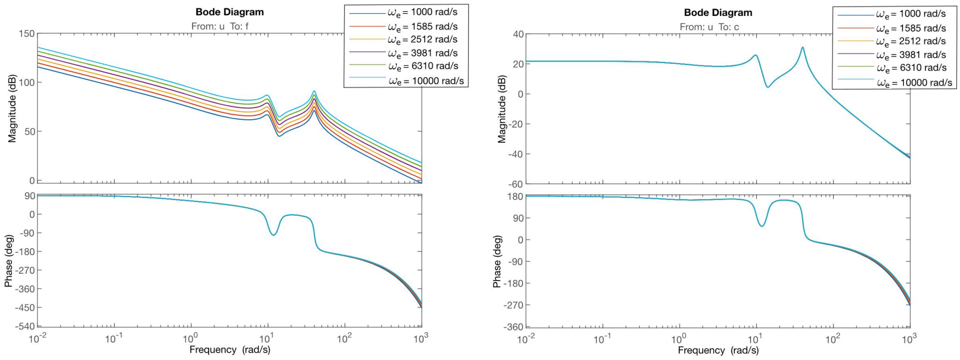

Figure 3.6.: Open loop Bode diagrams with $\omega_c$=5 rad/s and $\tau = 0.005$ s for equations $e^{-\tau s}H^c_{geso}(s)P(s)$ (right) and $e^{-\tau s}H^f_{geso}(s)P(s)$ (left). The observer bandwidth $\omega_0$ ranges between 1000 rad/s and 10000 rad/s and the phase degrades linearly with $\tau$.

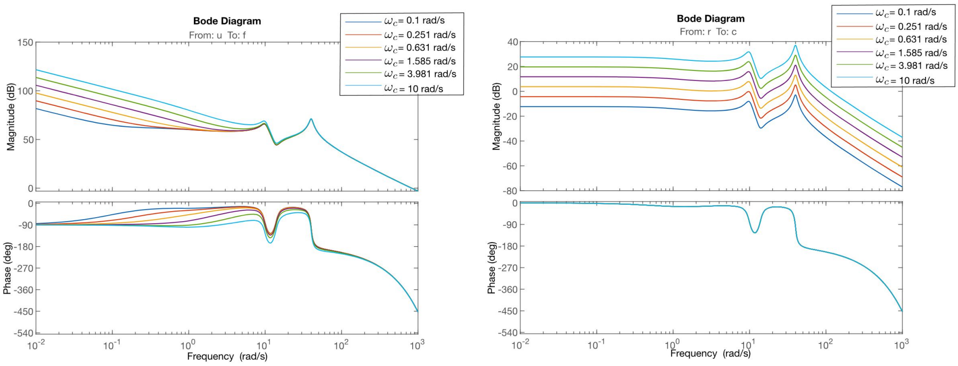

Figure 3.7.: Open loop Bode diagrams with $\omega_e$=1000 rad/s and $\tau = 0.005$ s for equations $e^{-\tau s}H^c_{geso}(s)P(s)$ (right) and $e^{-\tau s}H^f_{geso}(s)P(s)$ (left). The controller bandwidth $\omega_c$ ranges between 0.1 rad/s and 10 rad/s and the phase degrades linearly with $\tau$.

width is closely related to the change of the gain value in the disturbance estimation loop ($H^f_{geso}(s)P(s)$).

Other relevant conclusion, observed in all cases, is the evident effect of the delay $\tau$=0.005 s on the stability of the LADRC system. This effect is especially important for the feedback loop containing the estimated disturbance. The high gain responsible of the disturbance reduction makes the system unstable with relatively low time delay, since the delay increases the phase lag proportionally with the frequency. In this case, following the Nyquist criterion for stable open-loop systems, the system becomes unstable if the system amplitude is higher than 0 db at frequencies with a phase lag higher than -180 degrees. Figure 3.6 and 3.7 show that the mentioned phase limit is always surpased due to the delay effect and, in conclusion, all cases have a maximum system gain that guarantees the stability. This maximum allowable gain limits the capacity of disturbance rejection.

Lastly, this example shows that, comparing both feedback loops, the disturbance estimation loop ($H^{f}_{geso}(s)P(s)$) is the dominant one, since its open-loop gain is much larger. This means that it can be considered the main control effect of the LADRC scheme. From this analysis, it is clear that the expression (3.22) facilitates the stability analysis of the LADRC controller, especially in the presence of time delay, and shows the possibility of using the gain $K$ as a designing parameter.

## 3.2 | ADRC ALGORITHM AND TIME DELAY

Like other control techniques, ADRC has practical limitations. One significant restraint arises from the presence of time delay, which reduces the stability range of the closed loop system.

Although the nominal stability of the ADRC was proved by adopting a sufficiently fast observer with a performance recovery principle [28], it is difficult to be employed in practice because the intrinsic delay of the system destabilizes the control loop.

In [62], the study of this phenomenon is carried out in depth, and it is concluded that the input time-delay tolerance is strictly decreasing with the increasing of the bandwidth of the ESO when other control parameters are fixed.

In contrast, the observer's accuracy is strongly linked to its dynamics, with better performance obtained the faster the observer is. Therefore, with the original ADRC, it is necessary to find a compromise between performance and closed-loop stable robustness.

Such is the sensitivity of the algorithm to delay that it is unfeasible for systems with relatively large time delays or poor relative stability, as it is shown in next section.

### 3.2.1 | EMPIRICAL ANALISYS

Said conclusions can be demonstrated empirically with relative ease in simulation by applying an ADRC to a plant, and varying the parameters of interest, such as time delay ($\tau$) and ESO bandwidth ($\omega_e$), to see the resulting system response.

For this purpose, in this section a mathematical model, obtained by Dr. Neumann and colleagues in [68] ,will used, which consist of a mechanical system composed by a saclay-I type piezo tuner and a 9-cell TESLA cavity. This is an approximate model of order 28 and relative order 1, whose frequency response is depicted in the Bode diagram of Figure 3.8.

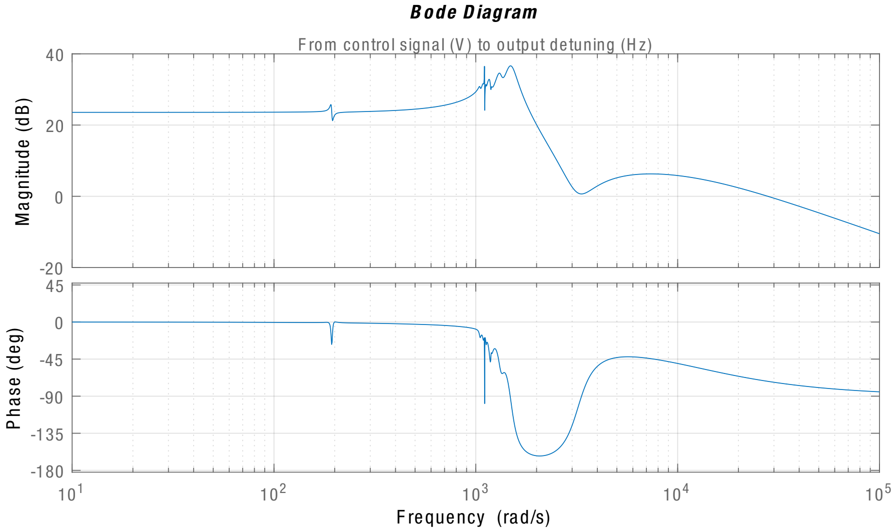

Figure 3.8.: Frequency response of the approximated mathematical model of the mechanical system formed by a Saclay-I piezo tuner and a 9 cell TESLA cavity. The model has no time delay. The diagram relates the control signal to the piezo actuator in volts with the generated detuning in Hz.

First, the effect of the ESO bandwidth ($\omega_e$) on the system stability and controller performance is studied. For this purpose, since the relative order of the system is two, an ADRC of order two is applied. This controller is composed of an ESO of order three and a state feedback control. The controller bandwidth ($\omega_c$) is set to 150 rad/s, which means that the control vector $\bar{K}$ is defined in such way that all poles of the resulting system are located at that frequency. The resulting system has fast dynamics with a rise time of approximately 20 milliseconds. Figure 3.9 shows the step response comparison between the non controlled piezo-cavity system and the controlled system depending on $\omega_e$.

As shown in figure 3.9 the temporal response of the system to a step input is faster and more stable the bigger $\omega_e$ is. This is because the wider the bandwidth of the observer, the wider the frequency range in which it can detect and correct unwanted disturbances and internal dynamics. In fact, if $\omega_e$ is expanded sufficiently, it is possible to reduce the complex dynamics of the mechanical system that is being controlled to a simple second-order system with a double pole at -150 rad/s. Figure 3.10 shows a Bode diagram comparing the original uncontrolled mechanical system to the one achieved with an extremely high ESO bandwidth ($\omega_e = 1000000 rad/s$).

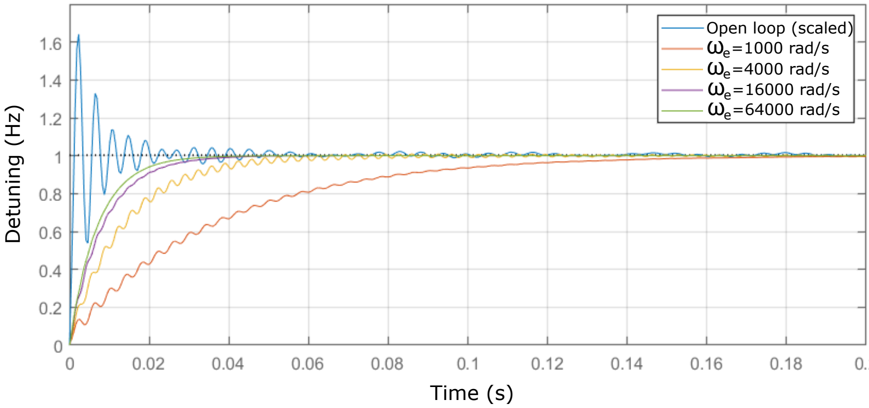

Figure 3.9.: Step response of the piezo-cavity mechanical system in open loop and controlled by different ADRCs. The uncontrolled system's output is scaled by a factor of 1/15 for ease of comparison. The controller bandwidth $\omega_c$ equals 150 rad/s for all cases while the ESO bandwidth $\omega_e$ varies.

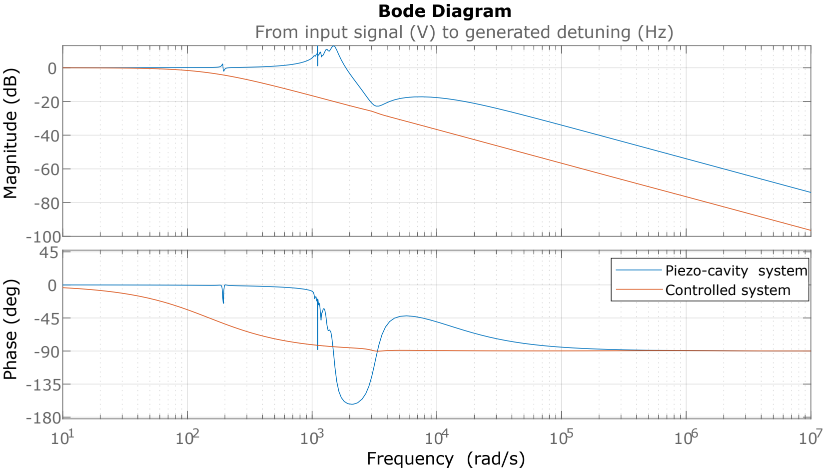

Figure 3.10.: Frequency response of the piezo-cavity mechanical system in open loop and controlled by an ADRC with $\omega_e = 1000000$ rad/s and $\omega_c = 150$ rad/s. The uncontrolled system's output is scaled by a factor of 1/15 for ease of comparison.

Thus, based on the simulations performed, it is empirically demonstrated that the performance of the ADRC increases as the bandwidth of the ESO increases.

Let now analyze the effect of the time delay on the stability of the controlled system. For this purpose, an ADRC configuration that is relatively conservative in terms of ESO bandwidth, but offers good dynamics is selected, i.e. $\omega_c = 150$ rad/s and $\omega_e = 16000$ rad/s.

As shown in Figure 3.11, as soon as delay is introduced into the system, the performance of the controller starts to deteriorate exponentially. The longer the delay, the lower the relative stability of the system, as reflected in the oscillations in figure 3.11, until it is completely destabilized when reaching a delay value between 100 to 110 microseconds. Note that these delay values are very small even for an actuator with such fast dynamics as a piezo-actuator, which, as will be shown later, has a delay of the order of milliseconds.

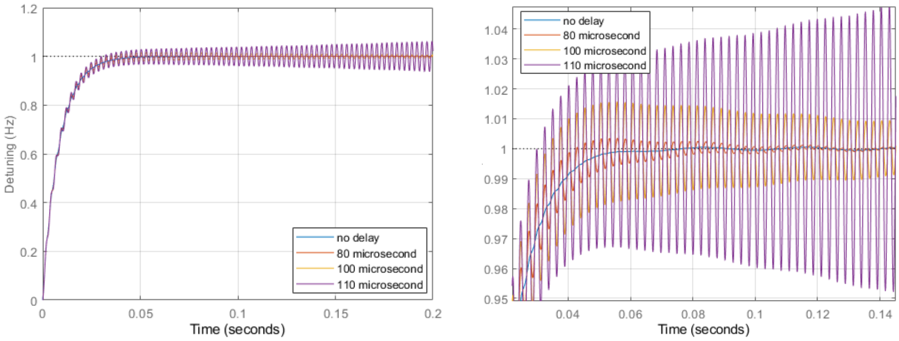

Figure 3.11.: Both images show the step response of the controlled system with varying time delays. The ADRC that controls the system has $\omega_e = 16000$ rad/s and $\omega_c = 150$ rad/s as fixed parameters. The image on the right is a detailed view of the image on the left, where the trend of the system is better appreciated.

By analyzing the bode diagram of the system in open loop (see chapter 3.1.1 and equation (3.22)), for different time delays (figure 3.12), it is easy to discern where and why the instability occurs. As it is well known, the time delay degrades the phase response of the system proportionally to the frequency, which is reflected in the bode diagram as an exponential drop in phase, since it is represented in logarithmic scale. At the same time, looking at the frequency response of the system (figure 3.8), it can be seen how at around 2000 rad/s the phase of the system is approximately -150 degrees. This means that this particular system has very little margin of stability against delay, since if the phase worsens by more than 30 degrees in that frequency zone, a phase crossover is generated in which the gain of the open-loop system is greater than 0 dB, so that the Nyquist stability criterion is not met.

According to [62], the ADRC time delay tolerance increases as the observer bandwidth decreases. To demonstrate this fact and to analyze the stabilization process from the point of view of the Nyquist stability criterion, the delay is set to 150 microseconds and the observer bandwidth is decreased until the system is stabilized. As it is shown in figure 3.13, as the bandwidth of the observer decreases, the gain of the control system decreases too. In this way, it is possible to achieve a $\omega_e$ low enough so that the open-loop gain of the system at the

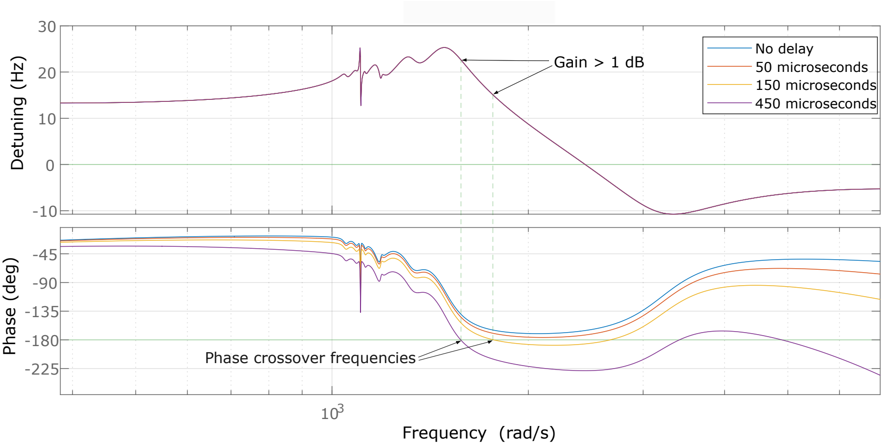

Figure 3.12.: Frequency response of the open loop system with varying time delays. The ADRC that is applied has $\omega_e = 16000$ rad/s and $\omega_c = 150$ rad/s as fixed parameters. An arrow indicates the phase crossover frequency at which the Bode stability criterion is not met for each delay case.

phase crossover frequency is less than 1dB, thus fulfilling the Nyquist stability criterion. In this particular case, the observer's bandwidth had to be decreased to 1000 rad/s in order to stabilize the system.

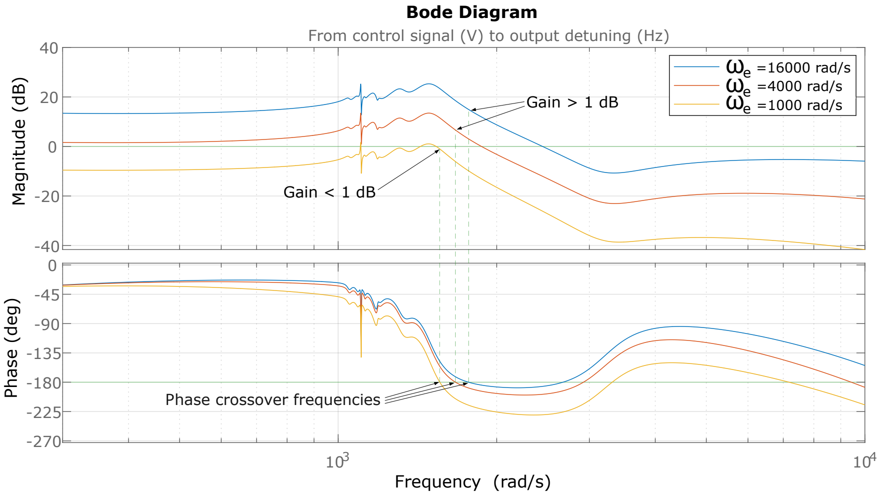

Figure 3.13.: Frequency response of the open loop system with a fixed time delay of 150 $\mu s$ and varying $\omega_e$. The bandwidth of the controller $\omega_c$ is 150 rad/s. An arrow indicates the phase crossover frequency at which the Bode stability criterion is met and not met for each $\omega_e$ case.

Obviously, with the reduction of the bandwidth of the observer, comes the loss of performance of the controller. Figure 3.14 shows the step response of the controlled system (closed loop) without delay ($\omega_e = 16000$ rad/s and $\omega_c = 150$ rad/s) and with a delay of 150 $\mu s$ ($\omega_e = 1000$ rad/s and $\omega_c = 150$ rad/s). A noticeable degradation in system dynamics is observed, which also suggests a loss in the controller's disturbance rejection capabilities.

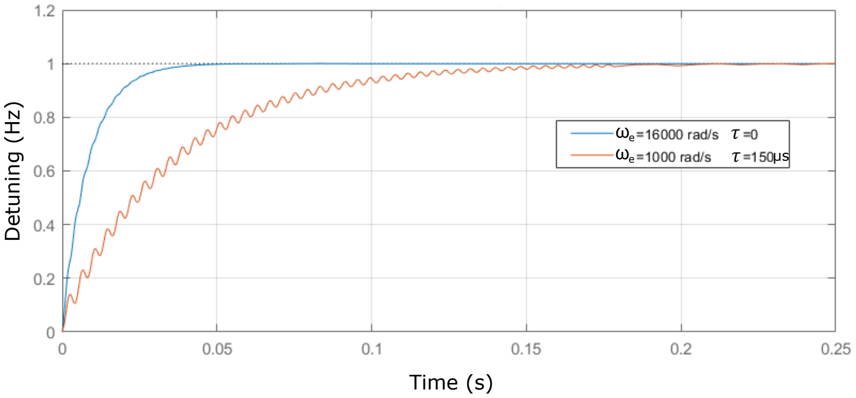

Figure 3.14.: Step response of the controlled system with and without delay. The ADRC that controls the non delayed system has parameters of $\omega_e = 16000$ rad/s and $\omega_c = 150$ rad/s. The ADRC that controls the delayed system has parameters of $\omega_e = 1000$ rad/s and $\omega_c = 150$ rad/s.

In conclusion, it is shown that the bandwidth of the observer is closely related to the performance of the system but also to its sensitivity to delay. Furthermore, it is clear that reducing the ESO bandwidth is not a valid system for the stabilization of systems such as the one in question, since the loss of perturbation rejection capabilities is too significant.

### 3.2.2 | CONTROL STRATEGIES AGAINST TIME DELAY

Thus, in recent decades, control specialists from all over the world have been working on strategies to overcome this shortcoming and make the ADRC more resistant to delay.

Various methods have been proposed to address this issue within ADRC-based schemes. In [36], Han proposed the possibility of designing the ADRC without considering time delay, which sacrifices performance. Another approach involves using a Padé approximation, increasing the system order, but it is only suitable for small time delays [90, 29]. To take into account the time delay, it has been suggested in [99, 101] to introduce a delay in the control signal before it enters the ESO. In [77], a Smith predictor-based generalized Proportional Integral control is proposed for input delayed nonlinear mechanical systems. [14] proposes a predictor scheme for time delay compensation in uncertain time delay systems. [29] presents a two-degree-of-freedom (2DOF) control structure for unstable time-delayed systems. More recently, ADRC designs based on probabilistic robustness have been applied to systems with delay [97].

While these methods improve stability in the presence of time delay, they may reduce the disturbance rejection effect and often require more information about the system, negating one of the major advantages of the ADRC.

## CHAPTER 4

# MODIFIED LINEAR ACTIVE DISTURBANCE REJECTION CONTROL

As already discussed in the previous chapter, the ADRC is a versatile and easy to implement controller, which provides certain features ideal for reducing detuning in SRF cavities, such as fast disturbance rejection, great performance controlling non-linear systems and not needing much information about the system to be controlled for its design and implementation.

The main idea of the algorithm is to reduce the plant to a simpler decoupled chain of intergrators form (canonical form) in order to, then, control it by means of a state feedback controller. This is achieved through the feedback of what is known as the total disturbance, which is nothing more than any dynamics, whether internal or external, that are different from the dynamics of the canonical form of the system. To obtain this total disturbance, the algorithm uses an extended state observer whose operation is described in chapter 3.1.

As shown in section 3.2, the ADRC algorithm is particularly sensitive to time delays in the control signal and the system destabilizes even for low delay and controller gain values. In addition, many of the techniques used so far to circumvent this problem sacrifice performance and perturbation rejection capability in exchange for stability. Many others sacrifice one of the major advantages of the ADRC, which is the lack of need to know the dynamics of the system to be controlled.

In this section, a novel solution is presented to make the ADRC more resistant to delay without compromising in excess its performance and its intrinsic advantages such as the possibility to design the controller without having information about the system to be controlled. In this case, the linear version of the ADRC, the LADRC, is taken as the foundation of the new algorithm. This modification of the LADRC is called modified linear active disturbance rejection control, or MLADRC.

Throughout this chapter, the formal definition of the MLADRC algorithm will be presented, as well as the detailed explanation of its working principles and the main differences with respect to the original LADRC. Then, the algorithm design methodology is shown, with a step-by-step guide, both for the case in which the system dynamics are known and for the case in which they are not. Later, a simulation example is used to illustrate the design methodology and to perform a stability analysis of the algorithm in question. Finally, the algorithm is implemented in a real oscillatory system to validate its feasibility.

## 4.1 | THEORETICAL BASIS FOR THE MLADRC

The concept of the MLADRC arises from the reformulation of the LADRC algorithm (see chapter 3.1.1) that was carried out to analyze the stability by means of the analysis of the open-loop system response.

The central idea in this stabilization approach involves systematically pushing the controller towards its stability threshold by progressively increasing the control loop's gain. Once this limit is reached, an assessment of the resulting instability is carried out. This evaluation can be based on analyzing the system's open-loop Bode diagram if the system dynamics are known or by studying the system's output signal when the system's dynamics are unknown. Subsequently, with the frequency range responsible for system destabilization identified, the goal is to re-establish stability using loop shaping techniques that will be explained in more detail throughout this chapter. Figure 4.1 shows the topology of the MLADRC.

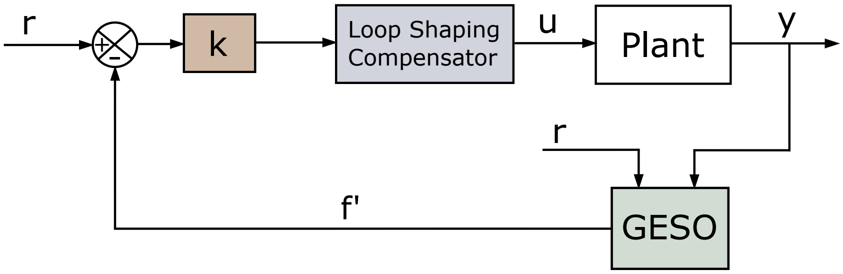

Figure 4.1.: Topology of the MLADRC controller.

The following is a mathematical definition of the MLADRC controller, as well as an explanation of its operation. It also details the most notable differences between the MLADRC and the original ADRC.

### 4.1.1 | USE OF THE GENERALIZED EXTENDED STATE OBSERVER

One of the major differences between MLADRC and the original ADRC is the internalization of the state space feedback control in the ESO itself, giving rise to the so-called generalized ESO, or GESO.

As explained in chapter 3.1.1, one of the main purposes of reformulating the ADRC scheme is to access the frequency response of the open-loop system. This is not possible with the original scheme since the ESO has as an input the control signal $u$ (see figure 3.1). By means of this transformation of the scheme, an algorithm mathematically identical to the original one is obtained. However, this reformulation offers the possibility of studying the stability of the closed loop system by means of frequency domain techniques, i.e, by analyzing the characteristic equation shown in equation (3.22).

The GESO is formally defined by means of its state space representation by the following equation.

$$\begin{cases} \dot{\hat{\bar{z}}}(t) = \mathbf{A}_g \hat{\bar{z}}(t) + \mathbf{B}_g \begin{pmatrix} r(t) \\ y(t) \end{pmatrix} \\ y_g(t) = \mathbf{C}_g \hat{\bar{z}}(t) \end{cases} \tag{4.1}$$

Being $\mathbf{A}_g = \mathbf{A}_e - \mathbf{L}_0 \mathbf{C}_e - \frac{1}{b} \mathbf{B}_e \mathbf{K}_g$ and $\mathbf{B}_g = \left( \frac{1}{b} \mathbf{B}_e \quad \mathbf{L}_0 \right)$, as it was defined in chapter 3.1.1. In the other hand, $\mathbf{C}_g$ is defined differently depending on the signal that is desired to be used in order to control the system (see equations 4.4 and 4.5). Note that these matrices can be represented more explicitly as follows

$$\mathbf{A}_g = \begin{pmatrix} -\beta_1 & 1 & 0 & \cdots & 0 & 0 \\ -\beta_2 & 0 & 1 & \cdots & 0 & 0 \\ \vdots & \vdots & \vdots & \ddots & \vdots & \vdots \\ -\beta_{n-1} & 0 & 0 & \cdots & 1 & 0 \\ -\beta_n - k_1 & -k_2 & -k_3 & \cdots & -k_n & 0 \\ -\beta_{n+1} & 0 & 0 & \cdots & 0 & 0 \end{pmatrix}_{(n+1)\times(n+1)} \tag{4.2}$$

$$\mathbf{B}_g = \begin{pmatrix} 0 & \beta_1 \\ \vdots & \vdots \\ 1 & \beta_n \\ 0 & \beta_{n+1} \end{pmatrix}_{(n+1)\times 1} \tag{4.3}$$

$$\mathbf{C}_{g1} = \begin{pmatrix} k_1 & k_2 & \cdots & k_n & 1 \end{pmatrix}_{1\times(n+1)} \tag{4.4}$$

$$\mathbf{C}_{g2} = \begin{pmatrix} 0 & 0 & \cdots & 1 \end{pmatrix}_{1\times(n+1)} \tag{4.5}$$

where $n$ is the relative order of the system, which is the difference between the number of poles and zeros. Note that $(\beta_1, \ldots, \beta_{n+1})$ and $(k_1, \ldots, k_n)$ are the vectors $\mathbf{L}_0$ and $\mathbf{K}$ respectively, which are designer tools to define the bandwidth of the observer $\omega_e$ and the controller $\omega_c$.

It is also worth mentioning that this scheme allows the use of two possible alternatives to generate the output; $\mathbf{C}_{g1}$ and $\mathbf{C}_{g2}$. In the first case, the full feedback loop is used, similarly to the typical LADRC scheme. While in the second case, the feedback is obtained only by means of estimating the total disturbance F(t).

Taking into account the nature of the total disturbance and the results obtained in previous experiments [52], the dynamics resulting from this updated approach do not diverge significantly from those of the original scheme. The notable benefit lies in the simplified structure of the controller, which facilitates more straightforward analysis.

One of the most important aspects about this new scheme is that due to the way the $A_g$ matrix is defined (see equations (3.17) and (4.2)), the matching condition in the GESO is fulfilled for any closed loop gain. This allows us to exchange the 1/b gain of the original ADRC scheme (see figure 3.1) for a variable gain $k$, which allows us to adjust the gain of the controller. This gain can be explicitly implemented in the direct chain of the controller or be implicit in the definition of the loop shaping compensator.

Varying this gain has an effect very similar to that shown in figure 3.13 in which the bandwidth of the observer $\omega_e$ is changed. The benefit of having this control variable is that it eliminates the need for redefining the ESO when adjusting the open-loop gain, assuring the matching condition. This enables us to systematically approach the stability limit of our controller by incrementally raising this gain, facilitating an in-depth examination of the underlying factors leading to system instability.

Finally, by looking at both the matrices defining the GESO (equations (4.2), (4.3), (4.4) and (4.5)) and the MLADRC topology (figure 4.1), it can be seen that the high frequency gain $b$ is not a relevant part of the algorithm description, so it is not a parameter to be known, unlike in the case of the original ADRC. This means that to design the MLADRC, it is only necessary to know the relative order $n$ of the system, which is another great advantage over the original algorithm.

### 4.1.2 | LOOP SHAPING COMPENSATOR

As the analisys shown in chapter 3.2.1 illustrates, gain reduction is a limited design strategy, which may be useful only for systems with small time-delays. However, the MLADRC approach paves the way for enhancing stability through the implementation of a loop shaping compensator, thereby enabling an increase in loop gain and consequent reduction of disturbances. This represents one of the primary innovations introduced by the MLADRC algorithm.

A loop shaping compensator refers to a control system component used to alter the frequency response or transfer function of a control loop. This can involve adding filters, poles, or zeros in the control system to shape the open loop frequency response and achieve the desired closed-loop behavior. Loop shaping is a widely used design methodology that can be implemented through various strategies to achieve a desired frequency response shape, as detailed in [3]. Controllers used in this approach may include PID controllers, lead or lag phase compensators, notch filters and so forth.

In the case of time delayed systems, loop shaping can be applied to compensate the frequency response in the high gain, high phase lag areas. Two potential measures can be implemented: either reducing the gain or introducing a lead phase within the critical frequency range. In scenarios involving resonances, lead compensators can enhance phase response, while notch filters can greatly reduce the system's gain within these sensitive frequency ranges. Conversely, at high frequencies, a gain-reducing filter may become essential, as the lag introduced by the delay may be excessive to be able to compensate.

Taking into account all that was exposed in chapter 3.1.1 and adding the loop shaping compensator into the equation, it is possible to analyze the open-loop response of the system by studying the characteristic equation (4.6).

$$1 + e^{-\tau s} k H_{geso}(s) C(s) P(s) = 0 \tag{4.6}$$

Being $H_{geso}$ the transfer function of the GESO, depicted in equation (3.21), $P(s)$ the transfer function of the plant and $C(s)$ the transfer function of the loop shaping compensator. Likewise, $\tau$ and $k$ refer to the time delay and loop gain respectively.

Note that the frequency response can be obtained experimentally in a large number of systems.

## 4.2 | DESIGNING METHODOLOGY

When developing this algorithm, the need for a straightforward process for the controller design, regardless of the system to be controlled, was taken into account. One of the major advantages of the MLADRC is that it is not necessary to know the dynamics of the plant, although it is useful when designing the loop shaping compensator. This poses a great usefulness for big facilities, as the operator could set the controller parameters without knowing the specific behaviour of a given cavity.

### 4.2.1 | PRACTICAL STEPS FOR THE DESIGN OF THE MLADRC

The method for designing and adjusting the controller is as follows.

I. Select the bandwidth of the observer, $\omega_e$. This parameter determines the frequency range in which the controller detects disturbances and is closely related to the stability of the system. As shown in [52], the stability decreases the larger the bandwidth of the observer. This is because at higher frequencies, the effect of the delay in the phase of the system is greater. Thus, the observer bandwidth is set as large as the delay allows. For systems with little relative stability, a conservative approach is to choose the bandwidth a decade larger than the highest frequency disturbance to be rejected.

II. Set the bandwidth of the controller, $\omega_c$. This step determines the final dynamics of the system and therefore varies depending on the application. In any case it should be at least 10 times smaller than the bandwidth of the observer.

III. Once implemented, it is advisable to start with almost no gain G, and gradually increase it until the desired dynamics are fulfilled. If the relative stability of the system is small, either because of the delay or because of its own characteristics, it may destabilize before the desired dynamics are achieved. In that case, a loop shaping compensator will be needed.

IV. If the plant transfer function is known, the filter can be designed using

> model based techniques in the frequency domain. If there is no information about the plant, it is possible to gradually increase the gain (G) until the system approaches instability and measure the frequency in which the instability occurs. Then, implement a loop shaping compensator such us a notch filter in order to drastically decrease the action of the controller in that problematic frequency, without affecting the performance in the rest of the bandwidth.

This method is illustrated below by means of a practical example carried out in simulation, but first, a brief review of how to analyze system stability using a bode diagram.

### 4.2.2 | SYSTEM STABILITY ANALYSIS USING BODE PLOT

The Nyquist Stability Criterion is a mathematical method employed to assess the stability of a control system and can be easily studied through the examination of its Bode plot, as long as the system is a minimum-phase system. Because it only looks at the Bode plot of the open loop systems, it can be applied without explicitly computing the poles and zeros of either the closed-loop or open-loop system. As a result, it can be applied to systems defined by non-rational functions, such as systems with delays. This criterion offers a quantitative assessment of the system's stability, considering both the system's gain and phase characteristics in its response.

This method introduces two critical measures of stability, namely the gain margin and phase margin. These margins are important because they provide an indication of how close the system is to instability and are very useful tools for designing the MLADRC controller for minimum-phase systems. They are defined as follows.

#### | GAIN MARGIN

The gain margin is the amount of additional gain that can be added to the system without causing instability. It is defined by the negative of the gain of the open loop system at the phase crossover frequency, that is the frequency in which the phase of the open loop system crosses -180 degrees. The gain margin can be directly read from the Bode plot by calculating the vertical distance between the magnitude curve and the x-axis at the phase crossover frequency, as it is shown in figure 4.2. The greater the gain margin, the greater the relative stability of the system.

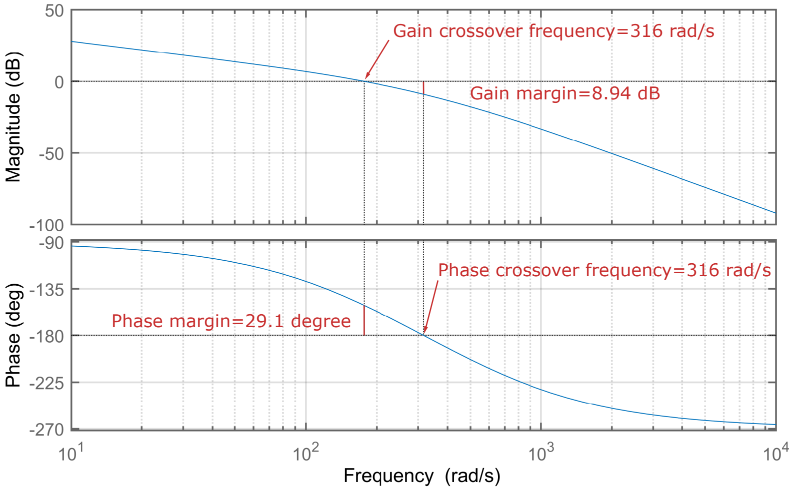

Figure 4.2.: Phase and gain margin of an example system.

### | PHASE MARGIN

The phase margin refers to the amount of phase, that can be increased or decreased without making the system unstable. It is defined by the phase lag of the open loop system minus 180 degrees, at the frequency where the gain of the open loop system is 0 dB. This frequency is called the gain crossover frequency. The phase margin can be directly read from the Bode diagram by calculating the vertical distance between the phase curve and and -180 degrees at the gain crossover frequency, as it is shown in figure 4.2. The greater the phase margin, the greater the relative stability of the system.

## 4.2.3 | PRACTICAL EXAMPLE OF THE DESIGN AND STABILIZATION OF A MLADRC ALGORITHM

For this example, the piezo tuner model shown in figure 3.8 is used as the target system, but in this case, with an instrinsic delay of 150 $\mu s$. As it has been pointed before, this delay generates a linear decay in the phase of the system that is shown as exponential in the bode diagram (see figure 4.3), since the frequency is represented in logarithmic scale.

As it can be seen, the combination of the delay and the observed resonance peak at 1500 rad/s causes the system to destabilize in closed loop at a relatively low frequency, 2000 rad/s or 318 Hz. This will be of particular importance for the stabilization process that will follow.

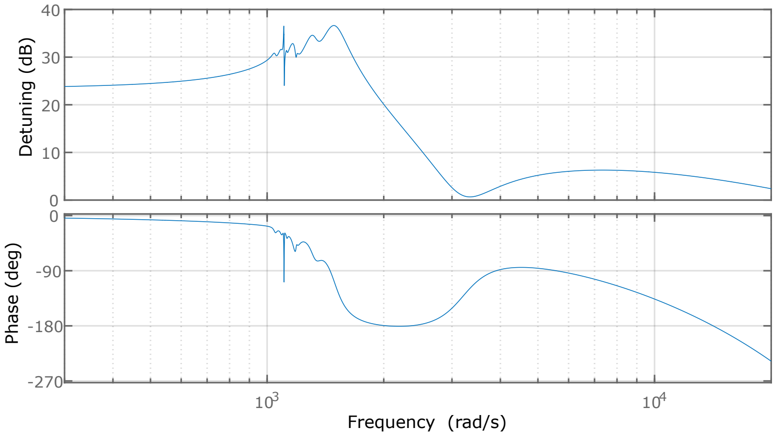

Figure 4.3.: Bode diagram of the delayed piezo tuner that is used as an example in chapter 4.2.3.

In order to carry out the design and stabilization process, the control system shown in figure 4.4 is implemented in Matlab, where the input r refers to the system set-point and p to the external disturbances suffered by the system.

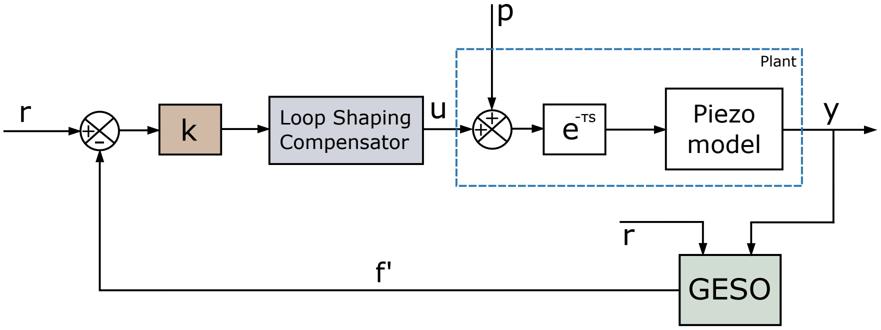

Figure 4.4.: Scheme of the simulation system implemented in matlab to test the designing methodology of the MLADRC.

To begin with, and based on the fact that the relative order of the system to be controlled is 1, it is determined that it is sufficient to implement an MLADRC of order 1, with the corresponding ESO of order 2. Thus, the next step is to set the bandwidths of both the observer $\omega_e$ and the controller $\omega_c$.

Typically, the bandwidths of both the controller and the observer are defined according to the system to be controlled and the specifications of the particular system, following the guidelines set out in the section 4.2.1. In this case, it is decided to work with $\omega_c = 150$ rad/s and $\omega_e = 16000$ rad/s since they were the ones used in the stability analysis carried out in section 3.2.1, and this will allow us to compare the results of our stabilization system with those obtained in that section.

One of the main objectives of our stabilization system is not to degrade the performance of the controller to the best extent possible, unlike most of the processes proposed to date. This is why, first of all, the GESO is applied to the non delayed target system in order to study its ideal performance. As shown in figure 4.5, the controller in question provides first-order dynamics, with no overshoot and a rise time of 0.02 sec. As far as disturbance damping is concerned, the controller is capable of suppressing the perturbation in roughly 0.02 seconds, suggesting a bandwidth of approximately 90 Hz.

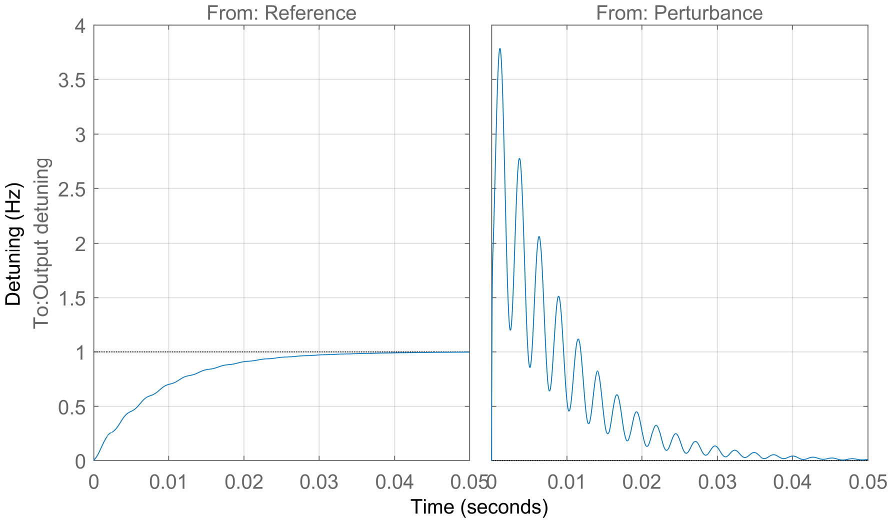

Figure 4.5.: Step response of the non-delayed system controlled by a MLADRC with $\omega_e = 16000$ rad/s and $\omega_c = 150$ rad/s. The plot in the left shows the response of the system when introducing the step as the systems setpoint, while the plot in the right shows the response of the system when introducing the step as a perturbation.

Once the delay inherent to the piezo-tuner has been applied, the system becomes unstable. This fact is easy to explain by analyzing the bode diagram of the system response in open loop. Figure 4.6 shows the comparison between the open loop response of the delayed and the non-delayed systems. As can be seen, the delayed system shows the typical linear degradation in the phase derived from the time delay, which in the bode diagram appears as an exponential decay. Due to the resonance peak that the system has at 1500 rad/s, the phase of the system around that frequency is very close to -180 degrees. When the delay is applied, the phase shift it introduces at those frequencies is enough to make the phase exceed -180 degrees and thus generate a phase crossover frequency. As the gain of the open loop system at that crossover frequency is higher than 0dB, this means that the closed loop system is unstable, as it is well demonstrated if a step input is introduced in it.

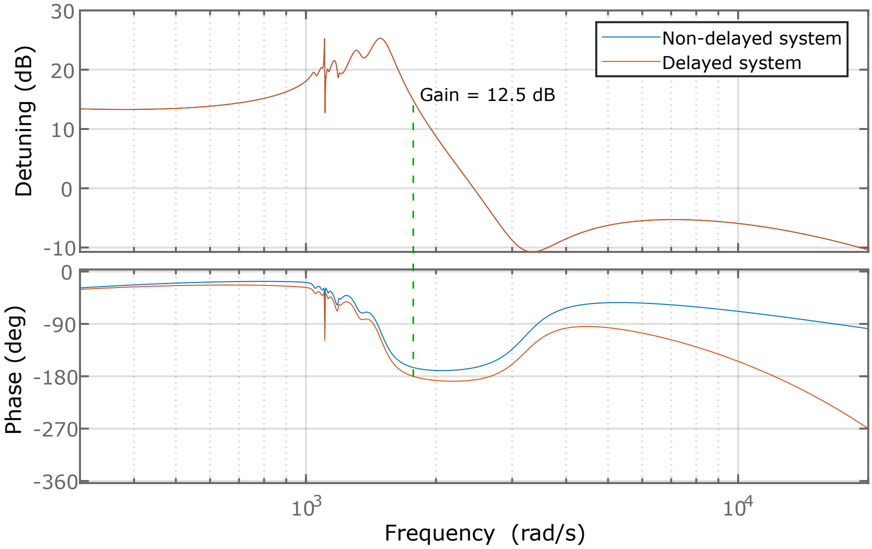

Figure 4.6.: Bode diagram of the controlled system in open loop. The blue plot represents the response of the non delayed system while the orange plot represents the delayed system.

Since the system is unstable,there are two options at this point. Use frequency design techniques in case the dynamics of the system are known (approximate transfer function), or apply a notch filter at the destabilization frequency if there is no transfer function available. In order to demonstrate the validity of both procedures and to compare the results, both stabilization approaches will be carried out below.

## STABILIZATION VIA A NOTCH FILTER

First of all, it is worth mentioning that, taking into account the characteristics of this system, stabilization by means of a notch filter is not the most efficient solution. This is because the mechanism by which the system is stabilized by introducing a notch filter is based on the decrease of the open loop gain of the system at the destabilization frequency. Figure 4.6 shows how the gain of this system at that frequency is 12.5 dB, which implies that for the notch filter to stabilize the system, it must reduce the gain below 0 dB in that frequency range without affecting the phase excessively. This implies a relatively large change in the dynamics of the system, and suggests that the system is stabilized at the expense of a degradation in performance. Still, implementing a notch filter as a loop shaping compensator is a viable method for when no system information is available, as shown below. Equation (4.7) depicts the transfer function of a generic notch filter, where $\omega_0$ is the frequency to which the filter is centered and $Q$ the quality factor of the filter.

$$H_{Notch}(s) = \frac{s^2 + \omega_0^2}{s^2 + \frac{\omega_0}{Q}s + \omega_0^2} \tag{4.7}$$

In the hypothetical case of not having an approximate transfer function, the first step to implement the notch filter is to obtain the frequency at which the system destabilizes. For this purpose, the gain $k$ is reduced until the point at which the system stabilizes, and gradually increased until the oscillations typical of the onset of destabilization are detected at the system output. For this particular case, the system starts to destabilize with a gain $k = 0.18$ as it is shown in figure 4.7.

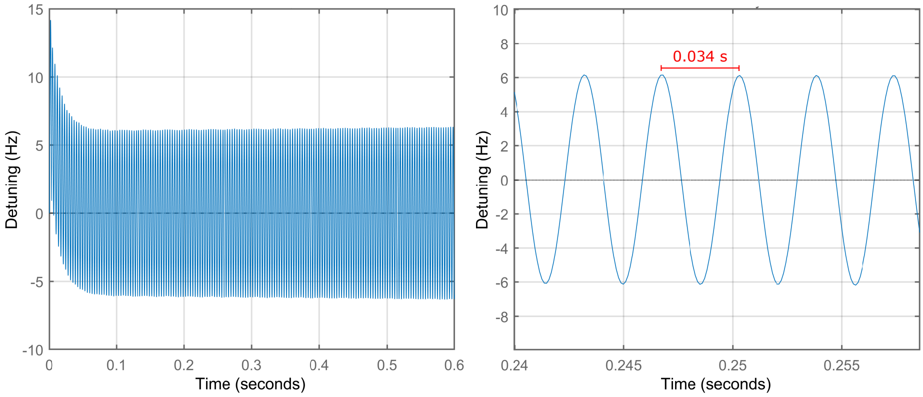

Figure 4.7.: Time response of the delayed system when k=0.18 and a step input is introduced as a perturbation. The plot in the left shows the evolution of the system's time response while the right plot shows a zoom of that same response.

When the system destabilizes, it begins to oscillate with a period of 34 $\mu s$, which indicates a destabilization frequency of approximately 295 Hz, or 1850 rad/s. It is important to note that since there is no transfer function available, this method relies more in trial and error. In this way, a notch filter centered in 1850 rad/s and with a quality factor Q=1 was initially implemented as the loop shaping compensator. Then, those parameters were tuned until an appropriate system response was achieved. The final implemented notch filter is described by equation (4.8) and is centered in 1550 rad/s with a quality factor Q=0.88.

$$H_{Notch}(s) = \frac{s^2 + 2402500}{s^2 + 17613s + 2402500} \tag{4.8}$$

Figure 4.8 shows the time response of the controlled system to a step input and compares it to the ideal behaviour obtained above. As expected, stabilisation by means of the notch filter has altered the performance of the original controller and has, to some extent, degraded its ability to reduce disturbances. Even so, the loss in performance has not been as noticeable as that obtained by other stabilisation methods such as reducing the gain of the control loop. In fact, the controller maintains intact the ability to follow a set-point, just as the original controller would do when controlling the system without delay. In addition, the settling time of the disturbance is approximately 0.05 seconds, suggesting a bandwidth of 36 Hz.

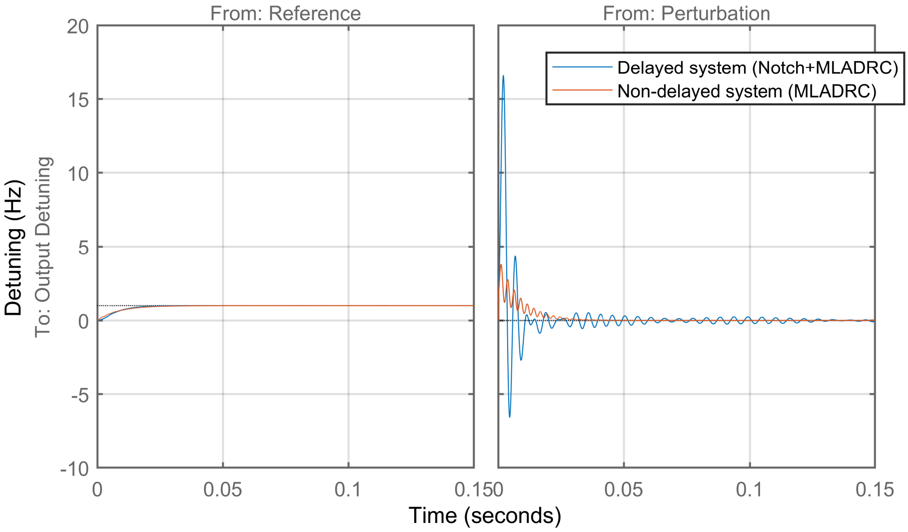

Figure 4.8.: Step response of both the non-delayed system controlled by a MLADRC and the delayed system controlled by the same MLADRC but stabilized with a notch filter. The plot in the left shows the response of the systems when introducing the step as the systems set-point, while the plot in the right shows the response of the systems when introducing the step as a perturbation.

By looking at the Bode diagram relating the disturbances to the output of the closed-loop system (see figure 4.9), it is easy to discern the effect of the notch filter on the disturbance suppression capability of the controller. As the notch filter reduces the gain of the controller at frequencies around 1550 rad/s to prevent it from destabilising, it also reduces its ability to act on the disturbances at these frequencies. This is reflected in the closed-loop system's Bode diagram as an increase in the gain at around 1550 rad/s.

It is important to note that this does not mean that the notch filter is an inferior solution per se. There are simply cases where one type of loop shaping compensator gives better results than others, and this depends largely on the characteristics of the system to be controlled. What is true is that when the

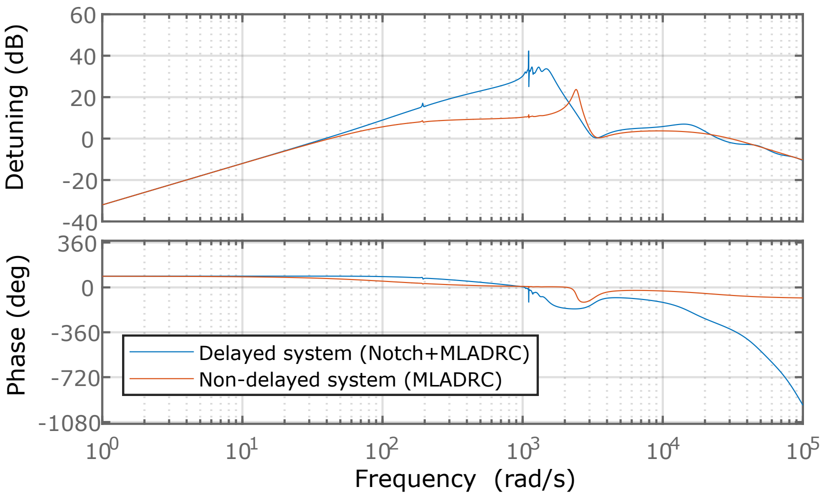

Figure 4.9.: Bode diagram relating the disturbances entering the system with the generated detuning. It compares the response of the non-delayed system while being controlled with the MLADRC and Bode diagram of the delayed system being controlled by the MLADRC and stabilized by the notch filter.

frequency response of the system is not known, it is usually easier to implement a notch filter, since it is enough to know the frequency at which the system destabilises. That being said, it is also possible to implement a lead filter by trial and error.

## STABILIZATION VIA LOOP SHAPING TECHNIQUES

In order to stabilise a system using loop shaping techniques, it is imperative to have an approximate transfer function of the system. This stabilisation method is based on analysing the frequency response of the system in open loop and detecting the frequency range in which the Nyquist stability criterion is not met. Later, by means of additional filters and controllers implemented as loop shaping compensators, the idea is to model the gain and phase of the system at those problematic frequencies in order to bring the system back to its stability regime, affecting its dynamics as little as possible.

Returning to the problem at hand and looking at the figure 4.6, it can be seen that the instability is given by the phase of the system in the frequency range 1800-2800 rad/s. The combination of the delay and the resonance that the system exhibits at 1500 rad/s causes the phase of the open-loop system to exceed -180 degrees in a short frequency range and in conclusion makes the closed-loop system unstable.

Thus, the objective of the loop shaping compensator that should be implemented is to increase the phase of the system in that problematic frequency range so that it never exceeds -180 degrees and thus no phase crossover frequency exists where the gain is greater than 0 dB. The ideal filter to achieve such an effect is a lead compensator, which can be defined by the equation (4.9).

$$H_{Lead}(s) = \frac{\omega_p(s+\omega_z)}{\omega_z(s+\omega_p)} \tag{4.9}$$

where $\omega_z$ stands for the frequency at which the zero of the filter is located and $\omega_p$ represents the frequency at which the pole is located.

Thus, to stabilise the system, the lead compensator has been designed in such a way that its pole is at 2500 rad/s and its zero is at 1500 rad/s. In this way, the open-loop system's phase is increased in the desired frequency range without affecting the gain significantly. This is important because if the gain is increased excessively, stability problems could arise at other frequencies that have not been problematic up to now.

In conclusion, the lead filter implemented as a loop shaping compensator is defined by the equation (4.10) and has a Bode diagram as shown in the figure 4.10.

$$H_{Lead}(s) = \frac{1.667s + 2500}{s + 2500} \tag{4.10}$$

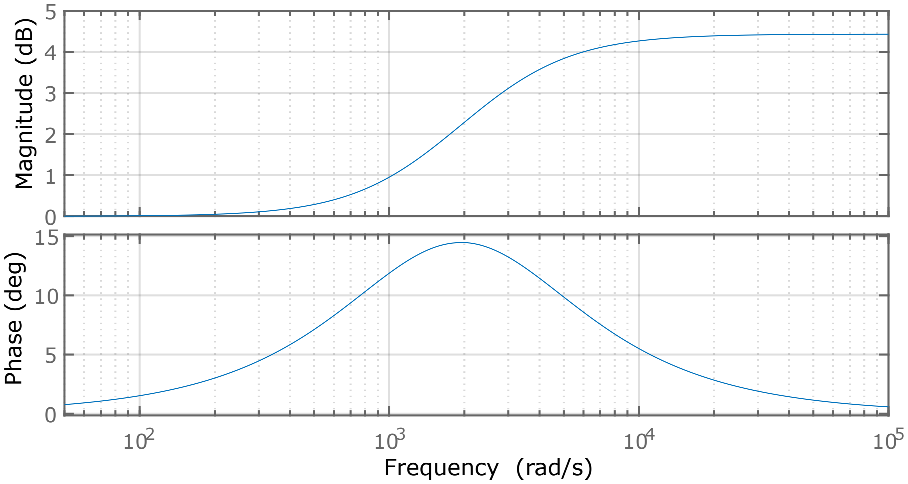

Figure 4.10.: Bode diagram of the phase lead filter used to stabilize the system.

As can be seen in figure 4.10, the lead filter increases the phase of the system by approximately 15 degrees at around 2000 rad/s. If this filter is implement and the Bode diagram of the complete system in open loop plotted (figure 4.11), it can be seen how the phase crossover frequency that was at 1850 rad/s has disappeared, resulting in the stabilisation of the system.

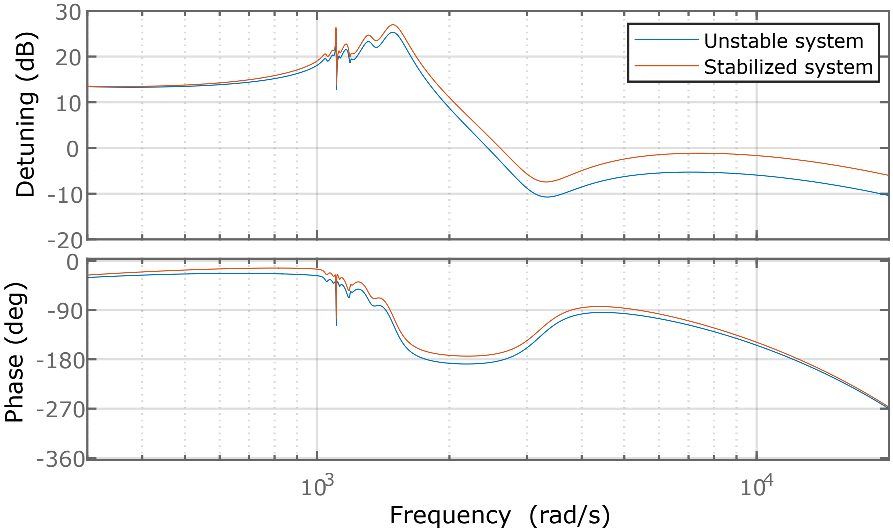

Figure 4.11.: Bode diagram of the open loop of the system without stabilization and stabilized by a lead compensator.

As the lead compensator stabilises the system, almost without altering the dynamics of the system, the controller performance obtained by this technique is superior to that achieved by the notch filter, and almost identical to the ideal performance of the MLADRC when controlling the system without delay. This has more to do with the fact that more information was available for the design of the lead compensator than with the compensator itself. Figure 4.12 compares the time response of the system without delay being controlled by the MLADRC (ideal performance) and the system with delay, stabilised by the lead compensator and controlled by the same MLADRC. As can be seen, the lead compensator not only stabilises the system, but also slightly improves performance by increasing the gain of the controller at frequencies above 2000 rad/s.

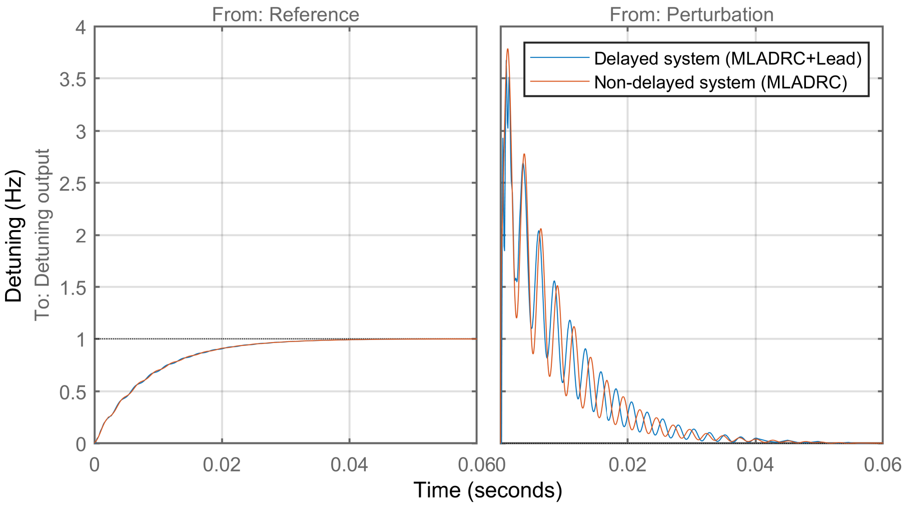

Figure 4.12.: Step response of both the non-delayed system controlled by a MLADRC and the delayed system controlled by the same MLADRC but stabilized with a lead filter. The plot in the left shows the response of the systems when introducing the step as the system's set-point, while the plot in the right shows the response of the systems when introducing the step as a perturbation.

## 4.3 | Experimental validation of the MLADRC

In this section, the aforementioned approach is implemented in a real mechanical system with relevant resonant modes to analyse the feasibility of the design process and the performance of the resulting controller.

### 4.3.1 | System description

The mechanical system used to analyse the stabilization process must meet certain characteristics that are important for proper testing of the control algorithm and its ability to reject disturbances. Considering that the ultimate goal of this algorithm is to control the microphonics of an SRF cavity, it is important that the mechanical system in which the controller is validated has similar qualities to those of such cavities, at least from a control point of view.

Among the most remarkable features regarding the control of an SRF cavity are its high sensitivity to mechanical vibrations, a remarkable non-linear dynamics derived from Lorentz forces and the fact that it is a non-collocated control problem. This implies that the control input and the output measurement are at different locations within the structure, making the system significantly more difficult to control.

In this way, the mechanical system selected for this test is a passive flexible structure mounted on a single-axis seismic table for the study of active mass dampers, shown in Figure 4.13. The structure has a capacitive accelerometer on its top in order to measure the vibration of the system and is controlled by the linear movement of the shaking table. At the same time, the shaking table is controlled by a high-torque motor connected to it via a rack-and-pinion system. The motor also has a high-resolution optical encoder with which the position of the shaking table is measured.

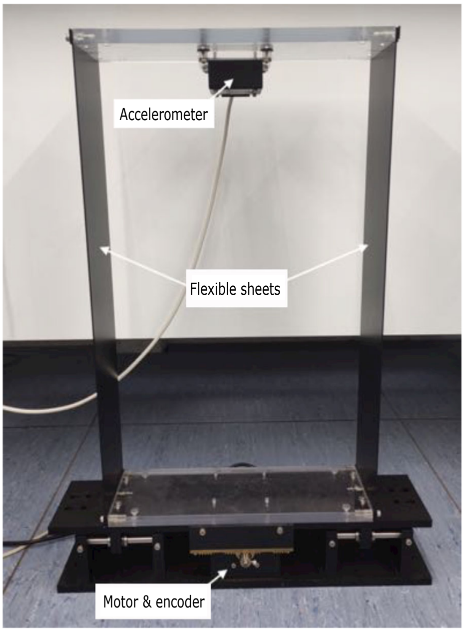

Figure 4.13.: Picture of the validation system. A flexible structure mounted in a seismic table.

As far as the control characteristics of the system are concerned, it is a system that tends to oscillate with relative ease, as it has a large resonance mode at 4 Hz. Thus, like resonant cavities, it is a system that is particularly sensitive to mechanical vibrations. In addition to this, the dead zone of the motor and the static friction in the pinion-rack system cause the dynamics of the system to have an important non-linear component. Finally, it is worth mentioning that it is a non-collocated control problem, as the main intent is to control the vibrations of the upper part of the structure by moving the lower platform.

## SEISMIC TABLE

This is a system commercialised by Quanser consisting of a stand and a stainless steel mobile platform. This platform slides along two guides by means of linear ball bearings, which are responsible for reducing the friction between the platform and the support. The motion is generated by a high quality DC motor capable of generating enough torque to accelerate masses of 5kg at 9.81m/s2. This movement is transmitted to the platform by means of a rack and pinion transmission system which has a maximum displacement range of 4 cm. In addition, the platform also has a position measurement system consisting of an optical encoder. The most relevant characteristics of the system are shown in table 4.1.

Table 4.1.: Technical specifications of the shake table I.

| **Symbol** | **Description** | **Value** | **Unit** |
|---|---|---|---|
| $\Delta x$ | Range of movement | 0.04 | m |
| $m_1$ | Moving platform mass | 1.5 | kg |
| $n_r$ | Rack holes | 30 | Teeth/m |
| $r_p$ | Pinion inner radius | 6.35 | mm |
| $n_p$ | Number of sprocket teeth | 12 | Teeth |

## DC MOTOR

The motor used in this system is a low-displacement, high-torque motor designed and marketed by the Pittman brand. More specifically, it is the **Pittman Express 1404S005** model. The technical specifications of the device are given in table 4.2. It is worth mentioning that in order to protect the integrity of the motor brushes, the bandwidth of all incoming signals has been limited to 50Hz.

Table 4.2.: Technical specifications of the DC motor Pittman Express 1404S005.

| **Symbol** | **Description** | **Value** | **Unit** |
|---|---|---|---|
| $\tau_{max}$ | Max torque | 1.4 | Nm |
| $k_m$ | Torque constant | 0.0612 | Nm |
| $k_b$ | Counter-electromotive force constant | 0.0612 | Vs/rad |
| $I_{max}$ | Max current | 22.9 | A |
| $R_m$ | Motor shell resistance | 1.5 | Ω |
| $L_m$ | Motor shell inductance | 1.6 | mH |
| $j_m$ | Moment of inertia of the motor | $2.64 \cdot 10^{-5}$ | $Kgm^2$ |

## OPTICAL ENCODER

The position of the mobile platform is measured by means of a quadrature digital optical encoder located at the rear of the motor, so the position measurements obtained are always relative to the initial position of the structure. The specific model of the encoder is **US Digital E3-2048-250-H** and its characteristics are listed in table 4.3.

Table 4.3.: Technical specifications of the Optical encoder US Digital E3-2048-250-H.

| Symbol | Description | Value | Unit |
|---|---|---|---|
| R | Resolution | 8192 | Accounts/rev |
| $S_e$ | Sensitivity | 4.87 | $\mu m$ |
|  | Type | TTL |  |

### FLEXIBLE STRUCTURE

This is a structure created by Quanser (model **AMD-1**) consisting of two flexible stainless steel sheets connected to each other at the ends by two methacrylate platforms. It is anchored vertically to the table described in the previous section by means of screws. In this particular case, it does not have any type of controllable moving element, making it a passive element. It includes an accelerometer which provides measurements of the acceleration of the upper platform of the structure. The most relevant characteristics are shown in table 4.4.

Table 4.4.: Technical specifications of the flexible structure.

| Symbol | Description | Value | Unit |
|---|---|---|---|
| l | Width | 320 | mm |
| h | Height | 500 | mm |
| d | Depth | 110 | mm |
| $m_2$ | Mass | 1.6 | kg |

### ACCELEROMETER

The top surface of the structure is equipped with a single-chip DC capacitive accelerometer with signal conditioning and a dynamic range going from -5g to 5g. It is calibrated by the manufacturer to generate 1 Volt per g of measured acceleration ($S_a = 9.8m/s^2V$). The accelerometer is capable of measuring both static and dynamic accelerations, and is mounted so that its sensitive axis is longitudinal to the structure.

## 4.3.2 | SYSTEM IDENTIFICATION

In order to have a preliminary idea of the dynamics of the system and as a starting point for the design of the loop shaping compensator, a simplified mathematical model has been developed, which represents the most relevant features of the system. For this purpose, and due to the complexity of the real dynamics of the structure, the mass-spring approximation was selected to serve as the foundation of the model.

First, it is important to model the dynamics of the DC motor. The process starts by defining the electrical equation based on the electrical schematic for a DC motor shown in figure 4.14.

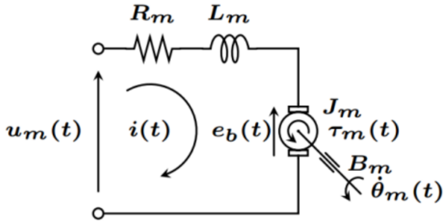

Figure 4.14.: Electric schematic of a generic DC motor.

Applying Kirchhoff's law to the DC motor schematic shown in figure 4.14, the following electrical equation is obtained.

$$u_m(t) = R_m i(t) + L_m \frac{di(t)}{dt} + e_b(t) \tag{4.11}$$

where $u_m$ is the input voltage to the motor, $i$ is the current flowing through the circuit, $e_b$ the counter-electromotive force and $R_m$ and $L_m$ the terminal resistance and inductance of the motor respectively.

In this particular case, it is possible to simplify the equation using the electrical motor constant elimination method, since $L_m$ is considerably smaller than $R_m$ (see table 4.2). Thus, the electrical equation is defined as the following.

$$u_m(t) = R_m i(t) + e_b(t) \tag{4.12}$$

On the other hand, the DC motor shall be considered to satisfy the following electromagnetic coupling ratios.

$$e_b(t) = k_b \dot{\theta}_m(t) \tag{4.13}$$

$$\tau_m(t) = k_m i(t) \tag{4.14}$$

where $k_b$ is the counter-electromotive force constant and $k_m$ is the torque constant of the motor. Both constants are equal when expressed in units of the same unit system, and represent the efficiency of the motor in converting electrical energy into mechanical energy.

Thus, by replacing the equation (4.13) in (4.12), it is possible to represent the electrical equation of the system as follows:

$$u_m(t) = R_m i(t) + k_b \dot{\theta}_m(t) \tag{4.15}$$

By isolating the intensity $i(t)$ in equation (4.15) and replacing it in equation (4.14) and taking into account that $\tau_m = r_p F_m$ and $\dot{x}_1(t) = r_p \dot{\theta}(t)$, the equation that relates the motor force to the voltage between its terminals is obtained.

$$F_m(t) = \frac{k_m}{R_m r_p} u_m(t) - \frac{k_m k_b}{R_m r_p^2} \dot{x}_1(t) \tag{4.16}$$

The next step is to parameterise the dynamics of the flexible structure. In this approach, the total mass of the system is divided into two. On the one hand the mass of the platform ($m_1$) and on the other hand the mass of the structure itself ($m_2$). In order to represent the oscillatory character of the system, these masses are connected to each other by means of an imaginary spring with an elastic constant $K_f$. The system to be studied is thus represented in figure 4.15, where $B_c$ is the coefficient of viscous friction corresponding to the load, $F_m$ is the force exerted by the motor on the load and $x_1$ and $x_2$ the linear positions of the upper and lower masses respectively.

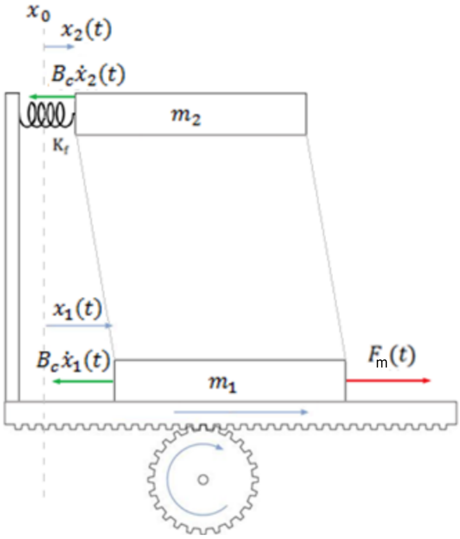

Figure 4.15.: Diagram of the approximate mass-spring system and the forces acting on it.

Note that the only oscillatory dynamic of the system is given by the imaginary spring, so the resulting approximation will only represent the most significant resonance of the real system, which will be a function of the unknown parameters $k_f$ and $B_c$. This is why, first of all, those parameters are approximated.

For this purpose, an experimental procedure was carried out in which, while keeping the position of the lower platform fixed, a thrust was manually applied to the upper part of the structure. Then, the acceleration of the upper platform was measured and the data was processed in Labview [9] to calculate both the frequency response and the envelope. Labview is a system design and development platform created by National Instruments that is widely used for the development of measurement, and control systems. It employs a graphical programming language, often referred to as "G" that is based in dataflow operation.

By keeping the position of the moving platform fixed ($x_1(t) = 0$), the system shown in figure 4.15 has been converted into a damped harmonic oscillator governed by the following time evolution equation.

$$\ddot{x}_2(t) = C_0 e^{-\gamma t} cos(\omega_n t + \phi_0) \tag{4.17}$$

where $C_0$ and $\phi$ are constants determined by initial condition and $\ddot{x}_2$ is the acceleration of the upper platform. At the same time, it is known that for a damped harmonic oscillator, the following relations are met.

$$\gamma = \frac{B_c}{2m_2} \tag{4.18}$$

$$\omega_n = \sqrt{\omega_0^2 - \gamma^2} \tag{4.19}$$

$$\omega_0 = \sqrt{\frac{k_f}{m_2}} \tag{4.20}$$

where $\omega_0$ is the harmonic frequency of the system.

In this way, to calculate the natural frequency of the system $\omega_n$, it is sufficient to measure the resonance peak observed in the Fourier transform of the measured acceleration, obtaining a value of 4 Hz, or $\omega_n = 25.133 rad/s$.

To obtain the damping coefficient $\gamma$, it is enough to adjust the envelope of the measured acceleration with the function $f(t) = C_0 e^{-\gamma t}$, obtaining a value of $\gamma = 0.142 rad/s$.

Substituting the values of $\gamma$ and $\omega_n$ into the equations (4.18-4.20) the parameters shown in the table 4.5 are calculated.

Table 4.5.: Parameters of the mass-spring approximation.

| $\omega_0$ | $B_c$ | $k_f$ |
|---|---|---|
| 25.133 rad/s | 0.454 kg/s | 1010.7 N/m |

In order to obtain the time evolution equations for both the top surface and the base of the structure, the system shown in figure 4.15 was solved using analytical mechanics.

The first step has been to formulate the Lagrangian, which is nothing more than the difference between the kinetic and potential energy of the system.

$$L = T - V \tag{4.21}$$

The total kinetic energy is equal to the sum of the contributions of both masses and the motor. The potential energy, in turn, is the energy stored in the imaginary spring. It is worth mentioning that the deformation of the imaginary spring is $x_1(t) - x_2(t)$ and the kinetic energy of the motor is defined as follows.

$$T_m(t) = \frac{1}{2} J_m \omega^2(t) = \frac{1}{2} \frac{J_m}{r_p^2} \dot{x}_1^2(t) \tag{4.22}$$

where $r_p$ is the radius of the pinion, $J_m$ is the moment of inertia of the rotor and $\omega(t)$ is its angular velocity.

The Lagrangian is thus defined as follows:

$$L = \frac{1}{2} m_1 \dot{x}_1^2(t) + \frac{1}{2} m_2 \dot{x}_2^2(t) + \frac{1}{2} \frac{J_m}{r_p^2} \dot{x}_1^2(t) - \frac{1}{2} k_f [x_1(t) - x_2(t)]^2 \tag{4.23}$$

The next step is to state the Lagrange equations.

$$\begin{cases} \frac{d}{dt} \frac{\partial L}{\partial \dot{x}_1} - \frac{\partial L}{\partial x_1} = Q_{x_1} \\ \frac{d}{dt} \frac{\partial L}{\partial \dot{x}_2} - \frac{\partial L}{\partial x_2} = Q_{x_2} \end{cases} \tag{4.24}$$

Bearing in mind that $Q_{x_1}$ and $Q_{x_2}$ are the external forces acting on the dynamics of $m_1$ and $m_2$ respectively, the following is obtained.

$$\begin{cases}(m_1 + \frac{J_m}{r_p^2})\ddot{x}_1(t) = k_f[x_1(t) - x_2(t)] = F_m(t) - (B_c + \frac{B'_m}{r_p^2})\dot{x}_1(t) \\ m_2\ddot{x}_2(t) + k_f[x_1(t) - x_2(t)] = -B_c\dot{x}_2(t)\end{cases} \tag{4.25}$$

Note that $Q_{x_1}$ is equal to the total force exerted by the motor minus the viscous frictional force generated by both mass 1 and the rotor. Similarly, $Q_{x_2}$ is equal to the viscous frictional force experienced by mass 2.

From this point on wards and in order to simplify the equations, the following equivalences will be used.

$$m_{eq} = m_1 + \frac{J_m}{r_p^2} \tag{4.26}$$

$$B_{eq} = B_c + \frac{B'_m}{r_p^2} \tag{4.27}$$

In order to be able to operate with the system of differential equations more easily, the equivalences (4.26) and (4.27) have been introduced and the Laplace transform has been applied under zero initial conditions.

$$\begin{cases}m_{eq}s^2X_1(s) + k_f[X_1(s) - X_2(s)] = F_m(s) - B_{eq}sX_1(s) \\ m_2s^2X_2(s) + k_f[X_1(s) - X_2(s)] = -B_csX_2(s)\end{cases} \tag{4.28}$$

Operating on the system of equations (4.28) the expression relating $X_1(s)$ to $X_2(s)$ is obatined.

$$X_2(s) = \frac{k_f}{m_2s^2 + B_cs + k_f}X_1(s) \tag{4.29}$$

At this point, substituting the equations (4.29) and the Laplace transform of $F_m(t)$ (4.16) into the first equation of (4.28), an equation only in terms of the input voltage to the motor $U_m(s)$ and the position of the moving platform $X_1(s)$ is obtained.

$$m_{eq}s^2X_1(s) + k_f\frac{m_2s^2 + B_cs}{m_2s^2 + B_cs + k_f}X_1(s) + B_{eq}sX_1(s) + \frac{k_mk_B}{R_mr_p^2}sX_1(s) = \frac{k_m}{R_mr_p}U_m(s) \tag{4.30}$$

In this way, the transfer function relating the input voltage to the motor and the position of the moving platform can be defined as follows.

$$G_{x_1}(s) = \frac{X_1(s)}{U_m(s)} = \frac{\frac{k_m}{R_m r_p}}{m_{eq}s^2 + (B_{eq} + \frac{k_m k_B}{R_m r_p^2})s + k_f(\frac{m_2 s^2 + B_c s}{m_2 s^2 + B_c s + k_f})} \tag{4.31}$$

Lastly, by using in equation (4.31) the values of the parameters provided by the manufacturer (tables 4.1, 4.2 and 4.4), as well as those calculated in section this section (table 4.5), it is obtained that the transfer function $G_{x_1}$ can be defined as follows.

$$G_{x_1}(s) = \frac{X_1(s)}{U_m(s)} = \frac{2.98(s^2 + 0.284s + 631.712)}{s(s + 24.11)(s^2 + 9.546s + 879.911)} \tag{4.32}$$

Substituting equation (4.32) into equation (4.29), the transfer function relating the input voltage of the motor with the position of the top surface of the structure is calculated.

$$G_{x_2}(s) = \frac{X_1(s)}{U_m(s)} = \frac{1881.3}{s(s + 24.11)(s^2 + 9.546s + 879.911)} \tag{4.33}$$

This system can also be described by its state space representation as shown in equation (3.2) where **A**, **B** and **C** are the following matrices.

$$\mathbf{A} = \begin{pmatrix} 0 & 0 & 1 & 0 \\ 0 & 0 & 0 & 1 \\ -469.063 & 469.063 & -33.38 & 0 \\ 631.6875 & -631.6875 & 0 & -0.3125 \end{pmatrix} \tag{4.34}$$

$$\mathbf{B} = \begin{pmatrix} 0 & 0 & 2.087 & 0 \end{pmatrix}^T \tag{4.35}$$

$$\mathbf{C} = \begin{pmatrix} 1 & 0 & 0 & 0 \\ 631.6875 & -631.6875 & 0 & -0.3125 \end{pmatrix} \tag{4.36}$$

By analyzing the bode diagram relating the input of the system $U_m(s)$ to the position of the moving platform $X_1(s)$ shown in figure 4.16, it is obvious that it has similar characteristics to the piezo tuner studied in section 4.2.3. Although the system is simpler, as only the most significant resonance has been characterised, it suffers from the same stability problem. This is caused by the fact that the resonance-antiresonance pair at 4 Hz makes the phase at that frequency very close to -180 degrees. Thus, when the time delay is sufficiently big, the phase will exceed -180 degrees, generating a phase crossover frequency where the gain is greater than 0 dB, and in conclusion, destabilising the system.

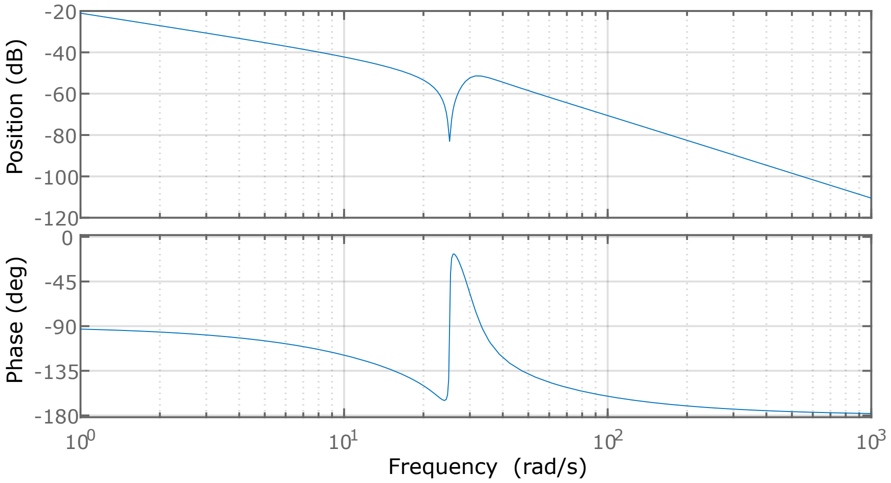

Figure 4.16.: Bode diagram of the $G_{x_1}$ transfer function.

## 4.3.3 | EXPERIMENTAL SETUP

For the experiment, a myRIO-9000 [48] was used to host the control algorithm. This device is a modular embedded control and acquisition system developed by National Instruments (NI). It is designed for applications that require real-time processing, high-speed data acquisition, and reliable performance in harsh environments. The general architecture of a myRIO involves a microprocessor running a real-time operative system, a Field Programmable Gate Array (FPGA) and and a set of analogue and digital inputs and outputs. See Appendix C.2 for more information.

In this way, the MLADRC algorithm was developed using LabView Real-Time and was run on the real-time processor of the myRIO. The analog I/O terminals of the Mini System Port (MSP) of the device were used to generate and acquire the nedeed signals. Figure 4.17 shows a schematic of the experimental setup.

The myRIO acquires both the acceleration signal from the upper platform and the position of the lower platform via the analogue input/output terminals. The MLADRC algorithm implemented for this particular system assigns a weight

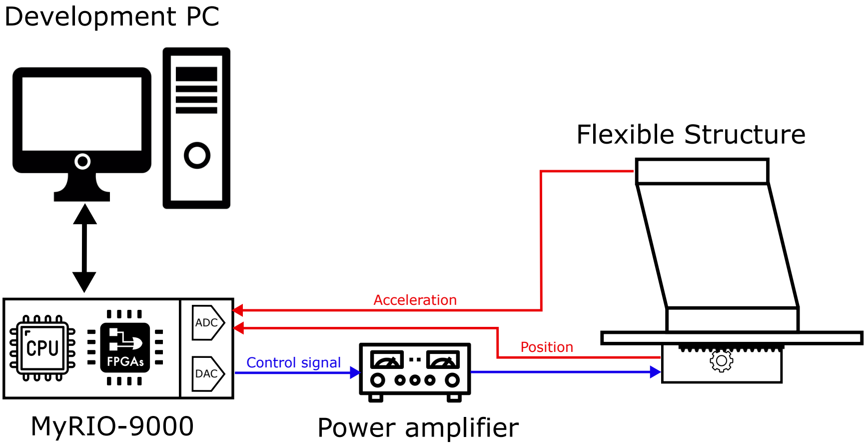

Figure 4.17.: Scheme of the experimental setup used for the flexible structure testing.

to each of these magnitudes and adds them together to then apply the control to that new magnitude. In this way, the algorithm tries to minimize both the position error of the lower platform and the acceleration of the top platform. Once the control signal is computed it is amplified by a power amplifier and sent into the motor of the structure. The myRIO is connected via USB to a development PC where the parameters of the system can be monitored.

## 4.3.4 | EXPERIMENTAL RESULTS

In this section, the controller and stabilisation techniques developed throughout this work are applied to the actual flexible structure.

### | MLADRC PERFORMANCE WITHOUT DELAY

First, the generic performance of the MLADRC for the mechanical system given by matrices (4.34-4.35) has been measured. For that purpose, the MLADRC structure described in figure 4.1 was implemented on a myRio device using LabVIEW and its performance was compared with that of a PID.

In order to make an objective comparison between both algorithms, it is important to set the parameters ofthe PID to an acceptable level of optimisation. For this purpose, a genetic algorithm based on BLX-alpha crossover [25] was developed to find the optimal parameters for the PID. This algorithm starts the first iteration by implementing on the mathematical model defined by the matrices (4.34-4.36) the controller to be optimised with random parameters, and calculates its performance by measuring several parameters of interest such as overshoot, rise time, RMS etc. For the next iterations, the algorithm retains the top 20% of controllers and adds new random controllers to the pool and repeats the process, until the controllers exceed user-set standards.

After extensive testing, the optimal parameters for the PID were defined as $K_p = 3$ , $K_i = 12$ and $K_d = 0.006$. Similarly, it was determined that a second-order MLADRC with a GESO bandwidth of $\omega_e = 250Hz$ and a controller bandwidth of $\omega_c = 15Hz$ is an acceptable compromise between smooth dynamics and good disturbance rejection. In this way, the $L_0$ and $K_0$ matrices (see chapter 4.1) have been set to place the observer poles at 250 Hz (three poles) and the controller poles at 15 Hz (two poles). As shown in figure 4.18, the performance of the MLADRC algorithm is superior to that of a PID, because it offers five times less overshoot and much better vibration rejection.

The sampling time used in the discrete implementation of the controller has been 0.5 milliseconds, thus restricting the MLADRC to a maximum bandwidth of 1 KHz.

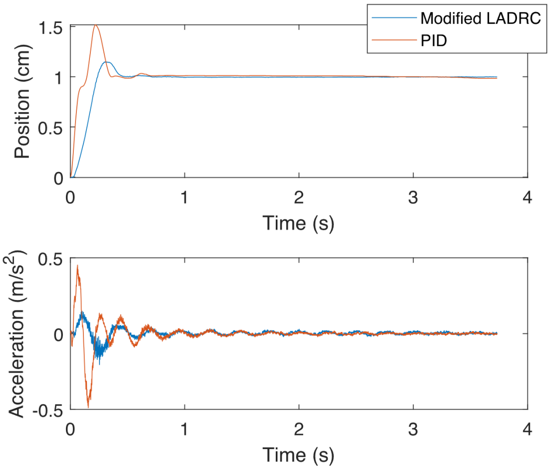

Figure 4.18.: Step response of the non-delayed system controlled by a well-tuned PID versus the proposed MLADRC. The graph above shows the position of the mobile platform while the lower graph shows the acceleration of the top platform.

## STABILIZATION OF THE DELAYED SYSTEM BY LOOP SHAPING

To test the proposed stabilization procedure, the control signal has been delayed via software by 5 ms, making the system unstable. Analysing the resulting control signal shown in figure 4.19, it can be concluded that the system instability grows in a frequency range around 97 Hz. Thus, a compensation around that frequency is necessary in order to maintain the stability.

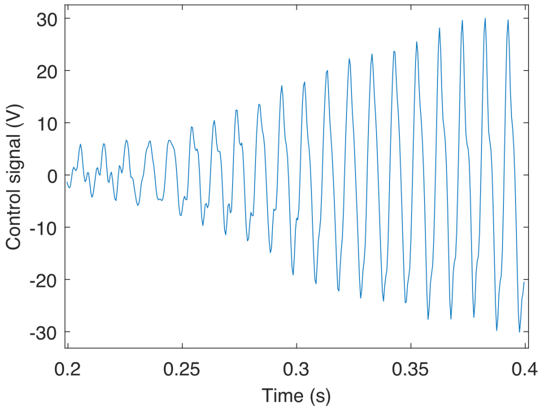

Figure 4.19.: Unstable control signal using the MLADRC with $\tau = 0.005s$.

In this way, a digital notch filter centered in 97 Hz was implemented as a loop shaping compensator, in order to stabilize the system and improve its dynamics. In this case, the stability is obtained limiting the gain around the critical frequency.

$$H_{notch}(z) = \frac{z^2 - 1.911z + 0.9975}{z^2 - 1.753z + 0.8396} \tag{4.37}$$

Figure 4.20 compares the step response of the non delayed system controlled by the original MLADRC, with the step response of the delayed system controlled by the MLADRC plus the loop shaping compensator. Recall that the objective of the stabilisation by loop shaping techniques is that the MLADRC algorithm withstands higher time delay values while maintaining performance. As it is shown in the step response, the MLADRC provides a better time response, even though it has to deal with the added delay, which is a clear sign of the controller's validity.

In order to analyse the disturbance rejection capabilities of the MLADRC and to observe whether its performance has decreased in this aspect in the stabilisation process, the top of the structure is struck in a controlled manner with a mass attached to a pendulum. The process is carried out with the non-delayed system controlled by the original MLADRC (no added filter) and with the delayed system controlled by the MLADRC plus a stabilization filter. Figure 4.21 shows how the stabilized MLADRC not only maintains its performance, but is able to reduce the acceleration of the top surface of the structure in less time than the MLADRC with no loop shaping, even when a delay is added to the control signal.

In conclusion, the resulting controller keeps the system's step response al-

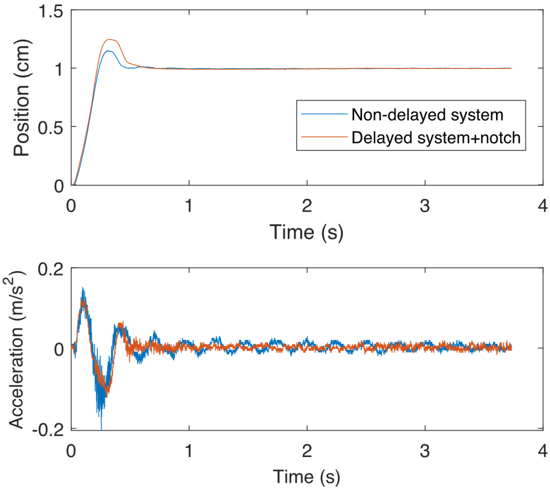

Figure 4.20.: Step response of the delayed ($\tau = 0.005s$) system controlled by the stabilized MLADRC plus notch filter versus the step response of the non-delayed system controlled by the MLADRC without stabilization. The graph above shows the position of the mobile platform while the lower graph shows the acceleration of the top platform.

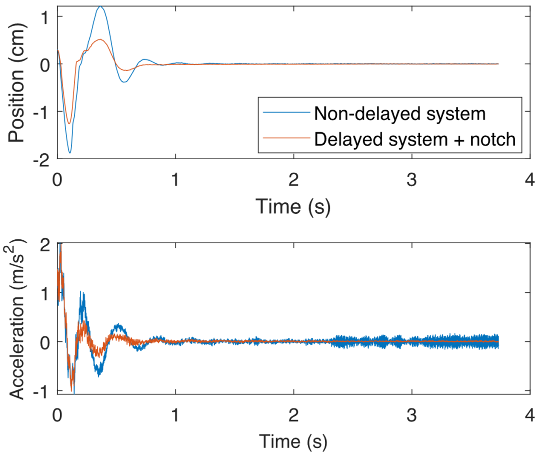

Figure 4.21.: External disturbance response of the delayed ($\tau = 0.005s$) system controlled by the stabilized MLADRC versus the step response of the non-delayed system controlled by the MLADRC without stabilization. The graph above shows the position of the mobile platform while the lower graph shows the acceleration of the top platform.

most identical and improves to a large extent the disturbance rejection (see figures 4.20 and 4.21 respectively), validating the proposed loop shaping-based compensation MLADRC scheme.

# CHAPTER 5

# MLADRC ALGORITHM APPLIED TO A SRF TESLA CAVITY

Now that the potential of the MLADRC algorithm has been demonstrated and its design process has been validated, both in simulation and experimentally, the algorithm is applied to the system that originally concerned us, a SRF TESLA cavity. For this purpose, the same process will be followed as for the flexible structure, which is summarised in a mathematical modelling phase, followed by a designing phase in simulation to finish with the experimental implementation in the cavity itself. This procedure will be explained in this last chapter.

## 5.1 | HoBiCaT facility for SRF systems

The success of the TESLA Test Facility (TTF) in showcasing the reliable operation of TESLA equipment has led to several proposals for CW linear accelerators built on this technology. These CW machines are designed for moderate energies (2–5 GeV) with minimal beam loading, allowing for continuous wave operation.

While much of the TESLA technology can be directly applied to CW machines, the shift to continuous wave operation introduces new challenges not necessarily addressed in TTF. Recognizing this, HZB constructed in 2003 a horizontal test facility named HoBiCaT [58] (Horizontal Bi-Cavity Test-facility). This facility enables swift testing and turnaround of SRF elliptical cavities in general and TESLA cavities in particular. Its design draws inspiration from the CRYHOLAB [80] and CHECHIA [17] systems developed at the Orsay and Saclay institutes, respectively.

The HoBiCaT test facility includes a cryostat, feedbox, helium refrigeration plant, RF power supply and space for two 9-cell elliptical cavities with its associated ancillary equipment. All of it is placed inside a bunker to protect operators and equipment from radiation.

### 5.1.1 | CRYOSTAT DESIGN

The horizontal vacuum tank (Figure 5.1) is capable of accommodating two complete TESLA 9-cell cavities or one TESLA superstructure, along with RF couplers, tuners, and helium tanks. The generously sized tank, with interior dimensions of 1.1 m in diameter and 3.5 m in length, is also versatile enough to house larger cavities, extending up to 500 MHz.

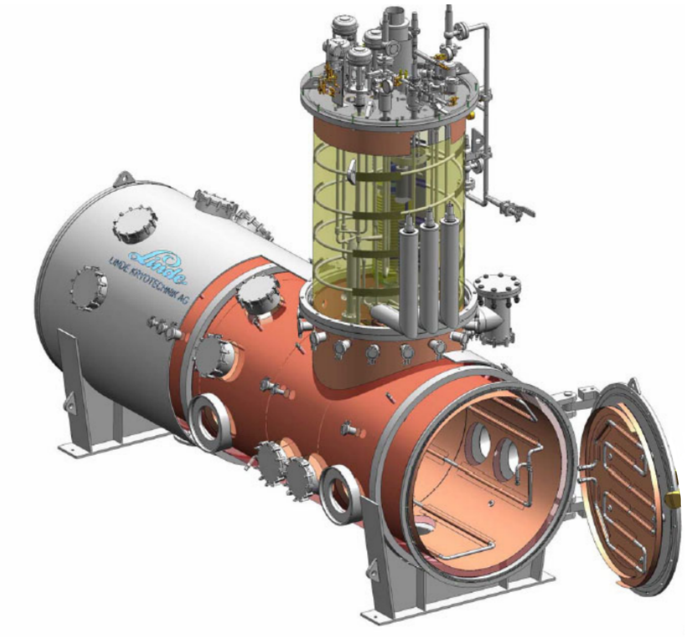

Figure 5.1.: The HoBiCaT cryostat [58].

Power couplers access the vacuum vessel through two of the four large feedthroughs located on the side, mirroring the arrangement seen in TESLA modules. Numerous diagnostic ports are incorporated for additional instrumentation. Conveniently positioned doors at each end provide rapid access to the unit.

A feedbox is situated on the main vessel, receiving 4.2K liquid helium (LHe) from the HZB cryoplant. This feedbox then supplies the cavities with either 1.8–2.2K or 4.2K LHe.

### 5.1.2 | Cryogenic system

Figure 5.2 illustrates the cryogenic scheme of the HoBiCaT cryostat. 4.2K helium from the cryogenic plant of HZB is collected in a 50-liter vessel in the feedbox. From here, helium passes through a heat exchanger and is expanded via a Joule-Thompson effect valve into a 2-phase line. This in turn supplies the two cavity helium vessels with He. A reservoir with a heater and a level meter at the end of the two-phase line is used for level control and to balance the dynamic heat load of the cavities.

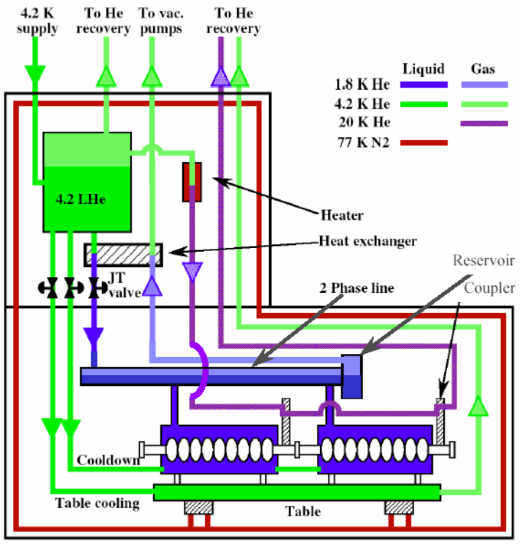

Figure 5.2.: Cryogenic system in HoBiCaT [58].

There are additional secondary cooling loops in HoBiCaT serving various purposes. One of these is a 4.2K He supply line intended for filling the helium vessels from the bottom during the cooldown process. Another 4.2K Helium line is in place to cool the table that supports the cavities. Additionally, there is a helium-gas line designed to cool heat intercepts on the input couplers, which includes a heater that enables temperature variation from 4.2 K to 20 K. Finally, a liquid nitrogen loop is implemented to cool the 77K radiation shield.

### 5.1.3 | RF power

Initially the main RF power source was a 10 kW CPI klystron adapted from the CEBAF 1.5-GHz design scaled to 1.3 GHz, but at the moment, two 15 kW CW Solid State Amplifiers (SSA) can be used operating at 1.3 GHz and 1.5 GHz. These SSA are located outside the bunker so the RF is transmitted through high power coaxial lines and waveguides. The RF chain also includes the circulators and water loads to protect the SSA from reflected power. Since beam loading is absent, 10 kW are sufficient for HoBiCaT tests, which is enough to compensate microphonic detuning up to 35 Hz at 20 MV/m.

## 5.2 | CHARACTERIZATION OF THE TUNER-CAVITY SYSTEM

Although knowing the dynamics of the system is not strictly necessary to design the MLADRC, it is very useful when analyzing its viability and studying the effect of its different components. The availability of an approximate transfer function allows analytical design of the controller, including the loop shaping compensator, to later validate its operation in the real system.

It is important to emphasize that the experimental part of this work takes advantage of the measuring setup, and all the previous study carried out by Dr. Neumann and colleagues [68].

### 5.2.1 | DETUNING MEASUREMENT

The resonance frequency of a cavity is exclusively dependent on its geometry. Thus, when a vibration is coupled to the system, it generates a micro-metrical deformation that causes a drift in its resonance frequency. In TESLA cavities, a change of the cavity length by a mere 1 nm results in a frequency shift of 0.3 Hz, which is specially relevant when operating with high $Q_L$, due to the extremely narrow bandwidth of the cavity.

When a cavity is fed by a fixed frequency derived from a master oscillator and a detuning event occurs, the cavity responds with a reduction of the field amplitude and a phase shift ΔΦ. It is possible to relate the detuning Δf to the phase shift by means of the following equation [68].

$$\Delta f(t) = \frac{f_0}{2Q_L} tan[\Delta\Phi(t)] \tag{5.1}$$

where $f_0$ is the fundamental resonance frequency. Thus, the phase shift can be used to measure and control the detuning. Note that equation (5.1) is only valid in steady state, which corresponds to detuning values comprised within the cavity half bandwidth. For TESLA cavities operating with $Q_L$ larger than $10^7$, the half bandwidth is approximately 65 Hz.

The scheme provided in Figure 5.3 presents an overview of the RF measure-

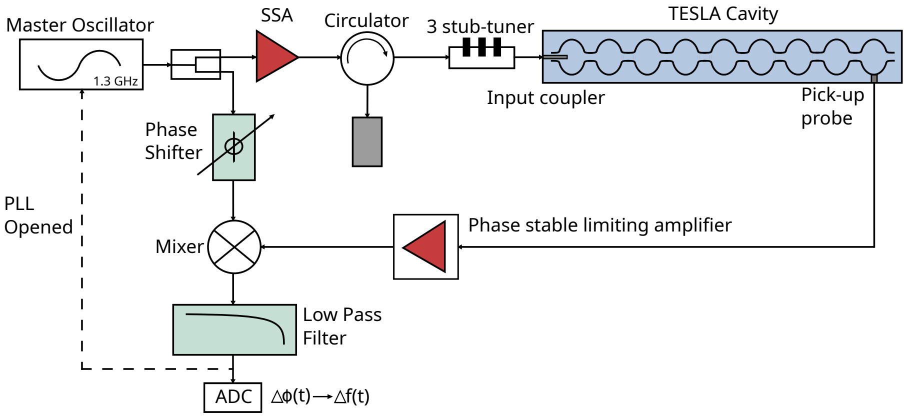

Figure 5.3.: Standard RF setup at HoBiCaT for continuous wave detuning measurement.

ment setup used at HZB's HoBiCaT (Horizontal Bi-Cavity Test facility) [58] for detuning measurements. The cavity operates in an open loop configuration, driven by a tunable master oscillator. The forward wave signal from this source is split to create a signal path for phase error measurement.

In order to feed the cavity, the RF signal is amplified by a SSA. By utilizing a three-stub tuner [42] and adjusting the variable penetration depth of the TTF-III input coupler antenna [57] into the beam pipe coupler port, the coupling strength can be varied. This allows for coverage of $Q_L$ ranging from $2 \cdot 10^8$ down to $5 \cdot 10^6$.

To extract the transmitted power signal and observe the excited RF resonance of the cavity, a pickup antenna with a weak coupling strength ($Q_{ext} \approx 5 \cdot 10^{11}$) is employed.

For precise phase and detuning measurements, the transmitted power signal undergoes amplification using a phase-stable limiting amplifier to eliminate amplitude variations. This ensures a clean phase shift measurement between the reference signal and the transmitted signal at a low-noise RF mixer. Any phase offsets introduced by the RF cabling can be compensated using a phase shifter in the reference signal path.

The phase error signal is further processed by a low-pass filtering amplifier to optimize the signal-to-noise ratio, eliminate higher-frequency components of the mixing process, and prevent aliasing caused by the subsequent sampling process. Sampling frequencies within the range of 1.0-5.0 kHz are chosen to cover the detuning range of several hundred Hertz.

## 5.2.2 | TRANSFER FUNCTION MEASUREMENT

Each accelerating cavity in an accelerator is equipped with a tuning system to adjust the resonance frequency to the desired operating point. In the case of elliptical niobium cavities, stepper motors are utilized along with a lever system to alter the cavity's length. For TESLA cavities, the tuning systems must have a range of approximately 300-500 kHz to compensate for manufacturing tolerances and changes that occur during cooldown.

To compensate the dynamic Lorentz-force detuning, caused by the pulsed RF mode of operation, modern tuning systems often incorporate an integrated piezo-tuner that helps mitigate such fast detuning events.

In the case of CW operated cavities, the pulsed Lorentz-force detuning is not a mayor concern. However, these fast tuners can still be utilized to compensate for microphonic detuning, which arises from external mechanical vibrations or acoustic disturbances affecting the cavity's resonance.

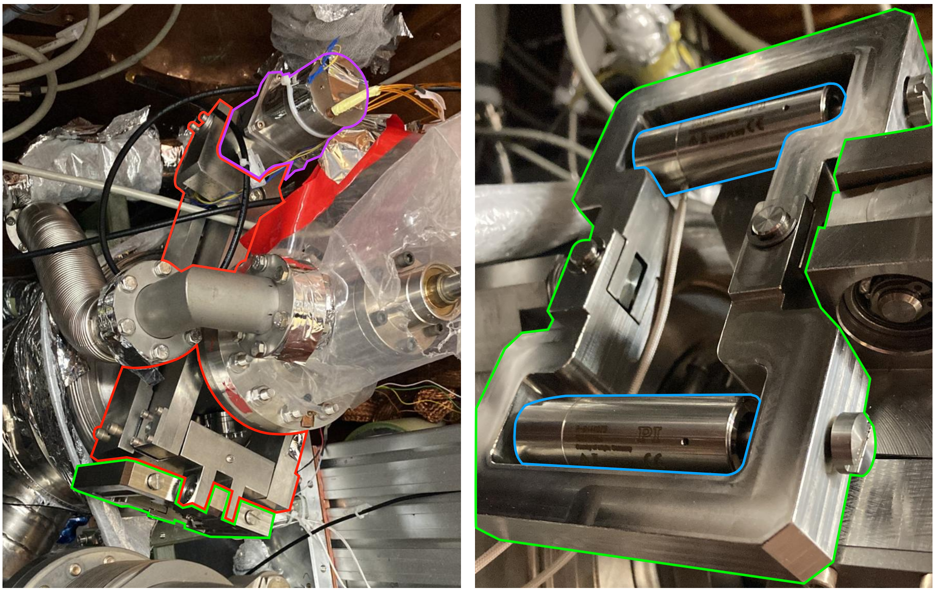

Figure 5.4.: Saclay tuning system for TESLA cavities. The left picture shows a Saclay-II tuner (red) with a step motor (purple) and a piezo holder (green) mounted on the cryovessel of the cavity. The right picture displays the piezo holder frame (green) designed in HZB with two piezos mounted (blue).

In this particular case and as can be seen in Figure 5.4, the cavity has a Saclay-II type tuner in which a P-844K075 encapsulated piezo actuator is incorporated [74]. This piezo tuner consists of two piezo-ceramic stacks mounted in a steel sheath.

The setup for measuring the transfer function between the piezo drive signal and the detuning response of the cavity is illustrated in Figure 5.5. To ensure precise measurements by excluding the low-pass characteristics resulting from the narrow cavity bandwidth, the loop is closed, operating in a phase-locked-loop configuration. The measurement itself is performed with a lock-in amplifier, which generates the excitation signal while performing low noise measurements.

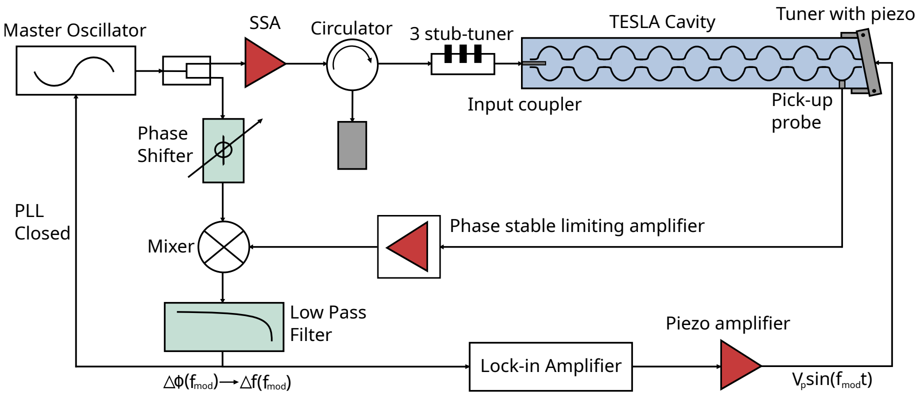

Figure 5.5.: Measurement setup to obtain the transfer function between piezo excitation and cavity detuning response.

Making use of the piezo-actuator, the system was excited by a sinusoidal signal of variable frequency. A frequency sweep was performed between 0 and 800 Hz, with a step of 0.2 Hz. To account for the unknown quality factor of the mechanical modes prior to the measurement, each frequency step was measured for a minimum duration of 2.4 seconds. This extended measurement time allowed for the acquisition of the steady state response for each data point.

Figure 5.6 depicts the transfer function that relates the piezo drive signal and the generated detuning. Given the narrow bandwidth of the cavity in low beam-loading CW machines, the contribution of eigenmodes above 100 Hz will have limited significance. However, it is important to note that they are relevant in terms of system stability. In fact, the resonance mode at 160Hz generates an abrupt jump in the phase of the system making its phase margin barely 2 degrees. This means that the system's closed-loop relative stability is extremely low. In addition, above that frequency, the phase continues to deteriorate, which makes it difficult to control this system by means of a feedback controller, at least in that frequency range.

Looking at the group phase, it is possible to infer that the system delay is approximately 1.2 milliseconds. This derives from the intrinsic delay of the piezoelectric actuator and mechanical tuner. It is important to note that, as previously stated, this time delay is especially harmful to system stability, as it

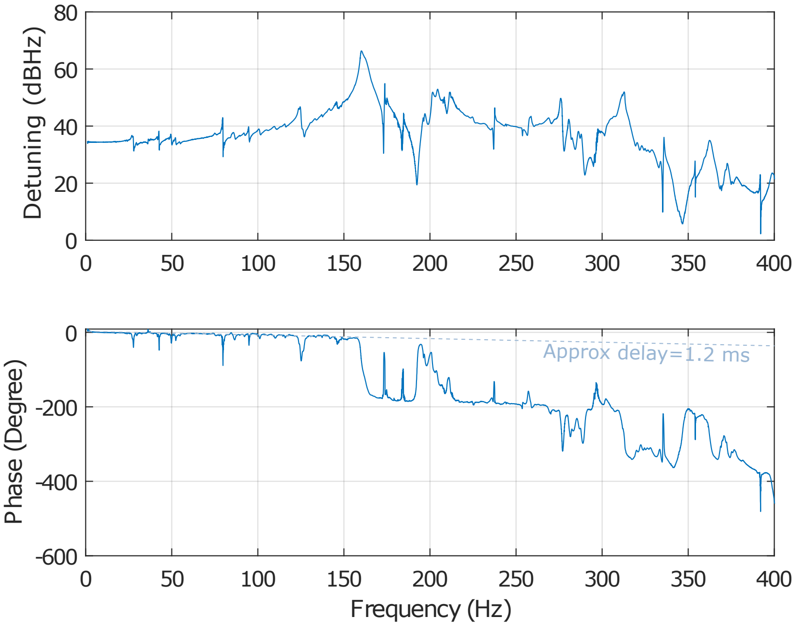

Figure 5.6.: frequency response of the system composed by the Saclay-II tuner and the TESLA cavity. The graph relates the piezo drive signal with the detuning generated in the cavity.

degrades the phase of the system and can cause a phase crossover at frequencies where the system gain is still higher than 0 dB.

## 5.3 | ANALYSIS AND DESIGN IN SIMULATION

As previously mentioned, due to the mechanical characteristics of the cavities, feedback controllers tend to destabilize these systems even at very low gains, obtaining effective bandwidths of only a few Hertz. The objective of this controller implementation is to reduce the detuning caused by stochastic effects over the widest possible bandwidth, to demonstrate the feasibility of the MLADRC algorithm and to discuss its advantages over more traditional controls such as the PID.

Since a frequency response of the system is available, it is possible to perform a theoretical analysis and design of the controller using tools such as the Bode and Nyquist diagrams. In addition, this allows to compare the expected theoretical behavior and the real one, to ensure unequivocally the feasibility of the design method and the MLADRC algorithm.

As discussed throughout the chapter, the objective of the control to be implemented is to reduce stochastic detuning as much as possible in the maximum possible bandwidth. For this purpose, and due to the relatively large system delay, it will be necessary to find a compromise between disturbance suppression and system stability in closed loop.

Figure 5.7 depicts the frequency response of a second order MLADRC algorithm as a function of the bandwidth of the controller $f_c$.

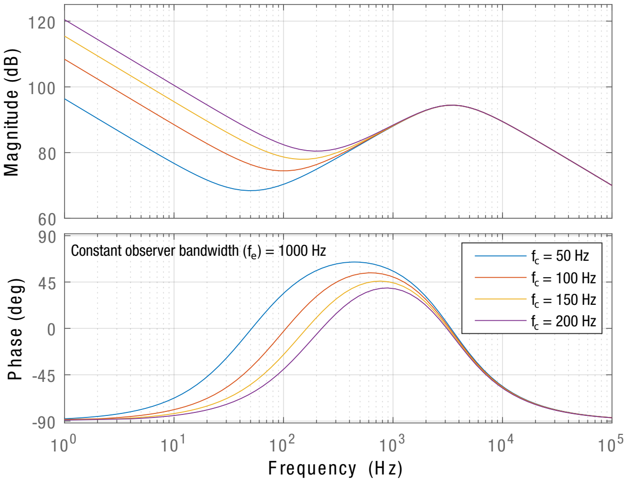

Figure 5.7.: Bode diagram of a second order MLADRC algorithm as a function of the bandwidth of the controller $f_c$.

The more the bandwidth of the controller is increased, the more the system gain increases at low frequencies, indicating an improvement in disturbance rejection in that frequency range. As far as the phase is concerned, it is possible to observe how the phase increment decreases the higher $f_c$ is. Considering the transfer function shown in Figure 5.6, the objective for stabilizing the closed-loop system is to improve the phase in the 160-190Hz range, so the higher the phase increment of the controller, the more stability it will bring to the system. In conclusion, detuning suppression capabilities increase with the controller bandwidth ($f_c$), but the stability it brings to the system decreases.

Repeating the same process with the observer bandwidth ($f_e$) and as shown in Figure 5.8, the controller gain increases the larger $f_e$ is, although it should be noted that the effect is greater at higher frequencies. This means that in the case of a system with delay, the bandwidth of the observer can negatively influence the stability of the system, since for the system to be stable, it is necessary that the gain of the controlled system is less than 0 dB above the phase crossover frequency. As far as phase is concerned, it improves the wider the bandwidth, so in theory, for a non delayed system, the performance of the controller is higher

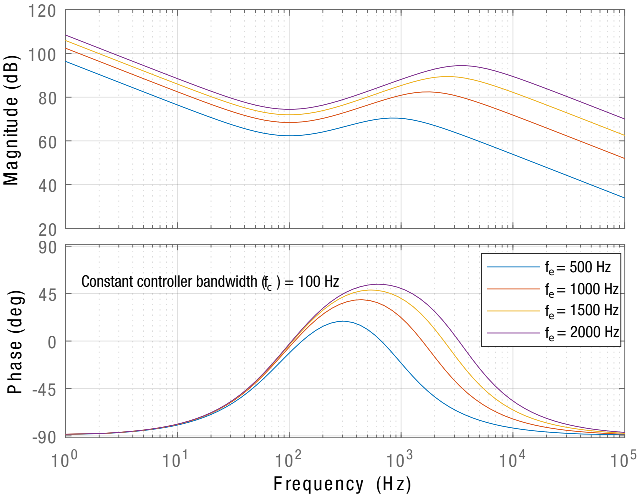

Figure 5.8.: Bode diagram of a second order MLADRC algorithm as a function of the bandwidth of the observer $f_e$.

the wider the bandwidth of the observer. In this particular case, as the system has a relatively large delay, the bandwidth of the observer is limited by the stability of the system, since it is not desirable for the system gain to be high at high frequencies. In addition, the phase distortion arising from the discretization when the observer dynamics is too fast is also detrimental for the stability of the system. It should also be taken into account that the higher the bandwidth $f_e$, the higher the execution speed of the controller and consequently the higher the needed computational power of the hardware used.

Based on the above, it is determined that a second order MLADRC with bandwidths of $f_c = 170Hz$ and $f_e = 2000Hz$ is appropriate for this particular system. To adjust the controller, the gain G is gradually increased until the best disturbance rejection performance is achieved. This information is obtained from the magnitude of the bode diagram of the closed-loop system. It should be noted that as the gain increases, the stability of the system decreases until destabilization is reached. Thus, it is important to reach a compromise between performance and relative stability. To analyze the stability of the system, it is possible to study the Nyquist diagram of the open-loop system. By following this process, a gain of $G = 3.62 \cdot 10^{-6}$ is obtained.

At this point, the objective is to improve the relative stability of the system in order to further increase the gain and achieve a better suppression of disturbances as well as a wider bandwidth. This can be done by implementing a large range of filters as a loop shaping compensator device, which is a key component of the proposed MLADRC. By analyzing the frequency response of the open loop system when the instability occurs, it is determined that the instability is generated at around 170 Hz, as could already be predicted by observing the transfer function shown in figure 5.6. Thus, a notch filter centered at 170 Hz is implemented in order to decrease the gain of the controller in that particular frequency and stabilize the system. Looking at the Nyquist diagram shown in figure 5.9, it can be seen that in the unstabilized system (blue line), there is a resonance surrounding the point (-1,0), which is the one located at 170 Hz. After applying the notch filter and stabilizing the system, it can be noticed how the circumference that represents that resonance decreases to the point of not surrounding the point (-1,0) anymore. The continuous version of this filter is defined by equation (5.2) and its effect can be seen in the nyquist diagram in figure 5.9.

$$H_{notch} = \frac{s^2 + 1140926}{s^2 + 854s + 1140926} \tag{5.2}$$

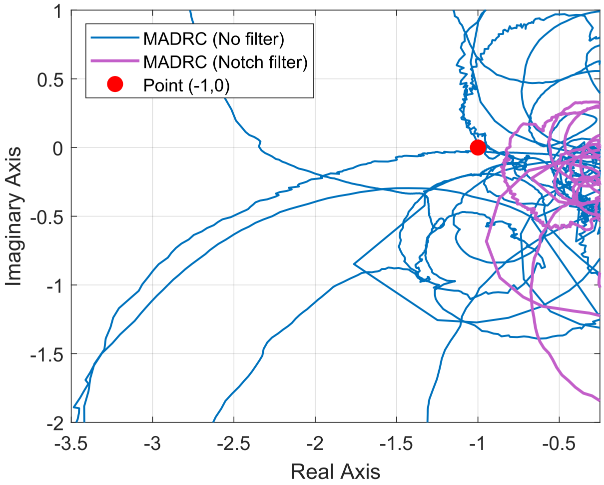

Figure 5.9.: Nyquist diagram of the system with and without loop shaping compensator. The Gain of the controller for both cases is $7.5 \cdot 10^{-6}$.

Once the system is stabilized by the filter, it is possible to further increase the gain (G=$9.1 \cdot 10^{-6}$) of the controller to improve its performance. Figure 5.10 shows the closed-loop frequency response to disturbances of the system for the MLADRC with and without loop shaping compensator. It is also shown the system response with a well-tuned proportional (P) and proportional-integral (PI) controller. Those controllers where tuned through numerical computation using frequency domain techniques.

Comparing the MLADRC with the PI, the former offers greater detuning reduction over a wider bandwidth, approximately 30 Hz. It is also demonstrated that with the appropriate loop shaping compensator, a notch filter in this case,

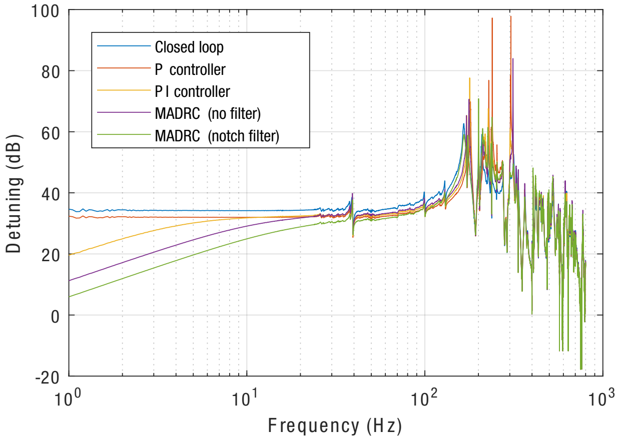

Figure 5.10.: Frequency response of the closed-loop system for different controllers.

it is possible to improve the performance of the controller by making it more stable and thus increasing its gain.

## 5.4 | DESIGN VALIDATION USING SIMULINK

So far, all simulations concerning the controller have been performed using the mechanical model of the cavity, which is nothing more than the mathematical function relating the incoming voltage to the piezo tuner to the detuning generated in the cavity. Although a good starting point, these simulations are limited in their ability to represent reality, as resonant cavities are complex systems in which electromagnetic and mechanical dynamics are tightly coupled. When the detuning increases, the cavity voltage gradient decreases, making the Lorentz forces impinging on the cavity walls smaller as well. This, in turn, generates changes in the cavity detuning that again affect the cavity voltage, and so forth.

To have an additional test of the performance of the controller including non-linear effects, a Simulink model has been used which includes the coupling between the mechanical and electromagnetic part of the cavity, as well as the detuning estimator to be used in the real system. It should be remembered that the electromagnetic-mechanical coupling is produced through the Lorenz force detuning, which introduces non-linear dynamics that pose an additional challenge for the controller.

### 5.4.1 | MODEL DESCRIPTION

This section describes the mathematical model used in the validation process. First of all, it is worth mentioning that a large part of the model was previously designed by HZB researchers for use in their own investigations. Even so, it is considered useful to set out the foundations of this initial model in order to later present all the improvements and refinements that have been implemented in it as a result of this work. Thus, the Simulink model designed in HZB [24] is taken as a starting point.

Regarding the electromagnetic dynamics, the behavior of the RF envelope of the transmitted voltage without beam loading is represented in the simulation model by the following equation:

$$\frac{d}{dt}\mathbf{V}_{cav} = \begin{pmatrix} -\omega_{1/2} & -\Delta\omega \\ \Delta\omega & -\omega_{1/2} \end{pmatrix} \mathbf{V}_{cav} + \begin{pmatrix} R_L\omega_{1/2} & 0 \\ 0 & R_L\omega_{1/2} \end{pmatrix} \frac{\mathbf{I}_{amp}}{m} \tag{5.3}$$

where $\omega_{1/2} = \frac{\omega_0}{2Q_L}$, $R_L$ is the loaded impedance defined as $R_L = \frac{R}{1+\beta}$ and $\Delta\omega$ is the detuning defined as the difference between the driving frequency and the RF resonance frequency ($\Delta\omega = \omega_0 - \omega$). At the same time, $\mathbf{V}_{cav}$ and $\mathbf{I}_{amp}$ are the cavity voltage and RF power source current, respectively, represented by their real and imaginary part, $\mathbf{V}_{cav} = (V^r_{cav}, V^i_{cav})^T$ and $\mathbf{I}_{amp} = (I^r_{amp}, I^i_{amp})^T$. See section 2.2.2 for more detail about the EM behavior of the cavity. Note that since in this case, the input to the system is the current generated directly in the RF power amplifier, the incident current in the cavity is defined as $I_{amp}/m$, where $m$ is the winding ratio of the ideal transformer of the equivalent RLC circuit (see equation (2.20)).

In summary, a simplified electromagnetic model with two inputs is presented, which characterises the fundamental mode of the EM resonance of the cavity. On the one hand, the RF power source current $\mathbf{I}_{amp}$, which dictates the general dynamics of the system, and on the other hand, the detuning $\Delta\omega$, which is used to couple the mechanical dynamics to the electromagnetic dynamics as it is shown in figure 5.11. It also has two outputs representing the real and imaginary part of the cavity voltage, to which the forward current $I_{fw}$ was added later on to allow the implementation of the detuning estimator.

As far as the mechanical aspect of the model is concerned, a transfer function is generated from the data obtained in section 5.2.2, by means of the vector fitting algorithm [34]. Originally, this transfer function had a single input and output, relating the input voltage to the piezo $V_{piezo}$ with the detuning generated in the cavity $\Delta\omega$, but in this case, two additional inputs were added to make the model more realistic. On the one hand an input for possible external disturbances $V_{pert}$ and on the other hand an input for Lorenz forces $V_{LF}$. To calculate the Lorentz forces acting on the cavity the following expression is used, $V_{LF} = k_0[(V_{cav}^r)^2 + (V_{cav}^i)^2]$ where $k_0$ is a scaling factor of order $10^{-13}$.

One of the main unknowns in controlling the mechanical vibrations of an elongated cavity such as the TESLA is based on the non collocated nature of the control problem. There are not enough studies so far to ensure that vibrations along the entire cavity geometry can be controlled by an actuator at one end of the cavity alone. Similarly, the exact effect of a mechanical disturbance affecting one point or another of the cavity is not known. In order to characterise this behaviour to some extent, the mechanical transfer function of the cavity has been altered so that each of the inputs ($V_{piezo}, V_{pert}$ and $V_{LF}$) affects the generated detuning slightly differently. For this purpose, the mechanical transfer function has been expressed by its state space representation and the input matrix $B_m = (b_1, b_2, \ldots, b_n)^T$ has been altered by adding two new columns.

$$B'_m = \begin{pmatrix} b_1 & -k_{pert}b_1 & k_{LF}b_1 \\ b_2 & -k_{pert}b_2 & k_{LF}b_2 \\ \vdots & \vdots & \vdots \\ b_n & -k_{pert}b_n & k_{LF}b_n \end{pmatrix} \tag{5.4}$$

where $\mathbf{k}_{pert}$ and $\mathbf{k}_{LF}$ are the gains affecting the perturbation and Lorenz forces inputs respectively. Note that in this case the different inputs are simply multiplied by a gain, but filters could also be applied to each input to enhance or minimise the effect of certain resonance modes depending on the input of the system. This would be a way to characterise more precisely the non-collocated nature of the control problem at hand, but it would require more detailed research that has not been carried out in this thesis.

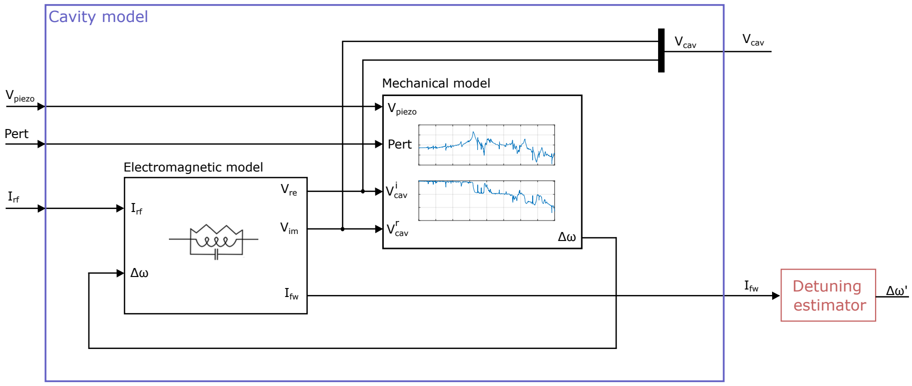

Figure 5.11.: Block diagram of the Simulink model.

Finally, a detuning estimator is used to obtain the detuning signal to perform the control. This device is capable of calculating an approximation of the detuning using the forward current $I_{fw}$, which is a signal that can be accessed in the real system.

### 5.4.2 | SIMULATION EXPERIMENT AND RESULTS

Using the simulink model described in the previous section, the MLADRC algorithm designed in chapter 5.3 has been tested.

Note that unlike in previous experiments, the electromagnetic dynamics of the cavity are present in this new model. Thus, before introducing the mechanical control loop, it is necessary to develop a LLRF system to keep the phase and amplitude of the electromagnetic field of the cavity stable. As this is not the focus of this thesis, the research literature has been used to implement a generic LLRF system. In this case, the work done in [93] was the foundation to design and implement the ADRC to control the electromagnetic dynamics of the cavity. The bandwidths of such controller are $f_o = 6000$Hz and $f_c = 100$Hz. Since in this case the delay is not a bounding factor, it has not been necessary to use the design and stabilisation techniques developed throughout this work.

As far as the detuning control is concerned, the MLADRC algorithm designed in chapter 5.3 has been implemented, which consists of a GESO with $f_o = 2000$Hz and $f_c = 170$Hz bandwidths and a notch filter centered at 170 Hz.

The implementation of the controller was carried out by mimicking a real digital implementation in order to study the effects of the discretization on the performance of the controller, as well as to have a first version that could be implemented on real hardware. Details on the implementation are set out in the following chapter. The resulting system is shown in figure 5.12.

To test the controller, a reference voltage is set for the cavity, and first, only the phase and amplitude control loop is activated. Then, a white noise signal is introduced through the input corresponding to the mechanical perturbations in order to study the detuning it generates.

This process is repeated again, with the MLADRC activated to analyse the detuning reduction achieved. Finally, to have data with which to compare the performance of the controller, the process is repeated using the PI controller presented in chapter 5.3. Figure 5.13 shows the results achieved in this experiment.

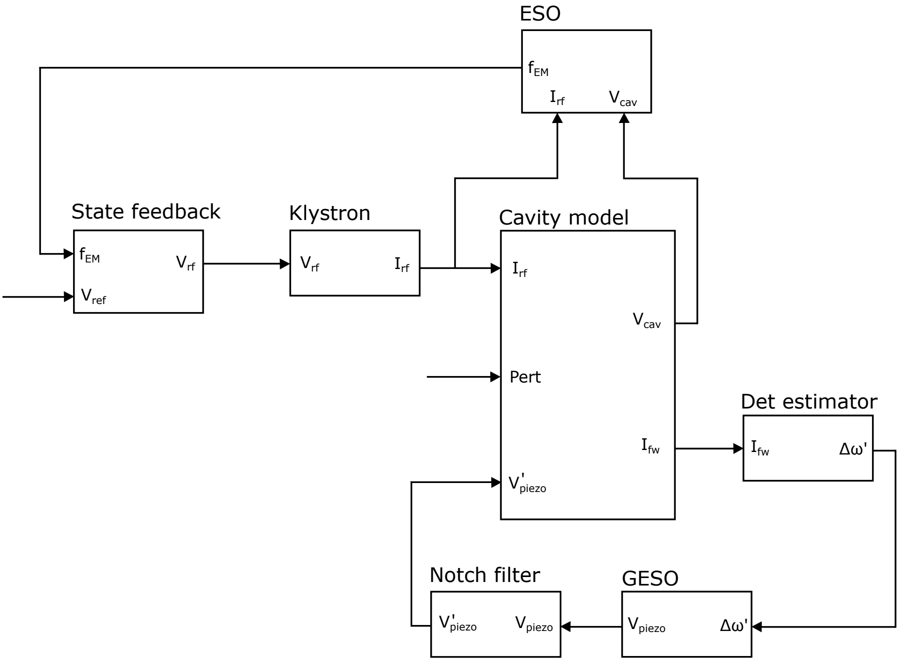

Figure 5.12.: Block diagram of the control structure used to control the cavity in Simulink.

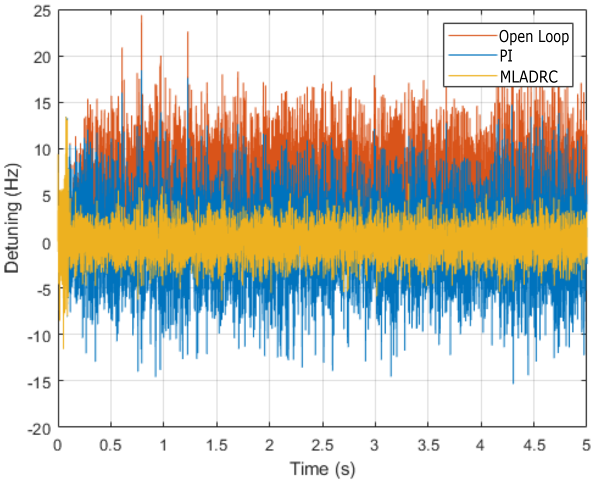

Figure 5.13.: Detuning generated in the cavity model by a white noise input. Three different cases are shown: When the detuning control is disabled (red), when detuning is controlled by a PI (blue) and when detuning is controlled by the MLADRC (yellow).

## 5.5 | IMPLEMENTATION AND DESIGN VALIDATION USING HARDWARE IN THE LOOP

Hardware in the Loop (HIL) testing is a simulation technique employed in the development and validation of complex control systems. At its core, HIL involves integrating a control system, referred to as the System Under Test (SUT), with a simulator or plant model that encapsulates the dynamic behavior of the physical system. It is worth mentioning that the virtual SRF cavity that was used as the plant model, was developed as a result of the collaboration between HZB and the University of the Basque Country [24].

The uniqueness of this simulator is that it is implemented on specific hardware that supports real-time execution, which ensures that the simulation occurs at the same rate as the actual system's dynamics. Other important aspect of the HIL technique is that the control algorithm can be implemented directly in the actual hardware intended to host the controller, giving the possibility to study and debug the digital implementation itself.

In summary, through this closed-loop operation, HIL testing provides a means to comprehensively evaluate the performance of a control system under conditions that closely mimic real-world scenarios. It allows for the testing of various scenarios, ranging from normal operation to extreme conditions and enables the testing of the actual digital implementation of the controller.

### 5.5.1 | HIL SYSTEM DESCRIPTION

National Instruments (NI) hardware was used to assemble the HIL system. On the one hand, the controller was implemented in a flexRIO device while the SRF cavity simulator was installed in a PCI eXtensions for Instrumentation (PXI) device. Both the controller and simulator were implemented on the FPGA of the respective devices, in order to ensure real time execution. More details on FPGAs are given in appendix C.1.

A PXI is a modular electronic platform that combines the high-speed capabilities of the PCI bus with specialized synchronization and triggering features. These devices typically consist of a chassis, a soft real-time controller, and various IO modules that can be configured to meet specific testing requirements.

For this particular case, in addition to the mandatory real-time controller, the PXI has been assembled using a re-configurable module, housing an FPGA, and a high-performance, high frequency analogue I/O module. For the technical characteristics of the system, please refer to Appendix C.3.

A flexRIO, in the other hand, is a re-configurable I/O module that combines FPGA processing hardware and a CPU running Linux real-time. Compared to the PXI, it is a slightly more restricted device in terms of customisation, as it only offers one input into which different I/O modules can be integrated. Even so, it is a highly flexible platform for developing high-speed and customizable measurement and control applications.

As in the previous case, a high frequency I/O analogue module is connected to the FPGA input of the flexRIO to generate and receive the RF signals required for the HIL system (See Appendix C.4 for technical information on the system). The layout of the experimental setup for the HIL system is shown in Figure 5.14.

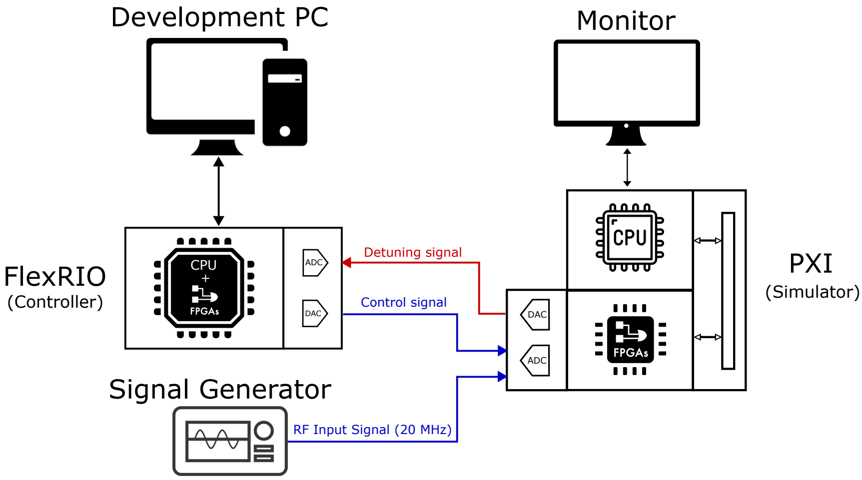

Figure 5.14.: Scheme of the setup used to create the HIL system.

As shown in chapter 5.4.1, the virtual cavity model includes both electromagnetic and mechanical dynamics. Thus, in order to perform simulations on it, it is necessary to feed it with an RF signal as it would happen in a real cavity. For that matter, a 20 MHz RF signal is used to simulate the cavity probe signal. The PXI, in which the simulator is housed, samples the RF signal four times per cycle (80MHz), which is known as IQ sampling. This sampling method allows the I/Q values of the signal to be obtained directly without the need for extra signal processing. This constant RF input generates in the mathematical model a voltage gradient inside the virtual cavity and a constant detuning resulting from the Lorentz forces. Note that for the sake of simplicity, no amplitude and phase control is applied.

The signal that will act as a mechanical disturbance, on the other hand, is generated in the CPU of the PXI, and is sent to the mathematical model housed in the FPGA through a Direct Memory Access (DMA) channel. This signal generates additional detuning on top of the existing detuning due to Lorentz Forces. The sum of all detuning is generated by I/O module with a generation speed of 100 MHz and is sent to the controller. The I/O module of the FlexRIO samples the detuning signal with a sampling rate of 100 MHz and feeds the discrete signal into the controller hosted in the FPGA. The controller computes the neccesary control signal and it sends it back in to the virtual cavity, closing the control loop.

The FlexRIO is connected via ethernet to a development PC on which the controller implementation has been designed and from which the performance of the controller can be monitored. Similarly, the PC housed in the PXI is connected to a computer screen in order to monitor the cavity parameters.

### 5.5.2 | DIGITAL IMPLEMENTATION AND VALIDATION

As mentioned above, the MLADRC controller has been implemented in the FPGA of a flexRIO. As shown in more detail in Appendix C.1, a FPGA is a re-programmable digital integrated circuit that enables the possibility to define and implement custom digital circuits on the go. Unlike traditional application-specific integrated circuits (ASICs), which are custom manufactured for specific design tasks, FPGAs can be programmed using a hardware description language (HDL) such as VHDL or Verilog, which allows the controller prototyping process to be fast and cost-effective. Note that such devices guarantee the execution of algorithms in hard real-time.

Although high-level languages can be used to define the operation of the circuit to be implemented, it is important to bear in mind that the final objective is to design and implement a real digital circuit. This means that in order to make an efficient design, it is important to take into account aspects of the implementation such as the type of data to be used, the distribution of the signals in the device itself to avoid timing violations and the necessary resolution for each signal. The following describes the process carried out to translate the MLADRC algorithm into a digital circuit and implement it on an FPGA.

In order to obtain the discrete representation of the controller, it is necessary to carry out a discretization process. To do so, first the execution time is set to 10 MHz, as this is a relatively slow speed to be carried out on an FPGA, but it also provides enough room to experiment with the bandwidth of the GESO.

One of the most crucial characteristics of a system when determining its stability is its phase. This is why it is of key importance to maintain the phase properties of the controller in the discretization process. To ensure that, the Tustin transform was used, since it preserves the relative stability of the system and is generally used when the phase response has to be preserved [96].

Thus, the implementation of the discrete GESO using its state space representation (5.5) is done first.

$$\begin{cases} \mathbf{x}[k+1] = \mathbf{A}_{gd}\mathbf{x}[k] + \mathbf{B}_{gd}\mathbf{u}[k] \\ y[k] = \mathbf{C}_{gd}\mathbf{x}[k] + \mathbf{D}_{gd}\mathbf{u}[k] \end{cases} \tag{5.5}$$

where $\mathbf{x}_k$ are the discrete states of the GESO and $y_k$ and $\mathbf{u}_k$ are the discrete output and input respectively. On the other hand, $\mathbf{A}_{gd}, \mathbf{B}_{gd}, \mathbf{C}_{gd}$ and $\mathbf{D}_{gd}$ are the matrices that define the dynamics of the discrete GESO and can be obtained by applying the Tustin transform to the continuous GESO. Figure 5.15 shows the structure used to implement equation (5.5), as well as the dimensions of the matrices for a second-order GESO, which is the one used for the control of the cavity.

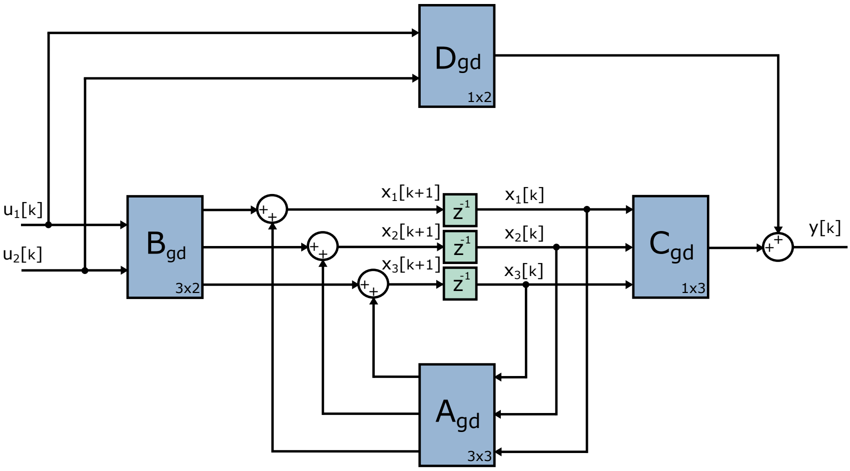

Figure 5.15.: Structure used to implement the second order GESO.

It is worth mentioning that the registers, represented by green blocks, are activated by a clock signal with a frequency identical to the execution time of the algorithm, 10 MHz. On the other hand, the blue blocks with the names of each GESO matrix represent a multiplication between a matrix and a vector that can be decomposed into simple additions and multiplications as shown in the equation (5.6).

$$\mathbf{A}\cdot\mathbf{x} = \begin{pmatrix} a_{11} & a_{12} & \cdots & a_{1n} \\ a_{21} & a_{22} & \cdots & a_{2n} \\ \vdots & \vdots & \ddots & \vdots \\ a_{m1} & a_{m2} & \cdots & a_{mn} \end{pmatrix} \cdot \begin{pmatrix} x_1 \\ x_2 \\ \vdots \\ x_n \end{pmatrix} = \begin{pmatrix} a_{11}x_1 + a_{12}x_2 + \cdots + a_{1n}x_n \\ a_{21}x_1 + a_{22}x_2 + \cdots + a_{2n}x_n \\ \vdots \\ a_{m1}x_1 + a_{m2}x_2 + \cdots + a_{mn}x_n \end{pmatrix} \tag{5.6}$$

Thus, to multiply a matrix of $n \times m$ dimension and a vector of $n$ dimension, it is necessary to perform $n \cdot m$ multiplications and $(n-1) \cdot m$ additions, that can be implemented by means of full adders and multiplier circuits. This allows us to get a preliminary idea of the resources needed for the implementation of the control algorithm. Table 5.1 shows the amount of multiplication and addition needed to perform each of the matricial multiplication for a second order GESO.

Table 5.1.: Number of additions and multiplications needed to implement for a second order GESO.

| | $\mathbf{A}_{gd}$ | $\mathbf{B}_{gd}$ | $\mathbf{C}_{gd}$ | $\mathbf{D}_{gd}$ | **Other** | **Total** |
|---|---|---|---|---|---|---|
| **Additions** | 6 | 3 | 2 | 1 | 4 | 16 |
| **Multiplications** | 9 | 6 | 3 | 2 | 0 | 20 |

As can be seen from the table, the GESO implementation is quite light on FPGA resources, as it is composed of a conservative number of simple arithmetic operations and 3 registers.

To implement the loop shaping compensator, a normalized discrete transfer function of order 2 has been integrated, such as the one shown in equation (5.7).

$$H_{lc}(z) = \frac{b_0 + b_1 z^{-1} + b_2 z^{-2}}{1 + a_1 z^{-1} + a_2 z^{-2}} \tag{5.7}$$

This function consists of two poles and two zeros with which to implement a wide variety of compensators such as notch filters, lead-lag compensators and so forth. The transfer function was implemented using its direct form, which is defined by the difference equation shown in (5.8).

$$y[k] = b_0 u[k] + b_1 u[k-1] + b_2 u[k-2] - a_1 y[k-1] - a_2 y[k-2] \tag{5.8}$$

where $u[k]$ is the discrete input to the loop shaping compensator and $y[k]$ is the discrete output. This equation can be implemented using the structure shown in figure 5.16.

Once the structures to be used in the implementation have been established,

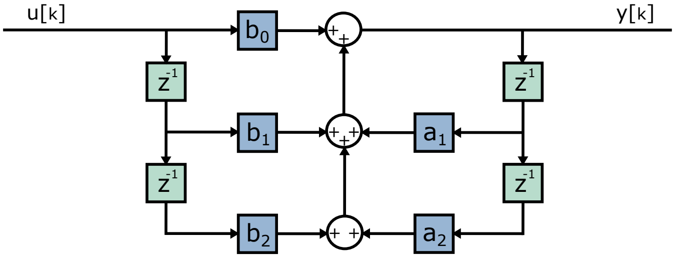

Figure 5.16.: Structure used to implement the Loop Shaping Compensator.

the format and word length of each internal signal of the circuit is determined, i.e. the number of bits with which each signal will be represented inside the circuit. The implementation also requires the compensation of internal delays, to avoid phase signal mismatches.

To do this, it should first of all be noted that most implementation in FPGA uses fixed-point mathematics, since it enables a much simpler implementation which is optimal for performance and power consumption. This means that for a successful implementation, it is necessary to know the dimension of each of the internal signals of the circuit, in order to assign them a format and word size suitable to represent the data to be transmitted by them. This is of particular importance in the case of fixed-point representation, since the number of bits representing the integer and fractional part of the data is fixed, unlike in floating-point mathematics.

So, before defining the fixed-point design, the algorithm was implemented in simulink following the real structure with which it would later be implemented in the FPGA (see figure 5.15 and 5.16). This allows us to simulate the controller under a wide variety of situations to determine the dimensions of each of the internal signals of the algorithm. Once this information is available, the word length to be used is defined and each signal is assigned a number of integer bits sufficient to represent the largest value that the signal has reached. It is worth mentioning that although the algorithm has been simulated under an extensive casuistry, it is possible that in reality there may be cases where the value of the signals exceeds the value measured in simulation. To manage this uncertainty and avoid overflows, the integer part of the data word has been given 3 more bits than necessary.

Initially, an 18-bit design was developed, with the idea of making the most of the FPGA's resources, as the device has 18-bit embedded adders and multipliers. In this way, it is possible to minimise the resources required for the implementation of the algorithm and improve routing and timing, while at the same time using the FPGA's embedded circuits, which generally offer higher performance.

When testing the implementation in Simulink, using Xilinx System Generator [43], it was observed that 18 bits is not a sufficient word length to implement the controller, as the system destabilises even with very conservative values for the controller. After analysing the problem, it was concluded that this is not due to possible overflows, but because the algorithm needs a minimum resolution in certain internal signals that could not be achieved with 18 bits.

Thus, work continued with the fixed-point implementation, and it was empirically concluded that the minimum word length to guarantee the stability of the controller, for this particular caser, is 24 bits. However, in order to have a greater margin of error and to take advantage of the FPGA's embedded adders and multipliers, a 36-bit design was developed. It is worth mentioning that although the device's embedded adders and multipliers are 18 bits, it can use two of them in conjunction to perform 36-bit additions and multiplications. It is also noteworthy that the fixed-point designs of the controller were carried out using both VHDL and Labview FPGA.

### 5.5.3 | HIL RESULTS

Experimentation with the HIL system served to validate the real-time performance of the MLADRC algorithm implementation, ensuring that non-linear dynamics such as those derived from Lorentz Forces do not introduce effects that could affect the stability of the system.

More importantly, it was also possible to test the implementation of the algorithm on the target hardware, which allowed to foresee the interface functionality that would be needed and to prematurely correct implementation errors such as overflows in different signals.

Regarding the actual detuning reduction achieved, it is not considered of great relevance, since the mathematical model of the virtual cavity differs from the real SRF cavity that will be used and the parameters of the model were not appropriately tuned. In this way, the obtained results were qualitative rather than quantitative. Even so, reductions of over 80% or the RMS detuning were achieved with respect to the open loop, when introducing white noise as a total disturbance.

## 5.6 | ALGORITHM TESTING IN THE REAL SRF TESLA CAVITY

Finally, the algorithm is implemented and tested on the real system, a 9-cell Tesla cavity in HoBiCaT.

### 5.6.1 | Control setup

As far as the control setup is concerned, the same measurement method described in the previous chapter 5.2.2 is used. In this case, the loop is closed by the mechanical control implemented in the FlexRIO device, so the master oscillator operates with the PLL loop opened and generating a constant driving signal of 1.3 GHz. The signal that is fed into the controller as a reference is the phase difference obtained by comparing the incident and transferred signal. Thus, technically, a phase control is performed, although the direct relationship between detuning and phase shift can be observed in equation (5.1). The control signal is amplified before driving the piezo-tuner, as it is depicted in Figure 5.17.

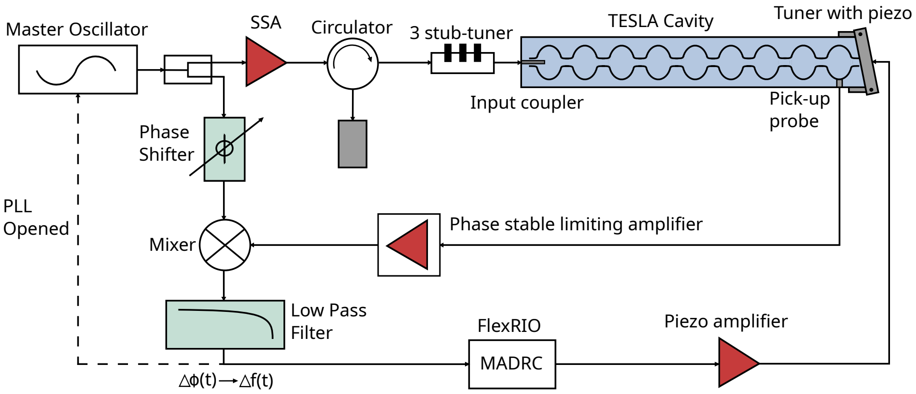

Figure 5.17.: Control setup used in HZB to compensate detuning of a TESLA cavity.

As has been described before, the implementation is done on the FPGA of a FlexRIO NI-7935R so there is enough execution speed to set the observers bandwidth high enough to experiments with different controller configurations. In this way, the controller is implemented with an execution rate of 10 MHz. In addition, a NI-5783 IO module is used, which provides an acquisition/generation speed of 100 MHz and a full-scale output range of 2V peak to peak. Considering that the piezo-amplifier has a gain of 20, the dynamic range of the control signal is $\pm 20V$, which constitutes $20\%$ of the operational range of the piezo-tuner.

### 5.6.2 | Experimental results

For this experiment, the input coupler and the three stub-tuner were arranged so that the $Q_L$ of the cavity was fixed at $10^7$. The cavity was fed by a $400W$ driving signal generating a field gradient of $4MV/m$. Then, by means of one of the piezo actuators, a frequency constant mechanical disturbance of $11.4Hz$

was introduced in order to replicate possible perturbations that the cavity may suffer during its operation in a machine, and to have a known disturbance on which to measure the reduction obtained by our controller, in adddition to other stochatics disturbances present in the system.

Following the design method described in section 4.2.1, first, the bandwidths of both the observer and the controller are determined. Taking as a starting point the values obtained in the theoretical section 5.3 and taking into account the possible discrepancies between the transfer function (Figure 5.6) and the real system, different MLADRCs are tested in order to find the optimal controller to which the loop shaping compensator will be applied later. The bandwidth of the observer was fixed at $2000Hz$ and different controller bandwidths were tested, obtaining the results shown in figure 5.18. The gain of all controllers were adjusted to provide the greatest reduction of disturbances while ensuring system stability. Table 1 shows the most relevant parameters results for each controller.

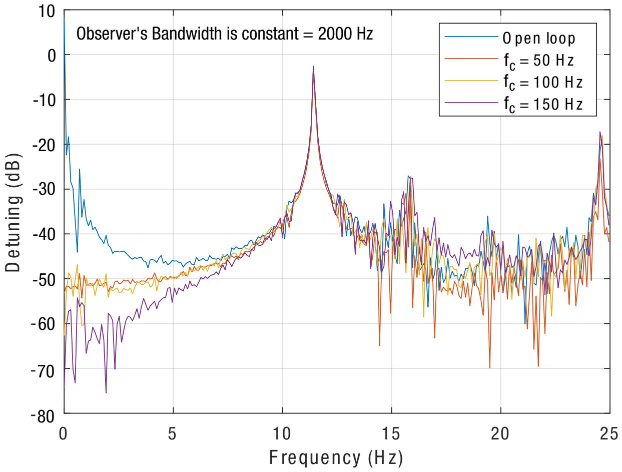

Figure 5.18.: Frequency spectrum of the measured detuning of the TESLA cavity by using different controller bandwidths. A constant perturbation of 11.4 Hz is being fed into the system.

Table 5.2.: Measured detuning and bandwidth for different controllers.

| | **Gain** ($10^{-4}$) | **RMS (Hz)** | **Bandwidth (Hz)** |
|---|---|---|---|
| **Open loop** | – | 2.2857 | – |
| $\omega_c$= **50 Hz** | 8.866 | 0.9005 | 5 |
| $\omega_c$ = **100 Hz** | 1.067 | 1.0699 | 5 |
| $\omega_c$ = **150 Hz** | 0.605 | 1.0628 | 7 |

As can be seen from both figure 5.18 and the results in table 5.2, all three controllers have very low bandwidth since the gain is limited by the stability of the system. Even so, they are able to control the static detuning and reduce the dynamic detuning by, at least, half in a bandwidth of around 5 Hz.

The next step, which consists of stabilizing the controller by loop shaping, is performed with the controller with $\omega_c$=150, since it is the one that best reduces disturbances at low frequencies and has the widest effective bandwidth. Thus, following the methodology described in 4.2.1, the controller gain is increased until the system destabilizes. This happens with a $G = 6.6 \cdot 10^{-4}$ generating an oscillation of 164 Hz, which is very similar to what was predicted in the analysis of the simulations. In order to stabilize the system, a notch filter centered in 164 Hz is implemented, so the gain of the controller in that frequency is drastically decreased mantaining the performance in the rest of the bandwidth. The notch filter is represented by the following equation:

$$H_{notch} = \frac{s^2 + 1061811}{s^2 + 1030s + 1061811} \tag{5.9}$$

Once the system was stabilized, is was possible to further increase the controller gain to a value of $77 \cdot 10^{-4}$, more than an order of magnitude higher. This resulted in a bandwidth of approximately 30 Hz, 25 Hz more than what was achieved without loop shaping. In addition, the fixed 11.4 Hz resonance was reduced by 11 dB, which in linear is equivalent to a factor of 4. Figure 5.19 shows the detuning measured for different controller gains and figure 5.20 illustrates in more detail the reduction achieved on the disturbance generated by the secondary piezo-tuner at 11.4 Hz.

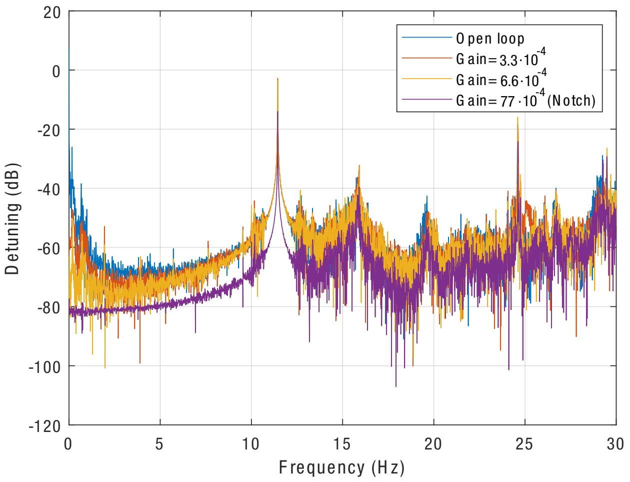

Figure 5.19.: Frequency spectrum of the measured detuning of the TESLA cavity for different controller gains. The parameters of the controller are $\omega_e = 2000Hz$ and $\omega_c = 150Hz$. A constant perturbation of 11.4 Hz is being fed into the system.

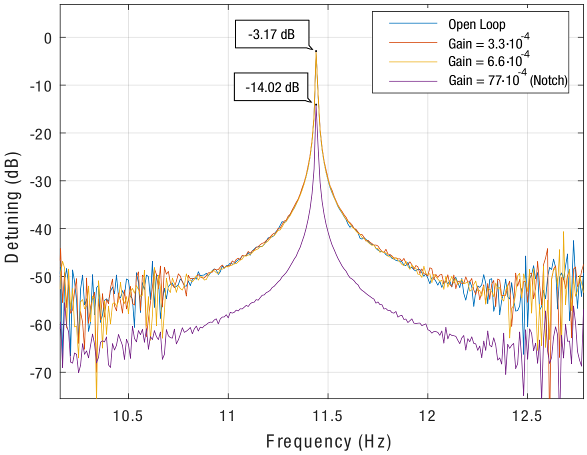

Figure 5.20.: Zoom in of the measured detuning of the TESLA cavity for different controller gains. The parameters of the controller are $\omega_e = 2000Hz$ and $\omega_c = 150Hz$. A constant perturbation of 11.4 Hz is being fed into the system.

In order to better appreciate the bandwidth of the controller, and the effect it has on the different mechanical resonance modes of the cavity, figure 5.21 shows the integrated detuning spectra.

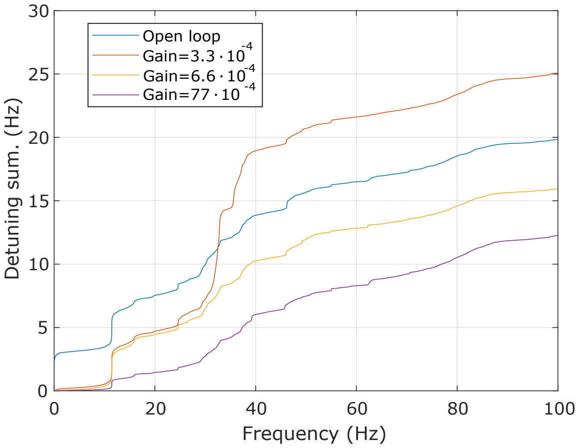

Figure 5.21.: Integrated detuning spectra of the TESLA cavity for different controller gains. The parameters of the controller are $\omega_e = 2000Hz$ and $\omega_c = 150Hz$. A constant perturbation of 11.4 Hz is being fed into the system.

Note that the bandwidth and performance of the controller increases with gain. The same conclusions are obtained if the data is represented on a time scale. Figure 5.22 clearly shows the DC correction and the improvement of the detuning RMS the larger the gain. Table 5.3 shows the most representative results for this controller.

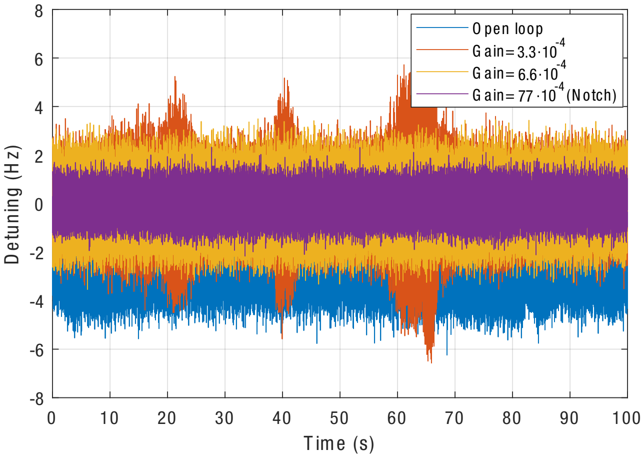

Figure 5.22.: Measured detuning of the TESLA cavity for different controller gains. The parameters of the controller are $\omega_e = 2000Hz$ and $\omega_c = 150Hz$. A constant perturbation of 11.4 Hz is being fed into the system.

Table 5.3.: Measured detuning and bandwidth for different gains with the same controller ($\omega_e = 2000Hz$ and $\omega_c = 150Hz$).

| **Gain($10^{-4}$)** | **Peak value(Hz)** | **RMS(Hz)** | **Bandwidth(Hz)** |
|---|---|---|---|
| Open loop | 6.2424 | 2.5877 | — |
| 3.3 | 7.2179 | 1.4824 | 3 |
| 6.6 | 3.5389 | 1.2264 | 7 |
| 77 | 2.3252 | 0.5297 | 29 |

Thus, the feasibility of the MLADRC algorithm and the proposed design method is evident. As shown in table 5.3, the MLADRC adjusted by loop shaping techniques is able to reduce the detuning (RMS) by a factor of 5 with respect to the open loop. Furthermore, it is evident that the controller's performance is significantly reduced when the stabilization step by loop shaping is absent. This is due to the lower relative stability, which prohibits increasing the gain without destabilizing the system, leading to a performance degradation of more than 60%. It is worth mentioning that experiments have been performed with different values of $Q_L$ and disturbance frequencies, varying from $10^7$ to $5 \cdot 10^7$ and from 5 Hz to 20 Hz respectively and the result has been very similar.

CHAPTER 6

# SUMMARY AND CONCLUSION

This work begins with a brief introduction to particle accelerators. Many of these machines are immense facilities not only in size and complexity, but also in terms of energy consumption. In the current context of climate change and soaring energy prices, current and future facilities need to tackle their efficiency to ensure their viability. The pursuit of efficient high-gradient RF structures and systems stands as one of the five critical domains identified by the European Strategy for forthcoming facilities, needing continued research and development efforts.

One of the approaches being taken to increase the efficiency of accelerating structures and reduce energy consumption is the use of high $Q_L$. When the quality factors are optimized, the power consumption required to attain a specific level of accelerating field diminishes, resulting in a reduction in RF cost and the possibility of using solid state amplifiers, which are cheaper and more versatile than klystrons.

The problem with such high $Q_L$ is that it makes the bandwidth of the cavities extremely narrow, making them very sensitive to external mechanical disturbances, known as microphonics. Thus, the aim of this thesis has been to develop a controller that provides advantages over the algorithms used to date to control the detuning generated by these microphonics.

The first step was to study the problem of detuning in depth, making use of the literature on the subject. To this end, the main characteristics and operating principles of SRF cavities were reviewed, with a special focus on TESLA cavities. By analysing the equivalent $RLC$ circuit with which the electromagnetic dynamics of a cavity can be represented, many important conclusions can be derived. On the one hand, by studying the steady-state behaviour of the cavity, the relationship between detuning and the amplitude and phase of the cavity voltage can be identified, which analytically shows how detrimental detuning is to the stability of the cavity field. This study is of particular relevance to this work as it shows that when the detuning is sufficiently small with respect to the cavity bandwidth, it can be calculated by the phase difference between the cavity field and the incident current. On the other hand, by analysing the transient behaviour of the cavity field, the simplified mathematical model to describe the electromagnetic dynamics of the cavity can be derived.

After presenting the main sources of detuning in a TESLA cavity, the power required to maintain a constant acceleration gradient in a CW-operating cavity was analysed as a function of beam loading and detuning. From this study, it can be found that when there is high beam loading, for energy consumption reasons, the loaded quality factor and the accelerating gradient must be kept at relatively low values, thus reducing the effect of detuning on the field. On the other hand, in applications where beam loading is negligible, it is possible to increase $Q_L$ to values of the order of $10^7$, thus obtaining high energy efficiencies. In these cases, as the cavity bandwidth is reduced to a few hundred Hz, the field stability becomes much more sensitive to detuning. Thus, in applications with low beam loading, reducing the peak detuning of the cavity translates in the possibility of increasing the loaded quality factor and in conclusion, increasing the energy efficiency of the machine.

After carrying out a study of the state of the art of microphonics control, the ADRC algorithm was presented, which is the controller used as the foundation for the development of the MLADRC throughout this thesis.

As described in chapter 3, the ADRC is a feedback control algorithm that bases its operation on the compensation of any unwanted dynamics by estimating the so-called total disturbance. For this purpose, an ESO that contains information on the desired dynamics is defined. This control element is able to estimate the difference between the real and desired dynamics (the total disturbance) and then feed it back into the system to cancel the undesired dynamics.

Based on the mechanical characteristics of an SRF cavity, it was determined that the ADRC is a strong candidate to control detuning in such systems, as it offers great performance in controlling non-linear systems and is especially good at rejecting disturbances. Moreover, it is an easy-to-implement algorithm that requires little preliminary information about the system to be controlled, which makes it especially useful in the case of large accelerators where a large number of different cavities have to be controlled.

However, due to the high gain obtained in the ESO bandwidth, the ADRC algorithm is very sensitive to the presence of time delay, specially when controlling mechanical systems like an SRF cavity. As could be seen in the stability study conducted in section 3.2, this is largely due to the fact that systems with mechanical resonances often have frequency ranges where the phase of their frequency response is very close to -180 degrees. Moreover, since the time delay adds a shift in the phase response of the system, which grows linearly with frequency, it is relatively easy for the controller to generate a phase crossover frequency. Since the gain provided by the ESO is extremely large for the entire ESO bandwidth, the open-loop system gain at that phase crossover frequency is usually greater than 0 dB, thus destabilising the system.

Studying the state of the art of the ADRC for time delayed systems, it was observed that most of the modifications designed to improve the stability of the algorithm in the face of time delay, also negatively affected its performance when it came to rejecting external disturbances. Thus, a new modification was developed, the MLADRC, with the aim of increasing the stability of the ADRC in the face of time delay, while maintaining the performance of the controller.

In this way, the MLADRC is studied in depth in chapter 4. This new modification of the ADRC has two main differences with respect to the original algorithm. On the one hand, in order to study the open-loop response of the system more easily, the state feedback control was integrated into the ESO itself, giving rise to the so-called GESO. This modification allows the study of the stability of the system by means of both the Bode and Nyquist diagrams of the open-loop system and it assures the matching condition of the ADRC algorithm. On the other hand, and as a complement to the GESO, a loop shaping compensator is introduced in the controller's direct chain. The purpose of this control element is to alter the frequency response of the system in the frequency ranges most likely to destabilise the system. In this way, by altering the phase and amplitude of the open-loop system, it is possible to increase the relative stability of the closed-loop system without affecting the performance of the controller.

One of the main objectives in developing the MLADRC algorithm was to make it a straightforward controller that is both simple to design and easy to implement. To this end, a straightforward design method was developed in section 4.2.1 to create MLADRC controllers without the need of having a great amount of information about the system to be controlled nor to be an expert in the field. This provides a simple step by step guide for engineers around the world to perform preliminary tests of the algorithm on their own systems.

Before applying the controller to a real cavity, both the design methodology and its operation was validated on a resonant mechanical system. First, an ADRC was applied to the system and to validate the design and stabilisation method, a time delay was applied by software large enough to destabilise the system. Then, the ADRC was exchanged for the MLADRC modification and the system was stabilised using loop shaping techniques. This stabilisation process was carried out in two different ways. On the one hand, the information provided by the approximate transfer function of the system was used, and a lead filter was developed as a loop shaping compensator. In this way, the system was stabilised and a performance similar to that of the ADRC with the system not delayed was achieved. On the other hand, the stabilisation process was repeated, this time without resorting to the information previously available about the system. To do this, the control signal was measured empirically when the system was in an unstable regime, and a notch filter centred on the oscillation frequency of the destabilised control signal was implemented as a loop shaping compensator. This method performed somewhat worse, but still achieved better performance than a well-adjusted PI.

Thus it was demonstrated that the stabilisation and design method of the MLADRC works, despite not knowing the dynamics of the system to be controlled. Furthermore, it could be observed that the MLADRC keeps the performance of the original ADRC almost intact, providing it with greater resistance to time delay. Finally, the superior performance of the MLADRC over a more conventional controller such as the PI could also be observed on a real system.

The next step was to test the MLADRC algorithm in a real SRF cavity. For that matter, a 9-cell TESLA cavity equipped with a Saclay-II tuner was used, which is located in the HoBiCaT test bench at the Helmholtz-Zentrum Berlin. This process was carried out in three different phases, which are described in the chapter 5.

In the first phase, an ad hoc MLADRC was designed for the cavity in question. To this end, a process of identification and parametrization of the mechanical dynamics of the cavity was first carried out, resulting in the mechanical transfer function of the system. The most relevant feature of this transfer function was the important resonance mode at 160 Hz, which causes the phase of the system around this frequency to approach -180 degrees. This gives the system an extremely low relative stability.

Based on the measured transfer function, a well tuned MLADRC was designed and proven in simulation in chapter 5.3. On the one hand, it was shown that the MLADRC algorithm in itself offers better performance than the most commonly used PI, since it offers greater reduction of disturbances in a wider bandwidth (see Figure 5.10). The feasibility of the stabilization system based on loop shaping was also demonstrated. By providing the system with greater relative stability through the implementation of filters, it has been possible to increase the gain of the controller, increasing at the same time its performance and bandwidth.

In the next phase, the fixed-point design of the algorithm was carried out and implemented on the FPGA of a flexRIO device. To carry out the debugging process of the implementation and to test the performance of the controller in a somewhat more realistic environment, a HIL system was developed. The results obtained were satisfactory, and the last step of the process was proceeded with.

In section 5.6.2, both the MLADRC algorithm and the design methodology were experimentally validated in the SRF cavity. Through trial and error, it was determined that the optimum parameters for the controller were $\omega_c$=150 Hz and $\omega_e$=2000 Hz, which is in agreement with the results obtained in simulation. The relationship between the controller gain and its performance was also demonstrated, since as shown in figure 5.19, the higher the gain parameter, the greater the bandwidth and detuning reduction. Finally, the validity of our stabilization method using loop shaping was demonstrated. By implementing a notch filter centered at 164 Hz, not only were the theoretical results matched, but they were significantly improved. An RMS of 0.5 Hz was achieved, 50% lower than that obtained in simulation, along with a bandwidth of 29 Hz.

From all this it was concluded that the MLADRC algorithm is a strong candidate for the control of low frequency stochastic microphonics. It is easy to implement and design, and does not require too much prior information about the system to be controlled. In that sense, it shares many of the benefits and strengths of classical PID controllers, but with better overall performance.

Compared to the classic ADRC, the alternative MLADRC structure offers two important advantages. On the one hand, it allows to analyze the open-loop frequency response more easily, facilitating the stabilization process. On the other hand, it is designed in such way that the matching condition is always met regardless of the controller gain. This allows the gain to be used to bring the system to its stability limit, which later allows a stabilization filter to be designed with relative ease.

It is also worth mentioning that due to the ease of design and implementation of the MLADRC, it is possible to automatize the controller design process for almost any cavity. This is of particular interest for installations where a large number of SRF cavities are to be controlled.

Finally, it should be noted that this is a feedback controller with the objective of controlling low frequency stochastic microphonics such as those derived from the pressure fluctuations of liquid helium. For future projects, it is planned to implement this feedback algorithm in conjunction with a feed forward algorithm that can handle constant-frequency detuning events, such as those that can occur due to rotating machinery like vacuum pumps. This would provide a controller operating in different bandwidths capable of suppressing low-frequency stochastic disturbances and higher frequency constant disturbances, thus obtaining a state-of-the-art detuning control system for SRF cavities.

It is also interesting to explore the possibilities that FE-FRT actuators may offer in the future, since, as discussed in section 2.6, the lack of mechanical parts enables them to offer much faster responses. This greatly benefits the MLADRC algorithm since, as has been shown throughout this thesis, its most limiting factor is the delay of the system to be controlled, i.e. the delay of the actuators.

# LIST OF PUBLICATIONS

Let us list the publications we have produced as a result of the research described in this thesis, in reverse chronological order, from most recent to oldest.

## Publications

[1] Elejaga, A., Jugo, J., & Echevarria, P. (2019a). Control algorithm tests using a virtual cw srf cavity. *arXiv preprint arXiv:1910.06227*.

[2] Elejaga, A., Jugo, J., & Echevarria, P. (2019b). Mikrofonien monitorizazio eta kontrola rf kabitateetan. *Ikergazte2019*.

[3] Elejaga, A., Jugo, J., & Echevarria, P. (2023a). Partikulen azeleragailuetan mikrofoniak kontrolatzeari buruzko oinarrizko kontzeptuak: Madrc algoritmoa. *Ikergazte2023*.

[4] Elejaga, A., Jugo, J., Echevarria, P., Neumann, A., & Ushakov, A. (2023b). Initial esperimental test of a modified adrc algorithm for microphonics reduction. *14th International Particle Accelerator Conference (IPAC)*.

[5] Elejaga, A., Jugo, J., Echevarria, P., Neumann, A., Ushakov, A., & Knobloch, J. (Under review). Experimental testing of a modified active disturbance rejection control for microphonics reduction in a 9-cell tesla superconducting cavity. *Physical Review Accelerators and Beams*.

[6] Jugo, J., Elejaga, A., & Echevarria, P. (2023). Modified active disturbance rejection control scheme for systems with time delay. *IET Control Theory & Applications*, 17(14), 1992–2003.

# APPENDIX A

# CYLINDRICAL CAVITIES AND THE $TM_{0n0}$ RESONANCE MODES

In this appendix the electromagnetic fields generated in a cylindrical cavity are summarized, as it can be found in the bibliography. This type of geometry is commonly used for non-superconducting cavities and through its study many of the characteristics of the fields generated in SRF elliptical cavities can be inferred. In addition to this, only the so-called $TM_{0n0}$ resonance modes are reviewed, since they have characteristics well suited for accelerating charged particles and are the most commonly used modes for this purpose.

One of the major advantages of these modes, for cylindrical cavities, is that they do not generate a magnetic component in the direction of wave propagation, i.e. the entire magnetic field is in the transverse plane and has no portion parallel to the length axis. This means that when charged particles pass through the cavity along its longitudinal axis, their trajectory is not altered by the magnetic field. At the same time, this kind of resonant modes generate longitudinal electric fields with a maximum value at the center of the cavity, which is especially useful for the acceleration of charged particles.

When working with cylindrical structures, the sub-indexes that classify the resonant modes refer to cylindrical coordinates. In the case of $TM_{0n0}$ modes, indexes indicate that the magnetic component has zero variation in the radial direction (0), $n$ full cycle variations in the azimuthal direction (n), and zero variation in the axial direction (0).

The following study is synthesised from the book *Principles of Charged Particle Acceleration* [41], more specifically from Chapter 12, *Resonant Cavities and Waveguides*, accesible in [70]. It is also worth mentioning that certain topics studied in this section such as resistivity and eddy current penetration are not directly applicable to SRF cavities. These differences become apparent when SRF cavities are discussed further in section 2.2.

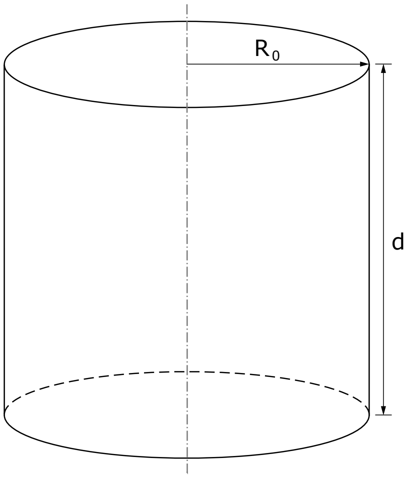

Figure A.1.: Geometry of a generic cylindrical resonant cavity.

Taking as reference the resonant cavity shown in Figure A.1, being $R_0$ its radius and $d$ its length, the electromagnetic field generated when exciting a $TM_{0n0}$ mode is calculated [27]. To do so, the Maxwell equations are used as a starting point:

$$\nabla \times \bar{E} + \frac{\partial \bar{B}}{\partial t} = 0 \tag{A.1}$$

$$\nabla \cdot \bar{E} = 0 \tag{A.2}$$

$$\nabla \times \bar{B} - \epsilon\mu \frac{\partial \bar{E}}{\partial t} = 0 \tag{A.3}$$

$$\nabla \cdot \bar{B} = 0 \tag{A.4}$$

By applying the vector identity $\nabla \times (\nabla \times \bar{A}) = \nabla(\nabla \cdot \bar{A}) - \nabla^2 \bar{A}$, Equations (A.1) and (A.4) can be rewritten as follows:

$$\nabla^2 \bar{E} - \frac{1}{v^2}\frac{\partial^2 \bar{E}}{\partial t^2} = 0 \tag{A.5}$$

$$\nabla^2 \bar{B} - \frac{1}{v^2}\frac{\partial^2 \bar{B}}{\partial t^2} = 0 \tag{A.6}$$

where $v$ is the speed of light in the the medium inside the cavity:

$$v = c\sqrt{\frac{\epsilon_0 \mu_0}{\epsilon \mu}} \tag{A.7}$$

By solving wave equation (A.5) it is possible to calculate the electric field related to the resonance modes $TM_{0n0}$. To do so, it is necessary to apply the appropriate boundary conditions [21] in cylindrical coordinates:

I. The $TM_{0n0}$ modes have azimuthal symmetry: $\frac{\partial}{\partial \theta} = 0$

II. The electric field along the z-axis is constant: $\frac{\partial \bar{E}}{\partial z} = 0$

III. The only component of the electric field is longitudinal: $E_r = 0$ and $E_\theta = 0$

IV. The electromagnetic field varies over time with an $\omega$ frequency. $e^{j\omega t}$

These last two conditions imply that the electric field has the following form:

$$\bar{E} = E_z(r)e^{j\omega t}\hat{z} \tag{A.8}$$

Using the cylindrical coordinate form of the Laplacian operator and applying the aforementioned boundary conditions on equation (A.5), it is obtained that the $TM_{0n0}$ resonance modes satisfy the following wave equation:

$$\frac{d^2 E_z(r)}{dr^2} + \frac{1}{r}\frac{dE_z(r)}{dr} + \frac{\omega^2}{v^2}E_z(r) = 0 \tag{A.9}$$

As can be seen, equation (A.9) is a particular case ($\alpha$=0) of the Bessel equation, whereby the solution can be expressed in terms of the zero-order Bessel functions $J_0(k_n r)$ and $Y_0(k_n r)$ [22]. In this case, the function $Y_0(k_n r)$ is eliminated because the electric field to be found has a finite value on the z-axis. Thus, the electric field taking part in the $TM_{0n0}$ resonance modes has the following form:

$$E_{zn}(r,t) = E_{0n}J_0(k_n r)e^{j\omega_n t} \tag{A.10}$$

where $E_{0n}$ is the magnitude of the electric field of the $TM_{0n0}$ mode over the z-axis, $\omega_n$ is the resonance frequency in rad/s and $k_n$ is the resonance wave number, which is defined as $k_n = \omega_n/c$, being $c$ the speed of light in the medium.

Another boundary condition, is that the electric field parallel to the cavity wall at $r = R_0$ has to be zero. This means that $E_{zn}(R_0, t) = 0$. Thus it follows that the only valid values of $k_n$ are those that make the function $J_0(k_nR_0)$ zero. Table A.1 shows these values for the first 4 modes:

Table A.1.: Values of $k_n$ and $\omega_n$ for the first four $TM_{0n0}$ modes [18].

| Mode | $k_n$ | $\omega_n$ |
|---|---|---|
| $TM_{010}$ | 2.405/$R_0$ | 2.405/$\sqrt{\mu\epsilon}R_0$ |
| $TM_{020}$ | 5.520/$R_0$ | 5.520/$\sqrt{\mu\epsilon}R_0$ |
| $TM_{030}$ | 8.654/$R_0$ | 8.654/$\sqrt{\mu\epsilon}R_0$ |
| $TM_{040}$ | 11.792/$R_0$ | 11.792/$\sqrt{\mu\epsilon}R_0$ |

To calculate the magnetic field associated to the electric field, it is sufficient to substitute the expression A.10 in equation (A.1), obtaining the following:

$$-jvk_nB_{\theta n} = E_{0n}\frac{d(J_0(k_nr))}{dr}e^{j\omega_nt} \tag{A.11}$$

Rewriting the equation, it is found that the resultant magnetic field in the $TM_{0n0}$ modes is the following.

$$B_{\theta n}(r,t) = -j\frac{\sqrt{\mu\epsilon}E_{0n}}{k_n}J_1(k_nr)e^{j\omega_nt} \tag{A.12}$$

Thus, looking at equation (A.10) it can be concluded that the electric field generated when a $TM_{0n0}$ mode is excited is longitudinal and only dependent on the radius. Similarly, looking at equation (A.12), it can be extracted that the associated magnetic field is azimuthal and also solely dependent on the radius. Furthermore, substituting the corresponding Bessel functions in each of the above equations, it is observed that the electric field is maximum on the z-axis, while the magnetic field is zero. This fact is very appropriate for accelerating charged particles, since on the one hand they obtain the maximum acceleration when passing through the z-axis, and on the other hand, they are not deflected since the magnetic field on the z-axis is zero and there is no transversal electric field.

Taking the $TM_{010}$ mode for simplicity, the electromagnetic field created in the cavity takes the form shown in Figure A.2.

Similarly, the normalized magnitude of both the electric and magnetic field as a function of radial position is shown in the graph in Figure A.3.

As can be seen in Figure A.3, the electric field is maximum on the z-axis while it decays almost linearly as it approaches the cavity wall (r=$R_0$). In the case of the magnetic field, its value is zero on the axis while it increases as it moves

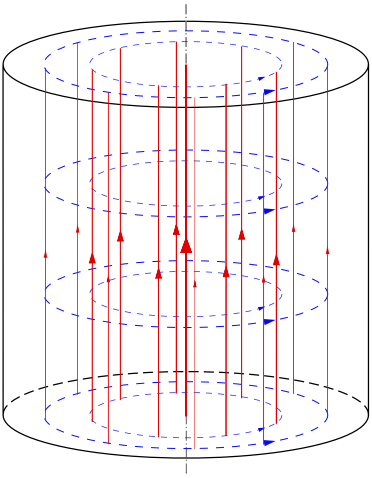

Figure A.2.: Scheme of the electromagnetic fields generated when exciting a $TM_{010}$ mode in a cylindrical cavity. The electric field is represented in red while the magnetic field is represented in blue.

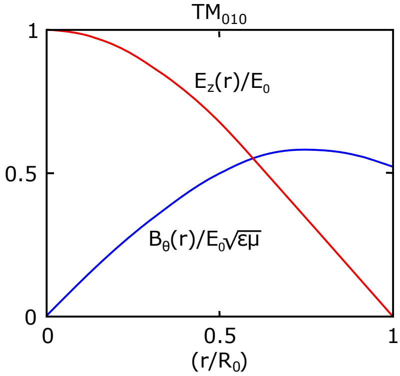

Figure A.3.: Normalized magnitude of axial electric field and azimuthal magnetic field as a function of radial position.

away from the center of the cavity, reaching its maximum around $0.8 r/R_0$ and decreasing again as it continues to approach the cavity wall.

With regard to the resonant frequency of each $TM_{0n0}$ mode, given that $\omega_n = v k_n$ and that the valid $k_n$ are those that take the function $J_0(k_n r)$ to 0 when $r = R_0$, the following expression is obtained:

$$\omega_n = \frac{X_{0n}}{\sqrt{\mu\epsilon} R_0} \tag{A.13}$$

$X_{0n}$ being the $n^{th}$ zero of the zero-order Bessel function, $J_0(x)$. Note that the resonance frequency of a cylindrical cavity is exclusively dependent on the characteristics of the medium ($\mu\epsilon$), which is assumed to be constant, and its radius ($R_0$). The value of $\omega_n$ for the first 4 modes is shown in Table A.1.

The total amplitude of the electromagnetic fields generated inside the cavity, on the other hand, is completely dependent on the amplitude of the injected RF wave, and on the effectiveness with which the cavity stores the energy of that wave, up to a limit. This efficiency is represented by the quality factor $Q_0$ of the device, which is defined as the ratio between the energy stored $E_{st}$ in the cavity and the energy dissipated $E_{diss}$ in each half oscillation cycle:

$$Q_0 = \pi \frac{E_{st}}{E_{diss}} \tag{A.14}$$

Alternatively, this factor can also be defined as the ratio between the resonant frequency $f_0$ of the resonant mode and its bandwidth $f_{BW}$ [18].

$$Q_0 = \frac{f_0}{f_{BW}} \tag{A.15}$$

Thus, the more energy the device dissipates, the worse its quality factor will be, and therefore, the lower the electromagnetic fields generated inside it, with the consequent loss of acceleration capability. On the other hand, the higher the quality factor, the better its efficiency in storing energy, although its bandwidth will be narrower and, as will be discussed in following sections, it will be more sensitive to disturbances.

As a general rule, resonant cavities are designed with the objective of obtaining the highest possible quality factor. For this purpose, materials with very high conductivity such as copper, aluminum and, in particular cases, superconducting materials such as niobium [23] are used in their construction. Even so, due to the large electromagnetic fields generated inside the cavity, large induced currents appear on the walls of the device, making the loss of energy due to resistivity very noticeable. These currents penetrate the cavity walls at a distance determined by the surface depth $\delta$ [16].

$$\delta = \sqrt{\frac{2\rho}{\omega\mu}[\sqrt{1+(\rho\omega\epsilon)^2}+\rho\omega\epsilon]} \tag{A.16}$$

Being $\rho$ the conductivity of the material, $\mu$ and $\epsilon$ the magnetic permeability and permittivity of the material respectively and $\omega$ the angular frequency of the induced current. As it is shown in equation (A.16), the surface depth is determined by the frequency of the current and the characteristics of the conductive material.

Similarly, the current density $J_s$ induced in the walls of a cylindrical cavity is given by the following equation.

$$J_s = B_\theta(r,t)/\mu_0 \tag{A.17}$$

In this way, the current density induced in the cavity walls is dependent on the azimuthal magnetic field of each point of the wall, so that the energy losses due to resistive effects are also dependent on this field. As has already been proven throughout this section, the magnetic field varies depending on the resonance mode being excited, so it can be concluded that each resonance mode is associated with a different induced current, and in conclusion, a different energy loss due to resistive effects. This shows that the cavity quality factor Q is dependent on both the cavity characteristics and the resonance mode being excited. As an example, equation (A.18) shows the quality factor of a cylindrical cavity for its $TM_{010}$ resonance mode.

$$Q_{TM_{010}} = \frac{d/\delta}{1 + d/R_0} \tag{A.18}$$

It is important to note that when the beam of particles passes through the cavity, there is a possibility of indirectly exciting undesired higher-order modes due to wakefield effects [61]. As a consequence, the resultant electromagnetic field becomes a superposition of the electromagnetic fields produced by each individual resonance mode. The contribution of these unwanted modes, as a general rule, is detrimental to the correct acceleration of the particles, since the electromagnetic fields they generate do not have the correct characteristics. Thus, all energy derived to make the cavity resonate in these modes is lost and the Q factor of the device is degraded.

Throughout this section, certain conclusions have been obtained that will be of great help for the development of the work. the most relevant ones are listed below.

I. In the case of cylindrical cavities, the most commonly used resonance modes for particle acceleration are the so-called $TM_{0n0}$. This is because, as shown in figure A.2, they provide electromagnetic fields with a very particular arrangement. On the one hand, the electric field is only axial (see equation (A.10)), and maximum in the center of the cavity, which allows maximizing the energy transfer to the particles. On the other hand, the magnetic field is azimuthal and zero in the cavity axis (see equation (A.12)), which decreases particle scattering.

II. The resonant frequency of each mode is defined solely by the medium and the geometry of the cavity (see equation (A.13)). Considering that the cavities operate in ultra high vacuum (UHV), it can be assumed that the medium is constant so that the resonant frequency is strictly dependent on the geometry of the cavity. This is an important fact when it comes to understanding the problem of detuning.

III. The quality factor of a resonant cavity refers to its efficiency in storing energy and is inversely proportional to its bandwidth. As shown in equation (A.18), the quality factor of a cavity is not only defined by its physical characteristics (geometry and material), but also by the characteristics of the resonant mode that is excited. Thus, it is important that the cavity has an appropriate design to avoid, or at least reduce, the excitation of unwanted high-order modes (HOM). This is usually accomplished with HOM filters, which are designed to selectively absorb and dissipate energy from these undesired modes, effectively damping their effects and preventing them from interfering with the accelerator's operation.

# APPENDIX B

# RELEVANT CHARACTERISTICS OF ELLIPTICAL SRF CAVITIES

## B.1 | SURFACE RESISTANCE

The primary advantage of utilizing superconducting cavities resides in their remarkably low surface resistance, measuring around 10 nΩ at 2 K. While normal conducting cavities exhibit typical quality factors ranging from $10^4$ to $10^5$, SRF cavities can surpass $10^{10}$, thereby reducing RF losses by a significant margin of 5 to 6 orders of magnitude. Despite the reduced efficiency of refrigeration, substantial savings in primary electric power are achieved.

That being said, it should be pointed out that, unlike the DC case, superconductors are not free from energy dissipation in microwave fields. This phenomenon stems from the penetration of the RF magnetic field into a thin surface layer, which induces oscillatory behaviors among the non-bound electrons, those that do not form Cooper pairs. The quantity of these "free electrons," experiences an exponential reduction in relation to temperature. According to the Bardeen-Cooper-Schrieffer (BCS) theory of superconductivity, the surface resistance within the domain of temperatures less than half the critical temperature ($T_c/2$) can be mathematically expressed as follows in the case of niobium:

$$R_{BCS} \propto \frac{\omega^2}{T} e^{-1.76T_c/T} \tag{B.1}$$

For niobium the BCS surface resistance at 1.3 GHz amounts to about 800 nΩ at 4.2K and drops to 15 nΩ at 2K. In TESLA-like bulk Nb cavities, the exponential temperature dependence is the reason why operation at 1.8–2K is essential for achieving high accelerating gradients in combination with very high quality factors.

In addition to the BCS term there is a residual resistance $R_{res}$ that is independent from the temperature. It is caused by impurities in the superconductor material and trapped magnetic flux. Niobium is in principle a superconductor without flux pinning, but in practice, weak magnetic DC fields are not expelled upon cooldown and remain trapped in the material. Those flux lines contain a normal-conducting core whose area is roughly $\pi\epsilon_0^2$. The coherence length $\epsilon_0$, which refers to the distance over which a wave maintains a relatively constant phase relationship, is of about 40 nm in Nb. In this way, trapped magnetic DC flux results in a surface resistance described by the following expression [10].

$$R_{mag} = (B_{ext}/2B_{c2})R_n \tag{B.2}$$

Where $B_{ext}$ is the externally applied field, $B_{c2}$ the upper critical field and $R_n$ the surface resistance of the conductor in the normal state. When operating at a frequency of 1.3 GHz, the surface resistance incurred due to entrapped magnetic flux totals 3.5 $n\Omega/\mu T$ for niobium. Consequently, cavities that lack proper shielding against the Earth's magnetic field are constrained to $Q_0$ values below $10^9$.

## B.2 | LIMITATIONS

The intrinsic limitation of a superconducting resonator is dictated by the necessity to maintain the RF magnetic field at the inner surface below the "superheating field" of the superconductor, which typically ranges from 200 to 240 mT for niobium [92]. For the TESLA cavities, this constraint imposes a maximum attainable accelerating field of 50-60 MV/m. While, in theory, the quality factor should remain constant, as this fundamental superconductor limit is approached, other effects often result in the "excitation curve" $Q_0 = Q_0(E_{acc})$ reaching noticeably lower values. Frequently, this is accompanied by a significant decline in $Q_0$ as the cavity's highest gradient is approached. The main factors contributing to this degradation in performance encompass excessive heating at impurities on the inner surface, the emission of electrons due to field effects, and multipacting. Multipacting is an abbreviation for "multiple impacting" and refers to a resonant process, where the number of unwanted electrons resulting from a parasitic discharge rapidly grows to a larger value at some specific locations in a radio-frequency cavity, which, in the case of SRF devices, can lead to quenching of superconductivity [76].

This phenomenon is closely related to another basic limitation of the maximum field in a superconducting cavity, which is referred as thermal instability. The dissipation of energy due to RF losses exhibits non-uniform characteristics across the entire surface of the cavity. Specific regions tend to manifest larger temperature raises, occasionally surpassing the critical temperature of the superconductor, which is referred as quenching. Consequently, these regions undergo a transition to a normal-conducting state, leading to notably intensified power dissipation. Given the exponential increase of surface resistance with temperature, this scenario can potentially trigger an uncontrollable escalation, culminating in a complete quenching of the entire cavity. As a typical number, the diameter of a normal-conducting spot must exceed 50 $\mu m$ to be able to initiate a thermal instability at 25 MV/m for niobium.

Lastly, field emission of electrons from sharp tips is the most severe limitation in high-gradient superconducting cavities. In field-emission loaded cavities the quality factor drops exponentially above a certain threshold, and X-rays are observed. There is experimental evidence that small particles on the cavity surface, such us dust or fibers, act as field emitters. As a result, meticulous cleaning procedures, such as high-pressure water rinsing, stand out as the most effective measure to counteract field emission. Figure B.1 shows a typical stainless steel particulate that was collected from a CEBAF-type 5-cell niobium SRF cavity after service for beam operation.

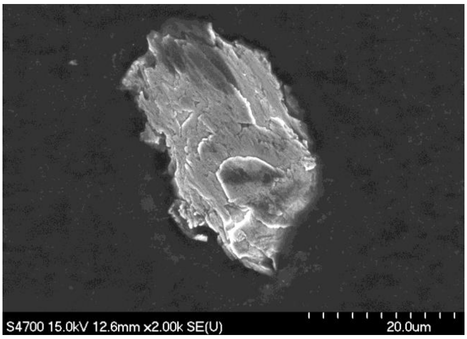

Figure B.1.: stainless steel particulate that was collected from a CEBAF-type 5-cell niobium SRF cavity [32].

All this limitations are discussed to a greater extent in the book by Padamsee, Knobloch and Hayes [72], *Rf superconductivity for accelerators.*

## B.3 | CRITERIA FOR ELLIPTICAL CAVITY DESIGN

Unlike in normal conducting cavities and due to the low surface resistance of superconductive materials, issues of high shunt impedance are of minor importance. This is why SRF cavities are designed with other objectives in mind, such as obtaining low-surface electromagnetic fields or avoiding electron multipacting effects. This results in larger iris openings and a rounded shape. Figure B.2 shows an inner elliptical cell and its shape parameters which are used to trim the RF properties according to given criteria for an specific application.

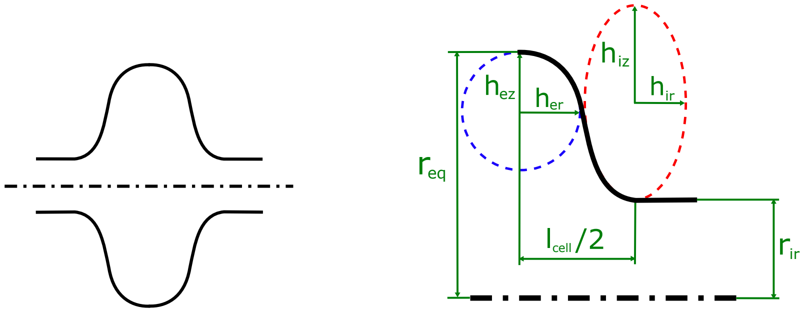

Figure B.2.: Cross section of an elliptical cell. The figure on the right depicts the seven parameters that are used to design the cell.

$h_{ez}$, $h_{er}$ and $h_{iz}$, $h_{ir}$ are the half axis of the ellipses defining the curvature of the equator and iris of the cell respectively. Similarly, $r_{eq}$ and $r_{ir}$ are the radius of the equator and iris of the cell while $l_{cell}$ is the length of the cell.

It should be noted that not all geometric parameters can be freely chosen. On the one hand, $l_{cell}$ has to be adjusted to the speed of accelerating particles $v$, since the maximum energy gain takes place for $l_{cell} = v/2c$, which provides synchronic acceleration of the beam along the multi-cell structure [82]. On the other hand, the radius of the cell $r_{eq}$ must be trimmed to adjust the frequency of the accelerating mode, which is a final step in the design process. In this way, optimization of the geometry of the inner cell, for a given application of a multi-cell accelerating structure, has to be performed with proper adjustment of the remaining five geometric parameters. This usually leads to conflicts in the optimization process and results in the need to adopt certain compromises in the design.

There are three criteria very often used for the inner-cell design, directly related to applications of accelerating structures:

When operating with high gradients, the aim is to ensure that the ratio of peak magnetic field to accelerating gradient is minimized. This is achieved by altering the curvature of the iris and equator of the cell, as well as by reducing the iris radius.

When cryogenic losses are to be minimised, the dissipation factor is sought to be maximised, which is a factor that depends on the geometry of the cavity and the characteristic impedance of the beam and is used as a measure for energy dissipation in the cavity wall. This is usually achieved by reducing the radius of the iris and altering the shape of the equator.

Lastly, when operating with high beam loading the aim is to design the cell so that the Wakefield effects excite as few HOMs as possible. This is normally done by increasing the radius of the iris. As an example, Figure B.3 shows 3 prototype cells that were proposed for the International Linear Collider (ILC) [64].

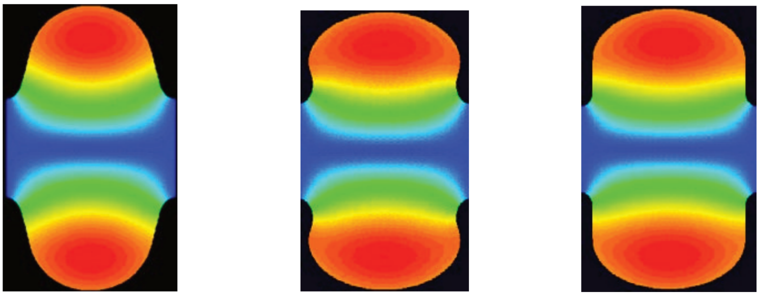

Figure B.3.: Three inner cells proposed for ILC: original TESLA shape (left), RE shape (middle), LL shape (right) [82].

The TESLA inner cell, shown in the left of Figure B.3 is one of the most used geometry in modern SRF cavities. It was designed in the 1990s with the objective of achieving exceptionally high accelerating gradients, ideally reaching 44.5MV/m. In the years 2002 and 2004, two geometries of inner cell with better ratio of peak magnetic field to accelerating gradient where proposed; the Low Loss (LL) and the Re-entrant (RE), with an achievable maximum gradient of 52 MV/m and 51 MV/m for the RE and LL shapes respectively. The disadvantage of those new shapes were higher HOM loss factors and bigger multipackting effects due to the difficulty of properly cleaning those more complicated geometries.

## B.4 | HIGHER-ORDER MODES AND COUPLERS

When traversing an accelerating cavity, a particle beam excites a broad spectrum of higher modes, depending on the geometric shunt impedances ($R_{sh}/Q_0$) of those modes. The resulting electromagnetic field left behind by the beam is called the wakefield. As such, the beam's movement can deposit a noteworthy amount of energy into high impedance, Higher-Order Modes (HOMs). Unless adequately extracted and damped, these HOMs can also induce longitudinal beam instabilities and increase the beam's energy spread, or even cause a total beam loss.

The main functions of HOM couplers are to remove the beam-induced power in the monopole HOMs and to damp the dangerous monopole and dipole modes to avoid energy spread, beam emittance degradation, and beam blow-up after multiple beam passages. Figure B.4 shows the main systems for decoupling HOMs from the accelerating field.

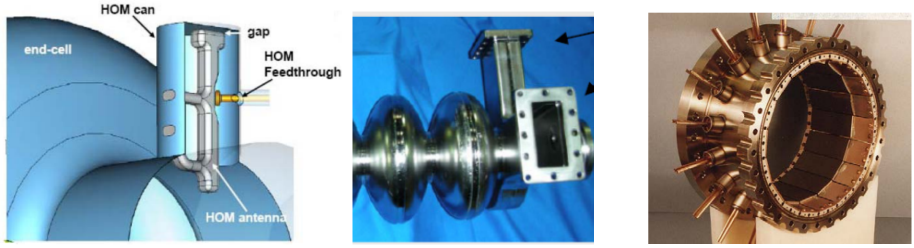

(a) (b) (c)

Figure B.4.: Different types of HOM couplers. (a) The antenna/loop based TESLA HOM coupler [71]. (b) Waveguide HOM coupler examples for the Cornell/CEBAF cavity. (c) Beam-pipe absorbers lined with ferrite [8].

APPENDIX C

# HARDWARE USED FOR THE IMPLEMENTATION

## C.1 | FIELD PROGRAMMABLE GATE ARRAYS

A FPGA is a re-programmable digital integrated circuit composed of configurable logic blocks (CLBs) and input/output ports (IOBs) (see Figure C.1), whose interconnection and functionality can be programmed using a hardware description language (HDL) such as VHDL or Verilog. Unlike traditional application-specific integrated circuits (ASICs), which are custom manufactured for specific design tasks, FPGAs enable the possibility to define and implement custom digital circuits on the go, maintaining most of the performance advantages of ASICs.

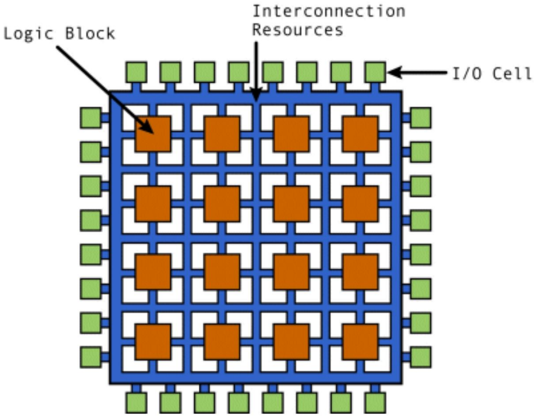

Figure C.1.: Simplified structure of an FPGA.

The CLB is the fundamental building block of FPGA technology, which, in general, consists of the combination of a number of logic cells like the one shown in Figure C.2.

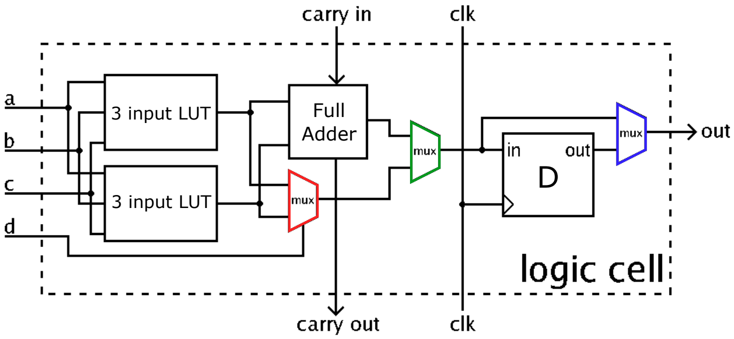

Figure C.2.: Simplified structure of a logic cell.

The main components of a typical logic cell are a 4-input Look Up Table (LUT) where logic functions can be programmed, a full adder (FA), and a D-type flip-flop. Note that in Figure C.2, the LUT is spitted in two 3-input LUTs. This is because, when configured in normal mode, both LUTs are combined into a 4-input LUT through the multiplexer depicted in red. Instead, when the cell is configured in arithmetic mode their outputs are fed to the FA. That configuration is dictated by the multiplexer depicted in green. Lastly, the output can be either synchronous or asynchronous, depending on the programming of the multiplexer depicted in blue.

Another important feature of FPGAs are the re-programmable interconnections. In essence, they consist of switch boxes, like the one shown in Figure C.3, arranged at the intersections of the interconnections between CBLs.

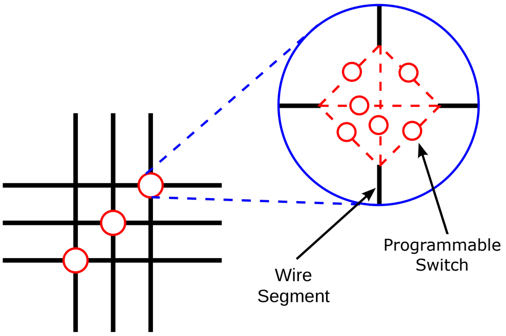

Figure C.3.: Simplified structure of a switch box.

Whenever a vertical and a horizontal channel intersect, a switch box is present. In the most typical architecture, when a wire enters a switch box, there are three programmable switches that enable it to connect to three other wires in adjacent channel segments. In this switch box topology, a wire in track number one connects only to wires in track number one in adjacent channel segments, wires in track number 2 connect only to other wires in track number 2 and so on.

In summary, these elements allow the configuration of interconnections between the CBLs, generating the routing of the signals of the integrated circuit in the FPGA. It must be mentioned that FPGAs contain dedicated global and regional routing networks for clock and reset signals so they can be delivered with minimal skew.

Modern FPGA families include the most basic and widely used functionalities, such as addition and multiplication, directly embedded in silicon. The so-called digital signal processing (DSP) blocks implement specific support for common fixed-point and floating-point arithmetic, which reduces the need to build equivalent logic from general-purpose CBLs and greatly increase the performance of the device.

## C.2 | MyRIO-9000

The myRIO-1900 card from National Instruments is a portable reconfigurable I/O (RIO) device that provides analogue input (AI), analogue output (AO), digital input and output (DIO), audio and power output in a compact integrated device. It can be connected to a development computer via USB connector or via wifi. Figure C.4 shows a picture of the device and a schematic of all its input and output ports.

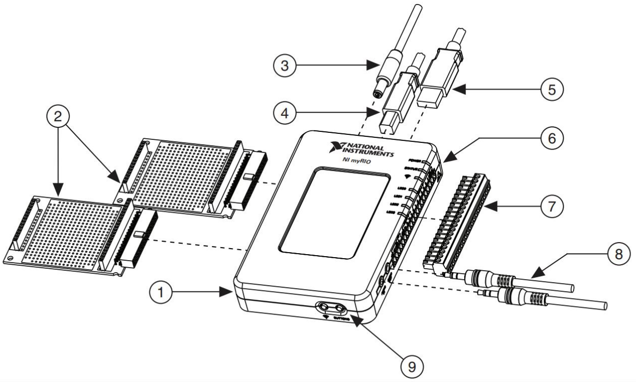

| | |
|---|---|
| 1 | NI myRIO-1900 |
| 2 | myRIO Expansion Port (MXP) Breakouts (One Included in Kit) |
| 3 | Power Input Cable |
| 4 | USB Device Cable |
| 5 | USB Host Cable (Not Included in Kit) |
| 6 | LEDs |
| 7 | Mini System Port (MSP) Screw-Terminal Connector |
| 8 | Audio In/Out Cables (One Included in Kit) |
| 9 | Button0 |

Figure C.4.: Schematic of the NI myRIO-1900 and its connection ports [48].

It is powered by a dual-core Xilinx Z-7010 microprocessor with 667 MHz processing speed, running a Linux Realtime operating system, which offers soft real time processing capabilities. It also features a Xilinx Z-7010 FPGA working in conjunction with the microprocessor which offers hard real time processing. Figure C.5 shows the full disposition of the different parts of the myRIO-9000.

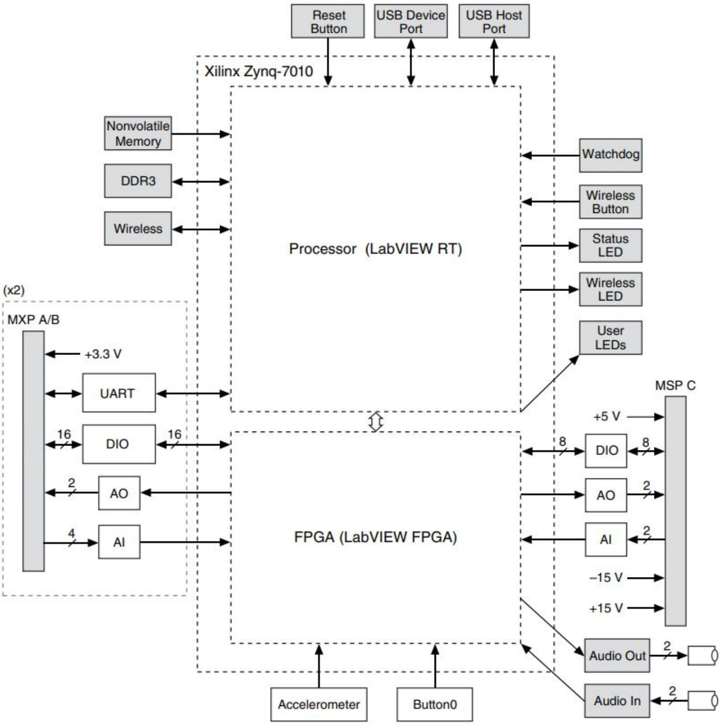

Figure C.5.: NI myRIO-1900 Hardware Block Diagram [48].

As for the myRIO's input and output terminals, the device has two myRIO Expansion Ports (MXP), to which breakout cards can be added, and a Mini System Port (MSP), to which a connection terminal can be screwed (see Figure C.4). Both types of ports have both analogue and digital IOs of different characteristics, as well as communication buses based on UART protocol.

All the analogue inputs are multiplexed to a single analog-to-digital converter (ADC) with an aggregated sample rate of 500 KS/s and a resolution of 12 bits. Each MXP port has 4 single ended AI channels with a nominal range going from 0 to 5 V. In the case of the MSP port, only two AI channels with a nominal range of ±10 V are available.

Each analogue output channel has a dedicated digital-to-analog converter (DAC) with a maximum update rate of 345 KS/s and a resolution of 12 bits, so they can all update simultaneously. The DACs for the analog output channels are controlled by two serial communication buses from the FPGA. MXP connectors share one bus, and the MSP connector and the audio outputs share a second bus. Each MXP port has 4 single ended AO channels with a nominal range going from 0 to 5 V and a current drive of 3 mA. In the case of the MSP port, only two AI channels are available, with a nominal range of $\pm 10$ V and a current drive of 2 mA.

Note that in this appendix only the most relevant characteristics of the device for the experiments carried out throughout the thesis have been described. For further technical information, please refer to [48].

## C.3 | PXI SYSTEM

The PXI is a device designed as a modular instrumentation platform for applications in test and measurement. At its core is the PXI chassis, which serves as a physical enclosure that houses key components called PXI modules (See Figure C.6). Inside the chassis there is a back plane, a printed circuit board that forms the communication backbone, that enables the flow of data and control signals between different PXI modules, which are the functional units of the system.

Figure C.6.: Example of a PXI system.

These modules are varied and can encompass signal generators, real-time CPUs, FPGA modules, digital I/O devices, RF analyzers, and more. When inserted into the PXI chassis, these modules are automatically recognized and configured by the system. The chassis may also include special slots for timing modules, which are responsible for generating and distributing the clock signals necessary for the synchronisation of all the different modules in the device.

In this way, PXIs are very versatile devices that can be assembled using the most appropriate modules to provide the desired functionality.

The chassis used for this work is the NI PXIe-1082, which, as shown in Figure C.7, has one slot for the controller, two peripheral slots with PCIe input, one slot for a timing module and four hybrid peripheral slots with PCI/PCIe input.

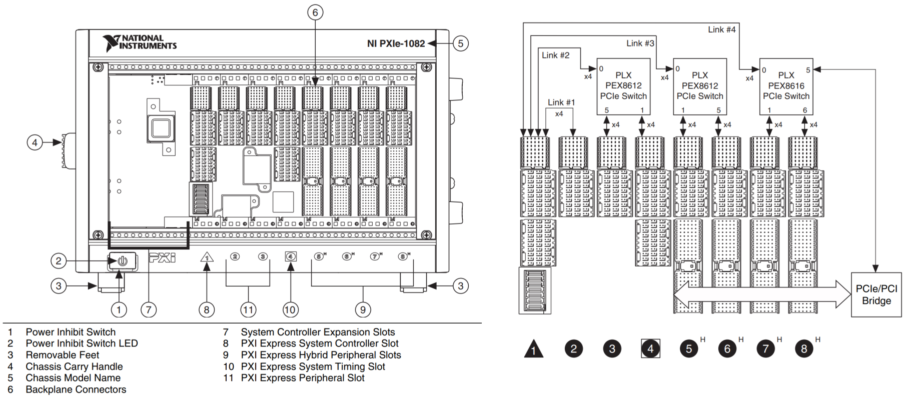

Figure C.7.: Schematic showing the most relevant features of the NI PXIe-1082 chassis. The figure on the left shows the most relevant components on the front of the device, as well as the different inputs. The figure on the right shows the interconnections between the different inputs of the device [49].

In the first slot of the chassis an NI PXIe-8135 module is connected [50], which is a system controller based on an embedded computer that has a quad-core Intel Core i7-3610QE processor, dual channel DDR3, 1600 MHz memory controller, all the standard I/O, and an integrated hard drive.

The PXI controller runs the software that controls and directs the specific functions of each module in the system. It handles module configuration, task synchronisation, and communication with other devices or systems.

A re-configurable NI PXIe-7966R module is installed in one of the PCIe peripheral slots, which has a Virtex-5 SX95T FPGA with 640 DSP slices and 40MHz default time-base [47].

For signal acquisition and generation, an analog input/output module NI 5781 is added to the input of the FPGA module. This adapter has two analog input channels with a fixed input range of 2 $V_{pk-pk}$ when operating in differential mode and 1 $V_{pk-pk}$ in single ended mode. It has a sample rate that can range from 10 MHz to 100 MHz and features an analog to digital converter (ADC) with 14-bit resolution. Similarly, it has two analog output channels with 2 $V_{pk-pk}$ output range when working in differential mode and 1 $V_{pk-pk}$ in single ended mode. The data generation rate ranges from 10 MHz to 100 MHz, but for this device, can be increased to 400 MHz by means of interpolation. Finally, the digital to analog converter (DAC) has a resolution of 16 bits [45].

The card also has a CLK IN input to introduce an external clock signal and a CLK OUT output to generate an internal clock signal.

## C.4 | FLEXRIO SYSTEM

FlexRIO is a technology platform developed by NI for designing and implementing custom hardware-accelerated systems. It consists of a CPU running a real-time operating system, and an FPGA on which to implement logic circuits. Figure C.8 shows the device itself and some possible IO modules.

Figure C.8.: FlexRIO device with an IO module mounted and different IO module options.

The device used in this work is a FlexRIO 7935R [46], which has a Kintex-7 XC7K410T FPGA with 1540 DSP48 slices and a default time-base of 40 MHz. As far as the processor is concerned, it consists of a Xilinx Zynq-7020 dual core running a 32-bit NI Linux Real-Time OS, which is embedded together with the FPGA on a single chip, thus creating a system on chip (SoC) device.

Since the signals used in SRF cavities are in the radio frequency range, it is necessary to implement an analogical input and output module to the FlexRIO to carry out the signal acquisition and generation process. The device chosen for that matter was the NI 5783 Analog Adapter Module [44], which has 4 analog input channels, 4 analog output channels and a clock input to serve as an external clock reference, among others.

The 4 analog inputs are single-ended with a fixed input range of 2.03 $V_{pk-pk}$ and a sampling rate that can range between 60 to 100 MHz. Each analog input features an ADC with 16-bit resolution. Similarly, the 4 analog outputs are single ended with a 16-bit resolution DAC and an output range of 1.001 $V_{pk-pk}$.

# BIBLIOGRAPHY

[1] M. Abo-Bakr, W. Anders, A. Büchel, K. Bürkmann-Gehrlein, A. Bundels, Y. Bergmann, P. Echevarria, A. Frahm, H.W. Glock, F. Glöckner, et al. Status report of the Berlin Energy Recovery Linac project BERLinPro. In *IPAC 2018: Proceedings of the 9th International Particle Accelerator Conference*, pages 4127–4130, 2018.

[2] C. Adolphsen, D. Angal-Kalinin, T. Arndt, M. Arnold, R. Assmann, B. Auchmann, K. Aulenbacher, A. Ballarino, B. Baudouy, P. Baudrenghien, et al. European strategy for particle physics–accelerator R&D roadmap. *arXiv preprint arXiv:2201.07895*, 2022.

[3] K. J. Åström and R. M. Murray. *Feedback systems: an introduction for scientists and engineers.* Princeton university press, 2021.

[4] B. Aune, R. Bandelmann, D. Bloess, B. Bonin ande A. Bosotti, M. Champion, C. Crawford, G. Deppe, B. Dwersteg, D.A. Edwards, et al. Superconducting TESLA cavities. *Physical Review special topics-accelerators and beams*, 3(9):092001, 2000.

[5] B. Baklakov, T. Bolshakov, A. Chupyra, A. Erokhin, P. Lebedev, V. Parkhomchuk, Sh. Singatulin, J. Lach, and V. Shiltsev. Ground vibration measurements for Fermilab future collider projects. *Physical Review Special Topics-Accelerators and Beams*, 1(3):031001, 1998.

[6] A. Bellandi, V. Ayvazyan, J. Branlard, C. Gümüs, S. Pfeiffer, K. Przygoda, and R. Rybaniec. LLRF R&D towards CW operation of the european XFEL. In *Proc*, 2018.

[7] A. Bellandi, J. Branlard, J. Diaz, S. Aderhold, A. Benwell, A. Brachmann, S. Hoobler, A. Ratti, D. Gonnella, J. Nelson, et al. Narrow bandwidth active noise control for microphonics rejection in superconducting cavities at LCLS-II. *arXiv preprint arXiv:2209.13896*, 2022.

[8] S. Belomestnykh, W. Hartung, J. Kirchgessner, D. Moffat, H. Muller, H. Padamsee, and V. Veshcherevich. Comparison of the predicted and measured loss factor of the superconducting cavity assembly for the CESR upgrade. In *Proceedings Particle Accelerator Conference*, volume 5, pages 3394–3396. IEEE, 1995.

[9] R. Bitter, T. Mohiuddin, and M. Nawrocki. *LabVIEW: Advanced programming techniques.* Crc Press, 2006.

[10] B. Bonin. CERN accelerator school superconductivity in particle accelerators, CERN 96-03, 1995.

[11] B. Bosotti, C. Pagani, R. Paparella, and N. Panzeri. The coaxial blade tuner–final report and evaluation of operation. Technical report, CARE, 2008.

[12] R. Brinkmann and TESLA Collaboration. The TESLA superconducting linear collider. In *AIP Conference Proceedings*, volume 397, pages 173–189. American Institute of Physics, 1997.

[13] A. Büchner, F. Gabriel, E. Grosse, P. Michel, W. Seidel, and J. Voigtländer. The ELBE-project at Dresden-Rossendorf. *EPAC'00, Vienna, June*, 2000.

[14] L.A. Castañeda, A. Luviano-Juárez, G. Ochoa-Ortega, and I. Chairez. Tracking control of uncertain time delay systems: An ADRC approach. *Control Engineering Practice*, 78:97–104, 2018.

[15] W. K. Chen. *The electrical engineering handbook.* Elsevier, 2004.

[16] G. Ciovati. *Investigation of the superconducting properties of niobium radio-frequency cavities.* Old Dominion University, 2005.

[17] P. Clay, JP. Desvard, R. Duthil, J. Gastebois, G. Grygiel, U. Knopf, R. Lange, F. Lejars, C. Mayri, P. Pailler, et al. Cryogenic and electrical test cryostat for instrumented superconductive RF cavities (chechia). *Advances in Cryogenic Engineering: Part A*, pages 905–910, 1996.

[18] R. E. Collin. *Waveguides and Cavities*, pages 329–410. Wiley-IEEE Press, 1991.

[19] Z. Conway and M. Liepe. Fast piezoelectric actuator control of microphonics in the CW cornell ERL injector cryomodule. *Proc. PAC'09*, pages 918–920, 2009.

[20] J. A. Cuenca. *Characterisation of powders using microwave cavity perturbation.* PhD thesis, Cardiff University, 2015.

[21] E. Daly. Overview of existing tuner systems. In *SRF2005*, Ithaca, NY, 2005.

[22] J.R. Delayen. Ponderomotive instabilities and microphonics: a tutorial. *Physica C: Superconductivity*, 441(1-2):1–6, 2006.

[23] G. Devanz, B. Visentin, M. Desmons, M. Luong, E. Jacques, M. Fouaidy, and P. Bosland. Active compensation of Lorentz force detuning of a TTF 9-cell cavity in CRYHOLAB. In *Proceedings of LINAC*, 2006.

[24] P. Echevarria, E. Aldekoa, J. Jugo, A. Neumann, A. Ushakov, and J. Knobloch. Superconducting radio-frequency virtual cavity for control algorithms debugging. *Review of Scientific Instruments*, 89(8), 2018.

[25] L. J Eshelman and J. D. Schaffer. Real-coded genetic algorithms and interval-schemata. In *Foundations of genetic algorithms*, volume 2, pages 187–202. Elsevier, 1993.

[26] Y. Feng, Z. Li, S. Rakheja, and H. Jiang. A modified prandtl-ishlinskii hysteresis modeling method with load-dependent delay for characterizing magnetostrictive actuated systems. *Mechanical Sciences*, 9:177–188, 04 2018.

[27] R. P. Feynman, R. B. Leighton, and Matthew Sands. *The Feynman lectures on physics; New millennium ed.* Basic Books, New York, NY, 2010. Originally published 1963-1965.

[28] L. B. Freidovich and H. K. Khalil. Performance recovery of feedback-linearization-based designs. *IEEE Transactions on automatic control*, 53(10):2324–2334, 2008.

[29] C. Fu and W. Tan. Control of unstable processes with time delays via ADRC. *ISA transactions*, 71:530–541, 2017.

[30] Z. Gao et al. Scaling and bandwidth-parameterization based controller tuning. In *ACC*, pages 4989–4996, 2003.

[31] H. Gassot, A. Caruette, T. Junquera, J.L. Borne, L. Grandsire, A. Thiébault, V. Ji, C. Verdy, C. Coddet, M. Jeandin, et al. Mechanical stiffening of SRF niobium cavities by thermal sprayed coating. In *Proceedings of the 9th Workshop on RF Superconductivity, Santa Fe, USA*, pages 472–477, 1999.

[32] R. Geng, J. Fischer, E. A. McEwen, and O. Trofimova. Nature and implication of found actual particulates on the inner surface of cavities in a full-scale cryomodule previously operated with beam. Technical report, Thomas Jefferson National Accelerator Facility (TJNAF), Newport News, VA …, 2015.

[33] B. Z. Guo and Z. L. Zhao. *Active disturbance rejection control for nonlinear systems: An introduction.* John Wiley & Sons, 2017.

[34] B. Gustavsen and A. Semlyen. Rational approximation of frequency domain responses by vector fitting. *IEEE Transactions on power delivery*, 14(3):1052–1061, 1999.

[35] J. Han. Control theory, is it a model analysis approach or a direct control approach? In *Journal of System Science and Mathematical Science Chinese Series, Vol. 9*, 1989.

[36] J. Han. From PID to active disturbance rejection control. *IEEE transactions on Industrial Electronics*, 56(3):900–906, 2009.

[37] J. Holzbauer, B. Chase, L. Doolittle, J. Einstein-Curtis, Y. Pischalnikov, W. Schappert, and C. Serrano. Active microphonics compensation for LCLS-II. Technical report, Fermi National Accelerator Lab.(FNAL), Batavia, IL (United States), 2018.

[38] J. Holzbauer, B. Chase, J. Einstein-Curtis, B. Hansen, E. Harms, J. Kaluzny, A. Klebaner, M. McGee, Y. Orlov, T. Peterson, et al. Passive microphonics mitigation during LCLS-II cryomodule testing at Fermilab. Technical report, Fermi National Accelerator Lab.(FNAL), Batavia, IL (United States), 2018.

[39] B. Holzer, M. Klein, O. Brüning, A. Bogacz, and K. André. Accelerator challenges of the LHeC project. *12th International Particle Accelerator Conference (IPAC 2021)*, 2021.

[40] Y. Huang and J. Han. Analysis and design for the second order nonlinear continuous extended states observer. *Chinese science bulletin*, 45:1938–1944, 2000.

[41] S. Humphries. *Principles of charged particle acceleration.* Courier Corporation, 2013.

[42] Markus Hüning. *Selbstoptimierende Parametersteuerung der Hochfrequenz des supraleitenden Linearbeschleunigers TESLA Test Facility.* PhD thesis, RWTH Aachen University, 1998.

[43] Xilinxs Inc. Xilinx system generator for DSP (version 2018.1), 2018.

[44] National Instruments. *Device specifications NI 5783.*

[45] National Instruments. *NI 5781R User Guide and Specifications.*

[46] National Instruments. *NI-7931R/7932R/7935R User Manual.*

[47] National Instruments. *NI FlexRIO FPGA Module Installation Guide and Specifications.*

[48] National Instruments. *NI myRIO-1900, user Guide and specifications.*

[49] National Instruments. *NI PXIe-1082 User Manual.*

[50] National Instruments. *NI PXIe-8135 User Manual.*

[51] C. Joshi, B. Bent, M. Drury, J. Preble, and V. Nguyen. A magnetostrictive tuning mechanism for SRF cavities. In *Proceedings of the 1999 Particle Accelerator Conference (Cat. No. 99CH36366)*, volume 2, pages 931–933. IEEE, 1999.

[52] J. Jugo, A. Elejaga, and P. Echevarria. Modified active disturbance rejection control scheme for systems with time delay. *IET Control Theory & Applications*, 2023.

[53] Y. Kadi, M.A. Fraser, and A. Papageorgiou-Koufidou. HIE-ISOLDE: technical design report for the energy upgrade. *CERN Yellow Reports: Monographs, CERN*, 2018.

[54] M. Keikha, M. Moallem, G. Zhu, and K. Fong. Microphonic noise cancellation in superconducting cavity. In *IECON 2019 - 45th Annual Conference of the IEEE Industrial Electronics Society*, volume 1, pages 449–454, 2019.

[55] T. Khabiboulline. SRF cavity design, RF measurements and tuning, June 2017.

[56] M. Klein and A. Stocchi. PERLE: a high power energy recovery facility for europe a contribution to the update of the european strategy on particle physics. Technical report, CERN, 2018.

[57] J. Knobloch, W. Anders, M. Martin, S. Bauer, M. Pekeler, S. Belomestnykh, D. Kostin, W. Moller, A. Buchner, H. Buttig, et al. CW operation of the TTF-III input coupler. In *Proceedings of the 2005 Particle Accelerator Conference*, pages 3292–3294. IEEE, 2005.

[58] J. Knobloch, W. Anders, D. Pflückhahn, M. Schuster, et al. HoBiCaT: A test facility for superconducting RF systems. In *Proc. 2003 Workshop on RF superconductivity*, 2003.

[59] J. Knobloch, O. Kugeler, A. Neumann, C. Albrecht, K. Jensch, R. Lange, and L. Lilje. Full characterization of the piezo blade tuner for superconducting RF cavities. In *Proceedings of EPAC08*, 2008.

[60] O. Kugeler, A. Neumann, W. Anders, and J. Knobloch. Measurement and compensation of microphonics in CW-operated TESLA-type cavities. *Proceedings of ERL07, Daresbury, UK*, 01 2007.

[61] SLAC National Accelerator Laboratory, United States. Department of Energy. Office of Scientific, and Technical Information. *Some Wakefield Effects in the Superconducting RF Cavities of LCLS-II.* United States. Department of Energy. Office of Science, 2014.

[62] Y. Li, M. Sun, Z. Wang, and Z. Chen. Quantitative analysis of critical limitation in using extended state observer: IJCAS. *International Journal of Control, Automation, and Systems*, 14(3):876–882, 06 2016. Copyright - Institute of Control, Robotics and Systems and The Korean Institute of Electrical Engineers and Springer-Verlag Berlin Heidelberg 2016; Última actualización - 2023-06-20.

[63] J. Ma, G. Huang, et al. Microphonics simulation and parameters design of the SRF cavities for CiADS. In *10th Int. Particle Accelerator Conf. (IPAC'19), Melbourne, Australia, 19-24 May 2019*, pages 2903–2905. JACOW Publishing, Geneva, Switzerland, 2019.

[64] S. Michizono. The international linear collider. *Nature Reviews Physics*, 1(4):244–245, 2019.

[65] S. Myers and E. Picasso. The design, construction and commissioning of the CERN large electron-positron collider. *Contemporary Physics*, 31(6):387–403, 1990.

[66] A. Nakhmani. *Modern Control: State-Space Analysis and Design Methods.* McGraw-Hill Education, 2020.

[67] A. Neumann. *Compensating microphonics in SRF cavities to ensure beam stability for future free electron lasers.* PhD thesis, Humboldt University of Berlin, 2008.

[68] A. Neumann, W. Anders, O. Kugeler, and J. Knobloch. Analysis and active compensation of microphonics in continuous wave narrow-bandwidth superconducting cavities. *Physical Review Special Topics-Accelerators and Beams*, 13(8):082001, 2010.

[69] A. Neumann and J. Knobloch. RF control of the superconducting linac for the Bessy FEL. *Proceedings of EPAC, Lucerne, Switzerland*, pages 973–975, 2004.

[70] Massachusetts Institute of Technology. web.mit.edu. https://web.mit.edu/22.09/ClassHandouts/Charged Accessed: January 27, 2024.

[71] H. Padamsee. Design topics for superconducting RF cavities and ancillaries. *arXiv preprint arXiv:1501.07129*, 2015.

[72] H. Padamsee, J. Knobloch, and T. Hays. *RF Superconductivity for Accelerators*. John Wiley & Sons, 1998.

[73] C. Pagani, R. Paparella, A. Bosotti, P. Pierini, P. Michelato, and N. Panzeri. The fast piezo-blade tuner for SCRF resonators. In *Proceedings of the 12th International Workshop on RF Superconductivity*, 2005.

[74] Y. Pischalnikov and C. Contreras-Martinez. Review of the application piezoelectric actuators for SRF cavity tuners. *arXiv preprint arXiv:2305.06868*, 2023.

[75] T. Powers. Control of microphonics for narrow control bandwidth cavities. In *Talk presented at the 2017 International Conference on RF Superconductivity, Lanzhou, China*, 2017.

[76] R. Prakash, A. Ratan J., and V. Kumar. Multipacting studies in elliptic SRF cavities. *Nuclear Instruments and Methods in Physics Research Section A: Accelerators, Spectrometers, Detectors and Associated Equipment*, 867:128–138, 2017.

[77] M. Ramirez-Neria, H. Sira-Ramírez, A. Luviano-Juarez, and A. Rodríguez-Angeles. Smith predictor based generalized PI control for a class of input delayed nonlinear mechanical systems. In *2013 European Control Conference (ECC)*, pages 1292–1297. IEEE, 2013.

[78] D. K. Ravikumar, Y. R. Than, and J. P. Longtin. Eliminating flow-induced microphonics in a superfluid helium cryogenic system. *Cryogenics*, 104:102984, 2019.

[79] R. Rybaniec, K. Przygoda, W. Cichalewski, V. Ayvazyan, J. Branlard, Ł. Butkowski, S. Pfeiffer, C. Schmidt, H. Schlarb, and J. Sekutowicz. FPGA-based RF and piezocontrollers for SRF cavities in CW mode. *IEEE Transactions on Nuclear Science*, 64(6):1382–1388, 2017.

[80] H. Saugnac and P. Blache. Cryogenic installation status of the CryHoLab test facility. In *this workshop*, 2001.

[81] T. Schilcher. Vector sum control of pulsed accelerating fields in Lorentz force detuned superconducting cavities. Technical report, DESY Hamburg, Germany, 1998.

[82] J.K. Sekutowicz. Superconducting elliptical cavities. *arXiv preprint arXiv:1201.2598*, 2012.

[83] N. Shipman, J. Bastard, I. Ben-Zvi, G. Burt, A. Castilla, M. Coly, F. Gerigk, C. Jing, A. Kanareykin, S. Kazakov, et al. A ferroelectric fast reactive tuner for superconducting cavities. Technical report, Fermi National Accelerator Lab.(FNAL), Batavia, IL (United States), 2019.

[84] N. C. Shipman, N. Stapley, G. Burt, A. Kanareykin, I. Ben-Zvi, H. Timko, C. J. Jing, M. R. Coly, A. Castilla, A. Macpherson, et al. Ferro-electric fast reactive tuner applications for SRF cavities. *JACoW IPAC*, 2021:1305–1310, 2021.

[85] S. Simrock. Review of slow and fast tuners. In *SRF2005*, Ithaca, NY, 2005.

[86] S. Simrock and Z. Geng. *Low-level radio frequency systems*. Springer Nature, 2022.

[87] H. Sira-Ramírez, A. Luviano-Juárez, M. Ramírez-Neria, and E. W. Zurita-Bustamante. *Active disturbance rejection control of dynamic systems: a flatness based approach*. Butterworth-Heinemann, 2017.

[88] J. C. Slater. Microwave electronics. *Reviews of Modern Physics*, 18(4):441, 1946.

[89] S. Stapnes. The compact linear collider. *Nature Reviews Physics*, 1(4):235–237, 2019.

[90] W. Tan and C. Fu. Analysis of active disturbance rejection control for processes with time delay. In *2015 American control conference (ACC)*, pages 3962–3967. IEEE, 2015.

[91] G. Tian. *Reduced-order extended state observer and frequency response analysis*. PhD thesis, Cleveland State University, 2007.

[92] N. Valles, M. Liepe, et al. The superheating field of niobium: theory and experiment. *Proceedings of SRF2011*, 2:12, 2011.

[93] J. Vincent, D. Morris, N. Usher, Z. Gao, S. Zhao, A. Nicoletti, and Q. Zheng. On active disturbance rejection based control design for superconducting RF cavities. *Nuclear Instruments and Methods in Physics Research Section A: Accelerators, Spectrometers, Detectors and Associated Equipment*, 643(1):11–16, 2011.

[94] W. Weingarten. Superconducting cavities: basics. Technical report, CERN, 1996.

[95] J. G. Weisend et al. *Handbook of cryogenic engineering*. Taylor & Francis, 1998.

[96] D. Williamson. *Discrete-time signal processing: an algebraic approach*. Springer Science & Business Media, 2012.

[97] Z. Wu, D. Li, and Y. Chen. Active disturbance rejection control design based on probabilistic robustness for uncertain systems. *Industrial & Engineering Chemistry Research*, 59(40):18070–18087, 2020.

[98] E. Zaplatin, I. Gonin, T. Khabiboulline, V. Yakovlev, et al. SRF low-beta elliptical resonator two-ring stiffening. In *28th Linear Accelerator Conf.(LINAC'16), East Lansing, MI, USA, 25-30 September 2016*, pages 929–931. JACOW, Geneva, Switzerland, 2017.

[99] S. Zhao and Z. Gao. Modified active disturbance rejection control for time-delay systems. *ISA transactions*, 53(4):882–888, 2014.

[100] Q. Zheng and Z. Gao. On practical applications of active disturbance rejection control. In *Proceedings of the 29th Chinese Control Conference*, pages 6095–6100, 2010.

[101] Q. Zheng and Z. Gao. On active disturbance rejection for systems with input time-delays and unknown dynamics. In *2016 American control conference (ACC)*, pages 95–100. IEEE, 2016.

[102] Z. Zheng, Z. Liu, J. Wei, S. Zhao, and Y. Zhang. ADRC control for beam loading and microphonics. *Proc. of LINAC2012, Tel-Aviv, Israel, TUPB061*, page 615, 2012.

[103] Z. Zheng, S. Zhao, Z. Liu, D. Morris, J. Wei, and Y. Zhang. Study of microphonics compensation for SRF cavity. *Proceed. of PAC2013*, pages 1355–1357, 2013.

[104] R. Zhou and W. Tan. A generalized active disturbance rejection control approach for linear systems. In *proceedings of IEEE 10th Conference on Industrial Electronics and Applications (ICIEA)*, pages 248–255, 06 2015.